The Dusty, Molecular Envelopes of Red Supergiant Stars: VY Canis Majoris as the Archetypal Example

Dissertation

zur

Erlangung des Doktorgrades (Dr. rer. nat.)

der

Mathematisch-Naturwissenschaftlichen Fakultät

der

Rheinischen Friedrich-Wilhelms-Universität Bonn

vorgelegt von

Lies Verheyen

aus

Leuven, Belgien

Bonn (Juni, 2011)

Angefertigt mit Genehmigung der Mathematisch-Naturwissenschaftlichen Fakultät der Rheinischen Friedrich-Wilhelms-Universität Bonn

Diese Dissertation ist auf dem Hochschulschriftenserver der ULB Bonn unter http://hss.ulb.uni-bonn.de/diss_online elektronisch publiziert.

1. Gutachter: Prof. Dr. K. M. Menten
2. Gutachter: Prof. Dr. N. Langer
Tag der Promotion: 28 Oktober 2011
Erscheinungsjahr: 2011

Abstract

Red supergiant stars are surrounded by dusty envelopes, which harbor a multitude of molecules. Often, they are also known to show maser emission. We collect a sample of 88 red supergiants associated with Galactic open clusters, and detect SiO maser emission at 86 GHz towards 13 sources with the IRAM 30m telescope. The maser observations allow us to determine the stellar line-of-sight velocity with high accuracy. A comparison of the maser peak flux with previous detections at 43 GHz shows that the 86 GHz maser is stronger in 10 out of the 12 red supergiants detected in both transitions. An analysis of the colors of the observed sources indicates that the detections occur in the reddest sources, supporting a radiative pumping mechanism for the SiO maser.

The hypergiant VY CMa has a famous asymmetric nebula. We apply a two-dimensional radiative transfer code to model the dust continuum spectrum and optical and near-IR images. We find that VY CMa is surrounded by a dusty disk with surface density $\Sigma \propto r^{-1}$ which is observed under an inclination angle of 55°. The dust has a total mass of 10^{-3} $M_{\odot}$ and consists of a mixture of metallic iron, alumina, olivine and melilite. The central star is best represented by a black body of 2800 K. The mass of VY CMa is 15 $M_{\odot}$.

With the Plateau de Bure interferometer, we observe a selection of molecular transition in VY CMa's nebula: HCN(1-0), HCO^{+}(1-0), SiS(5-4), NaCl(7-6), NaCl(8-7), $SO_2(3_{1,3}\text{-}2_{0,2})$, $SO_2(16_{2,14}\text{-}15_{3,13})$ and $SO_2(10_{1,9}\text{-}10_{0,10})$. The interferometric images show that different molecules trace different parts of the envelope. NaCl is present exclusively in the spherical outflow, while SO_2 is found in the bipolar outflow. Others, like HCN and SiS, exist in all components of the envelope. We reproduce the observed emission by constructing a model of the envelope plus outflow. The bipolar outflow has an opening angle of 120°, a constant H_2 density and the expansion velocity increases linearly from 15 km s^{-1} to 45 km s^{-1}.

para jona

Acknowledgements

I wish to thank Prof. Karl Menten for offering me the opportunity to start working on my PhD thesis at the Max-Planck-Institut für Radioastronomie (MPIfR) in Bonn, and for supervising me throughout the process. I am grateful for his time and support, and for all the knowledge he shared with me. I was fortunate to be part of the submm group, where I could benefit from the help of many colleagues, such as Endrik Krügel, Friedrich Wyrowski and Maria Messineo.

I am thankful to the International Max Planck Research School (IMPRS) for Astronomy and Astrophysics at the Universities of Bonn and Cologne, for the financial and scientific support. I particularly want to thank Eduardo Ros and Gabi Breuer, as well as Emmanouil Angelakis and Simone Pott, respectively the former and current IMPRS coordinator and secretary.

Special thanks are for Leen Decin from the Katholieke Universiteit Leuven. Without her help, it would have been impossible to finish this work. I want to thank her for all the time she made available for me. It was always a pleasure visiting my old university in Leuven again.

With the financial support offered by the IMPRS and the MPIfR, I had to chance to attend a number of summer and winter schools, and visit collaborators such as Dejan Vinković, Jan Martin Winters, Michiel Min and Dieter Poelman. I learned a lot from them.

My final thanks go to my family and friends. Without their constant support, I wouldn't have been able to complete this work. Bedankt mama en papa, voor al jullie steun, jullie hulp en interesse, voor de ontelbare ritjes naar Bonn. Bedankt om er altijd voor mij te staan. To my sisters, Sanne, Dorien en Lotte: bedankt voor de bezoekjes en de telefoontjes. To my cousin Lore: bedankt voor je briefjes en het vele langskomen. And to Jonathan: gracias por todo.

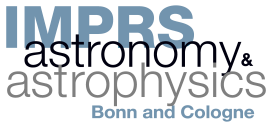

Contents

Max-Planck-Institut
für Radioastronomie

1 Introduction

1.1 Red Supergiant Stars

Red Supergiants (RSG) are a remarkable class of stars. Reaching the end of their life, stars with masses between 8 and 30 $M_\odot$ will undergo extensive mass-loss (10^{-7} – 10^{-3} $M_\odot$ yr^{-1}), creating a cool circumstellar envelope. This envelope is the perfect environment for the creation of a variety of molecules and dust grains, making the stars strong infrared (IR) sources. As RSGs will lose most of their mass to the interstellar medium (ISM) during this short ($\sim 10^4 - 10^5$ yr) evolutionary phase, and eventually end up as supernovae, they provide an important contribution to the elemental enrichment of the ISM.

1.1.1 Evolution of massive stars

The extreme properties of RSG stars are a consequence of their evolutionary state. Massive stars ($M > 8$ $M_\odot$) spend about 90% of their lifetime on the main sequence. During this stable phase hydrogen is burned in the stellar core. After a few million years, the central hydrogen is depleted and the star, which now consists of a core of helium surrounded by a hydrogen mantle, leaves the main sequence. The termination of central energy production causes the core to contract and heat up. Due to the increasing temperature H-shell burning is ignited, supplying the necessary energy to counter

gravity, soon supported by helium core burning. At this point, the envelope becomes convective, cools down and has expanded considerably: the star reached the red supergiant phase. Since the core has a temperature high enough to prevent degeneracy, central helium burning is followed by carbon, oxygen and silicon burning. Where He burning still lasts for about one million years, C burning takes places for about 500 years and the timescale for silicon burning is only of the order of days (Woosley et al. 2002). With no central energy source left, the star is near the end of its life, and has only one fate: exploding as a type II supernova. It is, however, also possible that the star evolves back towards the left in the Hertzsprung-Russel (HR) diagram after the RSG phase, to become a yellow supergiant or Wolf-Rayet (W-R) star before exploding (see e.g. Conti 1976; Levesque 2010). It is yet unclear which parameters determine whether the RSG phase is the final stage before supernova explosion, or if the object will pass on to the W-R or yellow supergiant phase. Fig. 1.1 shows the evolution of the RSG stars through the HR diagram. Note that the evolutionary tracks are influenced by the metallicity. For instance, in galaxies with low metallicity the Hayashi limit for hydrostatical equilibrium shifts towards warmer temperatures, therefore imposing warmer limits to the coolest point in the RSG's evolution. As a result, RSGs in a low metallicity environment are on average of an earlier spectral subtype than those in higher metallicity galaxies (Elias et al. 1985; Levesque et al. 2006).

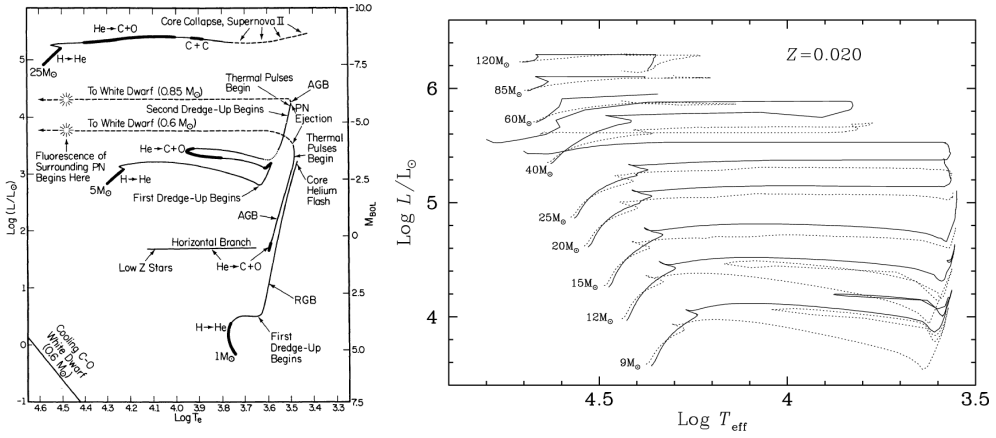

Figure 1.1: *Left*: HR diagram showing the evolutionary tracks for stars of different masses. At the top, the subsequent core burning cycles are marked along the track of a 25 $M_{\odot}$ RSG star (Iben 1985). *Right*: Evolutionary tracks for RSGs in a galactic metallicity environment (Z = 0.02) calculated by Meynet & Maeder (2003). Full lines represent non-rotating models, dotted lines correspond to models with an initial rotational velocity of 300 km s^{-1}.

1.1.2 Circumstellar envelopes

Red supergiants are cool ($T \sim 3500 - 4000$ K) objects of late K and M spectral type, with a very high luminosity ($L \sim 10^5\ L_\odot$), as can be seen from their position in the HR diagram (Fig. 1.1). They suffer extreme mass-loss, reaching from $10^{-7}\ M_\odot\ \mathrm{yr}^{-1}$ up to as high as $10^{-3}\ M_\odot\ \mathrm{yr}^{-1}$. This results in the formation of a cold, extended circumstellar envelope (CSE). The temperature decreases from typically 1500 K close to the stellar photosphere to ~25 K near the outer edge of the envelope, located around $10^4 - 10^5\ R_*$. Once the temperature has dropped below ~1000 K, dust particles start to form. Whether the envelope mainly consists of carbonaceous grains or silicates, depends on the C/O ratio. When O > C, as is usually the case for main sequence stars, (nearly) all carbon will be locked up in CO, and an oxygen-rich chemistry develops. The star is a so-called M-type star. Its spectrum is dominated by TiO bands, which can be used to determine the effective temperature. In the optical and near-IR, TiO is the main opacity source. On the other hand, dredge-up processes taking place during the turbulent post-main sequence evolution can bring enough carbon to the surface so that C > O. This leads to a much richer C-chemistry. A famous example of such a C-type star is the asymptotic giant branch (AGB) star IRC+10216, towards which over 60 different species have been detected. As a comparison, only 18 chemical compounds have been found around one of the most (if not *the* most) fascinating M-type red supergiants VY CMa (see Chapter 3).

Even though the circumstellar envelope consists of only 1% dust compared to 99% gas, the appearance of the spectral energy distribution (SED) of RSGs is determined by the dust. A large contribution to the flux at optical wavelengths comes from scattering by dust particles. Dust is an efficient absorber at shorter wavelengths, and emits at larger infrared wavelengths. Therefore, thermal dust emission dominates the IR part of the SED, causing the so-called infrared excess. It were observations of this infrared excess which led to the discovery of circumstellar dust shells around RSGs (e.g. Johnson 1968 for NML Cyg; Hyland et al. 1969 for VY CMa). Dust is also responsible for the occurrence of several molecular bands. The 9.7 μm silicate feature is a well-known example of such a band. The SED of the red supergiant NML Cyg, with the silicate feature in absorption, is shown in Fig. 1.2.

An accurate understanding of the chemistry, both dust and gas phase, of the envelopes of red supergiants is important in a broader context. These massive stars are laboratories where all heavy elements are created. Because of the strong mass-loss that RSGs are undergoing, and finally the supernova explosion, matter is constantly blown into space. In this way, red supergiants are responsible for the chemical enrichment of the interstellar medium. Since also AGB stars, the lower-mass counterparts of RSGs, lose

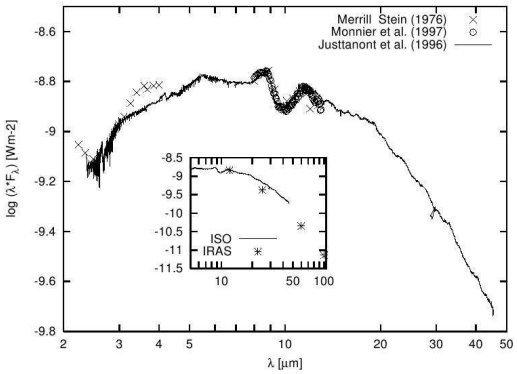

Figure 1.2: Spectral energy distribution of NML Cyg (Blöcker et al. 2001). The IR emission and silicate feature at 9.7 μm reflect the presence of a dusty circumstellar envelope, characteristic for RSG stars.

a significant amount of their mass to the ISM, the RSGs are mainly important in young starburst galaxies at large lookback times. In these galaxies, only the massive RSGs have had the time to evolve to their final stage, and are therefore the dominant dust producers.

The mechanism behind the mass-loss in RSGs, leading to the creation of the circumstellar envelope, is not yet fully understood. Radiation pressure on the dust grains is probably the main driving force of the strong wind. By means of collisions, momentum is transfered to the gas and it will be dragged along with the dust, resulting in an outflow with a typical expansion velocity of 15 km s^{-1}. Pulsations, rotation or convection are possibly also involved in the mass-loss process. Moreover, there is evidence for the occurrence of episodic mass-loss events in RSGs (Danchi et al. 1994), which complicates the determination of the precise mass-loss mechanism.

1.1.3 Masers

Maser (Microwave Amplification by Stimulated Emission of Radiation) emission has been observed towards RSG stars. Masers are a non-thermal process, caused by population inversions in the energy levels of molecules. Different pumping mechanisms, such as infrared radiation and collisions, can induce the population inversion. Maser lines from SiO, H_2O and OH are commonly found in red supergiants. SiO masers (43 GHz and 86 GHz) are produced closest to the central star, near the photosphere and below the dust formation layer. H_2O masers (22 GHz) are formed farther out in the envelope, and OH masers (1612 MHz, 1665 MHz and 1667 MHz) occur in the cooler

outer parts of the CSE. The presence or absence of particular maser lines appears to depend on the value of $\tau_{9.7\mu m}$: as the mass-loss rate increases, the increasingly opaque dust shell shields molecules longer against photodissociation by interstellar UV radiation. Lewis (1989) has analyzed the colors and associated masers of IRAS sources, and suggested a chronological sequence of increasing mass-loss rate: from SiO, via H_2O to OH masers. Maser studies are useful to determine stellar line-of-sight velocities, or measure parallaxes, and hence distances, accurately (e.g. Jewell et al. 1991). In the next chapter we will describe a search for 86 GHz SiO masers among Galactic RSGs associated with stellar clusters.

1.2 Outline

In this thesis we present the results of an analysis of red supergiant stars and their peculiar properties. First, we study the complete sample of known Galactic RSGs in open clusters, next we focus on one of the most exceptional red supergiants, the hypergiant VY CMa.

In Chapter 2 the SiO maser is investigated. Masers are common among red supergiants, but several questions remain unanswered. It is yet unknown why certain stars harbor masers in certain species, how the maser intensity is related to stellar properties, and also the pumping mechanism is not always precisely understood. Nevertheless, masers can provide valuable knowledge about their host stars. SiO masers proved to be the ideal tool to measure stellar line-of-sight velocities. In order to unravel unknown properties of SiO masers in red supergiant stars, a study of a large sample of RSGs is needed. Therefore, we collect a complete sample of RSGs in Galactic open clusters. Stars within each cluster share common properties such as metallicity, distance and age, and the occurrence of the SiO maser will thus depend upon the specific properties of each individual RSG. With the IRAM 30m telescope, we search for the 86 GHZ ($v = 1$, $J = 2 - 1$) SiO maser among a total of 88 red supergiants. We present the results of this survey, and discuss the detections cluster by cluster. We compare the observed maser intensities with previous detections at 43 GHz, and study the colors of the stars which harbor SiO masers.

Thereafter, we introduce one special red supergiant, known for its extreme luminosity and interesting circumstellar environment, VY CMa. Chapter 3 gives an overview VY CMa's properties. Results from the literature are summarized, we show images to demonstrate the asymmetry of its envelope, and previous modeling attempts are reviewed. In the next two chapters, we will focus on respectively the dust and gas chemistry of VY CMa's envelope.

The continuum emission of VY CMa is the subject of Chapter 4. Because of its dusty circumstellar envelope, the SED of VY CMa is dominated by a large infrared excess. We will construct a model of this envelope, where we introduce a dusty disk around VY CMa, and attempt to reproduce the observed spectral energy distribution. Moreover, optical and infrared images clearly show the asymmetry of the circumstellar environment. Therefore, we will also produce theoretical images to fit these observations.

In Chapter 5 we take a closer look at the gas chemistry. With the Plateau de Bure interferometer, we observe a number of molecular transition around VY CMa. Previous studies provided evidence for the existence of a bipolar outflow in VY CMa's envelope, with different molecules tracing different parts of the CSE. By using the advantages of interferometry, we hope to be able to distinguish between these different regions. Again, we will construct a model and try to reproduce the observed molecular emission, which will allow us to calculate abundances of the observed molecules.

Finally, Chapter 6 contains a summary of our results.

Max-Planck-Institut
für Radioastronomie

2

Silicon monoxide maser emission from red supergiants across the Galaxy

2.1 Introduction

Near the end of their lifetimes, stars of moderately high mass (10 $M_\odot < M_* < 30\ M_\odot$) go through the red supergiant evolutionary phase. Red supergiants are burning helium in their core, have luminosities more than 10^5 times that of the sun and, since their effective temperature is low (3500 - 4000 K), they are intrinsically luminous in the near-infrared (Levesque 2010). Studying RSGs and, in particular, their mass-loss history, is important for several reasons: RSGs are very luminous and may be recognized as individual objects in dusty galaxies and serve as tracers of young populations and as distance indicators. They contribute to the enrichment of the interstellar medium by losing mass at a high rate (10^{-5} to more than $10^{-4}\ M_\odot\ \mathrm{yr}^{-1}$) and by eventually exploding as core-collapse supernovae. Furthermore, RSG stars are often surrounded by circumstellar envelopes which may harbor maser emission. Maser emission reveals the line-of-sight velocity of the star to within a few km s^{-1} (Jewell et al. 1991). Frequently detected maser lines are from OH at 1.612 GHz, H_2O at 22.2 GHz, and SiO at 43 GHz and 86 GHz. The power of velocity determinations via maser lines was demonstrated by Messineo et al. (2002, 2004, 2005), who used the IRAM 30m telescope to find the 86

GHz SiO line discussed here toward 271 color-selected AGB stars out of 471 searched. The velocities obtained in this study provided important input for kinematic modeling of the inner Galaxy (Habing et al. 2006).

Some fundamental questions, however, have not yet been answered and this fact limits the use of RSG stars as well-calibrated tracers of young stellar populations. Probably the most important open questions are those of the relations (i) between the maximum luminosity, $L_{\rm max}$, of a given star and its main-sequence mass, $M_{\rm ms}$, and (ii) between mass-loss rate, $\dot{M}$, and stellar luminosity, L_*, and stellar initial metallicity Z. Possible stellar rotation further complicates their studies (Meynet & Maeder 2000). All these uncertainties also limit our understanding of these stars' circumstellar envelopes. In particular, it is unclear which stars exhibit maser emission in which species and which don't. This is certainly not only a function of temperature and mass-loss rate. Other parameters, like elemental abundances and stellar luminosity, probably also play an important role (Habing 1996).

Unfortunately, Galactic studies of RSG stars are hampered by the high and patchy interstellar extinction in the Galactic plane that combined with a possible periodic stellar light variation and possible circumstellar extinction renders the distinction between a massive RSG and an intermediate age mass-losing late-type star difficult (Comerón et al. 2004; Messineo et al. 2005; Messineo & Menten 2011). Furthermore, the uncertainties in the stellar distance prevent the determination of the luminosity of the stars, and stellar abundance measurements are not easy in obscured objects. It is obviously clear that to address these questions it is highly desirable to detect maser emission in RSGs other than the "classical" OH/IR RSGs VY CMa, VX Sgr, and NML Cyg, which were first recognized in the early 1970s (Buhl et al. 1974; Kaifu et al. 1975). Therefore, we present in this chapter a search for 86 GHz SiO maser emission towards 88 known RSG stars associated with open clusters.

2.2 Red supergiants in stellar clusters

Ideally, one wishes to observe RSG stars in clusters: the presence of an associated stellar cluster guarantees that these RSGs are coeval, at equal metallicity, and at the same distance as the other cluster stars. The RSGs distinct properties will thus only depend on their large initial masses. Stellar clusters rich in red supergiant stars must naturally be very massive and have an age from about 5 to 15 Myr (Meynet & Maeder 2000). Moreover, due to the steepness of the initial mass function, they must be very massive clusters.

Only a dozen massive clusters are currently known in the Milky Way. Their location in the near-side of the Galaxy confirms that their census is highly incomplete (Messineo et al. 2009). Three "well-known" examples of such clusters (mass $> 10^4\ M_{\odot}$) are the Arches and Quintuplet clusters (Cotera et al. 1996; Figer et al. 1999, 2002, 2004), both located near the Galactic center (GC), and the Westerlund I cluster (at $l = 340°$) (Westerlund 1961; Clark et al. 2005). However, the Arches and the Quintuplet may not be representative of massive cluster elsewhere in the Milky Way galaxy because of the peculiar conditions near the GC region. Fortunately, thanks to the new generation of near- and mid-infrared surveys (e.g. 2MASS, Spitzer), recently several more massive Galactic stellar clusters have been discovered around $l =\sim 25°$, at the base of the Scutum-Crux arm, which contain several RSGs. In the RSGC1 cluster 14 red supergiants have been spectroscopically confirmed (Figer et al. 2006; Davies et al. 2008). Only a few hundred parsecs from the RSGC1, the RSGC2 cluster (also called Stephenson 2 cluster (Stephenson 1990)) was found to contain 26 RSG stars (Davies et al. 2007). More recently, a third massive cluster dominated by red supergiants was discovered near the base of the Scutum-Crux arm (Clark et al. 2009; Alexander et al. 2009). This RSGC3 cluster contains 16 strong candidate RSG members. Moreover, a fourth cluster rich in RSG stars was identified not long ago in close vicinity of the RSGC1 cluster (Negueruela et al. 2010). The Alicante 8 or RSGC4 cluster contains another 13 candidate RSG members. Since this new cluster was not yet uncovered at the time of the observations presented in this chapter, it will not be included in the rest of the discussion. The total number of RSG stars in these four clusters amounts to 69, increasing the number of known RSGs by 40%. Before this, the cluster with highest known number of RSGs (five) was the NGC 7419 cluster (Beauchamp et al. 1994; Caron et al. 2003). Furthermore, the four RSGCs are concentrate within a few degrees of longitude ($25° - 29°$), likely at similar distance (5-6 kpc). The location of this extremely massive burst possibly coincides with the near endpoint of the Galactic Bar (Davies et al. 2009b).

Above clusters offer an extraordinarily important natural laboratory in which to study the evolution of RSGs and the properties of their envelopes. Altogether, we now have a sample of more than 100 Galactic RSGs in clusters at our disposal. Here we present a search for 86 GHz SiO maser emission toward these RSG stars. All the targets show infrared excess and therefore high mass-loss rates, from the analysis of existing photometric data (2MASS, MSX, Spitzer) (e.g. Figer et al. 2006). This makes them likely to exhibit maser emission, as the SiO maser flux is shown to be correlated with the mid-infrared continuum flux density (Bujarrabal et al. 1987; Bujarrabal 1994a).

2.3 SiO masers in red supergiants

RSGs undergo an extreme mass-loss which generates circumstellar envelopes. These envelopes often harbor maser emission from OH (1.612 GHz), H_2O (22 GHz) and SiO (43 GHz and 86 GHz) (see e.g. Habing 1996). In this chapter, we will focus on the 86 GHz SiO ($v = 1, J = 2 - 1$) maser.

2.3.1 SiO maser pumping

The pumping mechanism for the SiO maser is still under debate. Both radiative and collisional pumping models have been proposed. The basic mechanism for SiO maser pumping is described by Kwan & Scoville (1974). They find that SiO population inversions can occur when vibrational transitions become optically thick. Namely, in this case the vibrational de-excitation rates will be modified in such way that they decrease with increasing rotational level J. The logical result is an overpopulation of higher J rotational levels, thus an inversion, as long as the pumping happens by collisions or an indirect radiative route.

Models favoring either collisional or radiative pumping have been proposed by a number of authors. A mechanism for pumping through collisions with H_2 molecules was first presented by Elitzur (1980). Further modeling by, e.g., Lockett & Elitzur (1992) and Humphreys et al. (2002) also supported collisional pumping as the primary pumping mechanism for SiO masers. On the other hand, contrasting studies find radiative pumping to be dominant (e.g. Bujarrabal et al. 1987; Bujarrabal 1994a,b). From the observational point of view, the radiative pumping model explains the observed correlation between SiO maser intensity and the infrared continuum (e.g. Bujarrabal et al. 1987), while the dependence on stellar pulsations can be explained by collisional pumping (e.g. Heske 1989).

2.3.2 Importance of SiO maser studies

In this chapter, we present the results of a detection program for SiO maser emission at 86 GHz toward the complete sample of Galactic red supergiants associated with stellar clusters, i.e., of stars in environments of known metallicity, distance and interstellar extinction. This study will result in a new understanding of the occurrence of the SiO maser in RSG stars as a function of their luminosities and mass-loss rates. Furthermore, and most importantly, the maser line observations will provide accurate radial velocities for these stars. With the SiO maser detections we will therefore be able to estimate the kinematic distance to the cluster and, if several stars are detected, we will also calculate the velocity dispersion of the red supergiants and infer the disruption speed of

the cluster. These measurements will be more accurate than those based on velocities from the CO bandhead at 2.29 μm. Radial velocities from infrared CO absorption may vary with the stellar pulsation up to 15 km s^{-1} (Scholz & Wood 2000), while the midpoint of an SiO maser spectrum gives the stellar velocity with an accuracy of a few km s^{-1} (Jewell et al. 1991).

2.4 Sample

The targets of our 86 GHz observations consist of a sample of late-type stars in directions of massive clusters (confirmed or candidate RSG stars), and of other confirmed Galactic RSGs collected from previous studies. The list of targets is given in Tables 2.2 and 2.3, which will be discussed later. Table 2.2 gives the coordinates of the targets where an SiO maser was detected, and the line parameters (peak flux density, rms noise, radial velocity, line width, and velocity-integrated flux). Table 2.3 reports the coordinates of the targets not detected as well as the spectral rms noise. Several RSGs have already been found to emit SiO maser in both transitions, in the $v = 1$ and/or 2, $J = 1 - 0$ lines at 43 GHz (e.g. Nakashima & Deguchi 2006), as well as at 86 GHz (Haikala et al. 1994). Since the SiO maser emission is often variable (e.g Alcolea et al. 1990, 1999), a second epoch of observations may reveal a new maser emitter in those sources that have been studied before.

2.4.1 RSGC1

Figer et al. (2006) reported on a cluster with 14 RSGs, the RSGC1 cluster located at $l = 25\overset{\circ}{.}3, b = -0\overset{\circ}{.}2$. High-resolution near-infrared spectroscopy confirmed their memberships (Davies et al. 2008). The 14 RSG stars have spectral types between K2 and M6. The mean radial velocity of the stars is 123.0 ± 1.0 km s^{-1}, while the velocity dispersion is 3.7 km s^{-1}, which yields a dynamical mass of a few times 10^4 $M_\odot$. By assuming a kinematic distance of 6.60 ± 0.89 kpc, Davies et al. (2008) estimated luminosities $\log(L/L_\odot)$ from 4.87 to 5.45, which are consistent with a cluster age of 12 ± 2 Myr and initial masses of 18 $M_\odot$. We observed 8 of the 14 RSGs, and we use the same identification numbers given in Davies et al. (2008). We also included the Name X18 source, since it was already detected at 43 GHz (Nakashima & Deguchi 2006).

The bright mid-infrared source, Name X18, was suggested as a cluster member by Figer et al. (2006), together with its association with the X-ray emitter AX J1838.0−0655. The source was found to be masing by Nakashima & Deguchi (2006), and because of its much lower radial velocity (74 km s^{-1}), it was, then, classified as a non-member.

Because of its special position at the base of the Scutum-Crux arm, near the endpoint of the Galactic bar, this cluster could provide interesting insights into the structure and kinematics of the Milky Way. While it is well known that the Milky Way is a spiral barred galaxy, it is for instance still unclear how the Galactic bar and the spiral arms are related (Bissantz et al. 2003). Since the RSGC1 cluster is located at a distance of approximately 3.5 kpc from the Galactic center, at the corotation radius of the Galactic bar (Habing et al. 2006), it is in the perfect position to help to improve Galactic models.

2.4.2 RSGC2

The RSGC2 cluster was detected by Davies et al. (2007) as an overdensity of bright infrared stars in GLIMPSE and MSX images at $l = 26.^{\circ}2, b = 0.^{\circ}0$. Those stars are RSG stars, which are spectroscopically confirmed members of RSGC2 (Davies et al. 2007), and have spectral types from K2 to M5. In order to host such a large number of RSGs the cluster must have a likely mass of 4×10^4 $M_{\odot}$. From the average radial velocity (109.3 ± 0.7 km s^{-1}) a kinematic distance of $5.83^{+1.91}_{-0.78}$ kpc is inferred. By assuming this distance, and using theoretical models from Meynet & Maeder (2000), the authors derived a likely cluster age of 17 ± 3 Myr (or 12 ± 1 when considering non-rotating isochrones). Luminosities $\log(L/L_{\odot})$ of the RSGs range from 4.4 to 5.4, suggesting initial stellar masses of about 15 $M_{\odot}$ (Meynet & Maeder 2000). All 26 RSGs were included in our SiO maser program. We use the identification numbers given by Davies et al. (2007). We also included star number one in Davies et al. (2007), which is classified as a candidate RSG star foreground to the cluster by Davies et al. (2007), because of its brightness (K_S =2.9 mag) and radial velocity ∼ 95 km s^{-1}. The authors do not list a precise spectral type. The star was found to have SiO maser emission at 43 GHz by Deguchi et al. (2010).

2.4.3 RSGC3

The RSGC3 cluster was identified by Clark et al. (2009). It contains 8 RSGs spectroscopically confirmed with spectral types from K3 to M4, and 8 other candidate RSGs on the basis of photometric information. There are no radial velocity measurements available yet. The number of RSG stars suggests a cluster mass of about 2×10^4 $M_{\odot}$ - 4×10^4 $M_{\odot}$. The values of $\log(L/L_{\odot})$ range from 4.5 and 4.8 when assuming a distance of 6 kpc, and suggest initial masses similar to those of the RSGs in RSGC2.

The target selection and IRAM observations presented here were carried out before completion of the analysis of Clark et al. (2009). All 8 RSGs spectroscopically confirmed were included in our program, together with one of the candidate RSG stars. For those stars, we use the identification numbers given by Clark et al. (2009). Our list

includes also another star (2MASS J18452254-0322261) that is not listed among the stellar members in Clark et al. (2009).

2.4.4 NGC 7419

Before the discovery of the four RSGCs, the NGC 7419 cluster was the cluster with the largest number of known RSGs (Caron et al. 2003). The cluster is located near the Galactic plane at $l = 109\overset{\circ}{.}14, b = +1\overset{\circ}{.}14$ at a distance of 2.3 ± 0.3 kpc (Beauchamp et al. 1994; Caron et al. 2003), and has an age of 25 ± 5 Myr (Subramaniam et al. 2006). The four RSGs have spectral types from M2.5I to M7.5. We list these RSGs with the names provided in the SIMBAD database. Additionally, MY Cep is a rare late-type RSG star with a circumstellar envelope. It has already been detected in several maser surveys. It shows SiO, OH and water masers (Nakashima & Deguchi 2007; Sivagnanam et al. 1990; Takaba et al. 2001).

2.4.5 Perseus OB1

The PER OB1 cluster contains the double clusters h and χ Per. These are young clusters of ∼14 Myr, located at a distance of $2.34^{+0.08}_{-0.08}$ kpc and $2.29^{+0.09}_{-0.08}$ kpc, respectively (Currie et al. 2010). The association contains at least 12 red supergiants (Garmany & Stencel 1992; Pierce et al. 2000).

RSG stars in the χ Perseus OB1 association were included in our target list. The list was taken from Pierce et al. (2000). We also observed the brightest member of the NGC 457 cluster, which is a M1.5Iab star (Mermilliod et al. 2008).

2.4.6 GLIMPSE13

The cluster number 13 of Mercer et al. (2005) was detected as an overdensity of bright mid-infrared point sources. Messineo et al. (2009) performed near-infrared spectroscopy of the brightest stars in the core of the GLIMPSE13 cluster and detected late-type stars. Messineo et al. suggest that the bulk of stars are massive late M giant stars with spectral types between G9 and M1. If one assumes a supergiant class, the corresponding spectral types would range from early-K to late-G. However, yellow supergiants are naturally rarer than RSGs, and Galactic RSGs have a median spectral type M2. It is more likely that the stars in GLIMPSE13 are giants. The bright star GLIMPSE13 1 is too luminous to be a member of the same cluster (K_S=2.67 mag). GLIMPSE13 1 is an M0I or an M7III star.

Masers are a powerful tool to easily measure accurate radial velocities, and therefore to understand complex regions. A search for SiO masers and water masers in stellar clus-

ters was carried out by Deguchi et al. (2010). There is only an overlap of two sources with the stars in Messineo et al. (2009). The authors detected three stars (including GLIMPSE13 1) with a radial velocities around 70 km s^{-1} (72.3, 74.9 and 70.2 km s^{-1}), while they found GLIMPSE13 2 (a K5III star) to have a water maser with a velocity of 21.4 km s^{-1}.

The cluster is located on the disk of the Milky Way at 33.8° of longitude, in a region particularly rich. Several young stellar objects are located a few arcminutes north of the cluster, and a number of bright mid-infrared sources surround the cluster. It is most likely that we are seeing different groups of stars along the same line-of-sight, but not physically associated. A velocity of 71 km s^{-1} corresponds to a near-kinematic distance of $4.3^{+0.37}_{-0.36}$ kpc, while a velocity of 21 km s^{-1} implies a distance of $1.6^{+0.41}_{-0.43}$ kpc. GLIMPSE13 is an older cluster with an age between 50 and 100 Myr and a total mass around 6.7×10^3 $M_\odot$ (Messineo et al. 2009). We included in our target list the candidate RSG GLIMPSE13 1.

2.4.7 GLIMPSE9

The stellar cluster number 9 in the list of Mercer et al. (2005) was analyzed with near-infrared spectroscopy and HST/NICMOS photometry by Messineo et al. (2009). The authors detected 3 RSG stars and one late M giant (or early type RSG). The cluster is located at a distance of 4.2 kpc, has a likely age of 15-27 Myr, and a cluster mass of at least 1600 $M_\odot$.

We included in our target list all 4 late-type stars detected in the direction of the GLIMPSE9 cluster (3 RSGs and 1 giant).

2.4.8 SGR 1900+14

We also included among the targets the two RSG stars, members of the stellar cluster associated with the magnetar SGR1900+14 (Davies et al. 2009a). The cluster is located at a distance of 12.5 ± 1.7 kpc, and has a likely age of 14 Myr. The two M5I stars have an angular distance of about 1”, therefore only 1 single pointing was needed with the IRAM 30m telescope.

2.4.9 MFD2008

A young massive cluster was recently identified in the direction of the W33 complex at a distance of about 4 kpc. It contains several evolved early-type stars and 1 RSG (Messineo et al. 2008, 2011), from which a likely age of 4.5 Myr and a cluster mass

of 10^4 $M_\odot$ are inferred. We included among our targets the RSG identified in the MFD2008 cluster by Messineo et al. (2008).

2.4.10 Trumpler 27

The Trumpler 27 cluster is located at $l = 335.^\circ1, b = -0.^\circ7$ at a distance of 2.1 ± 0.2 kpc (Moffat et al. 1977). It contains a binary RSG star of M0 type (Massey et al. 2001). The presence of two WR stars and several other evolved OB stars suggests a cluster age below 6 Myr.

2.4.11 RSGs not associated with clusters

Blum et al. (2003) performed a spectro-photometric analysis of a sample of 79 luminous late-type stars in the central parsecs of the Galaxy. We observed 7 out of 17 RSGs listed by Blum et al. (2003).

With a similar technique, Comerón et al. (2004) identified another 18 RSGs in the direction of the inner Galaxy. We observed nine of these RSGs.

2.5 Observations

We observed the SiO ($v = 1, J = 2 - 1$) maser transition at 86.24335 GHz in 90 sources (88 (candidate) RSGs and 2 Mira variables) with the IRAM 30m telescope on Pico Veleta, Spain, during 3 epochs in September-October 2006, May 2008 and August 2008 (see Table 2.1). The A100 and B100 receivers were used, connected to the 256-channel 1 MHz low resolution filterbank with 3.5 km s^{-1} spectral resolution, as well as the VESPA autocorrelator at 40 kHz resolution and a bandwidth of 240 MHz. We used integration times between 5 and 15 minutes per source (on-off), observing in wobbler switching mode with a wobbler throw of 100”-120”. This gives an rms noise around 20-90 mK in T_A^* scale, equivalent to 0.12-0.54 Jy, using the conversion factor from antenna temperature to flux density of 6 Jy/K. The system temperatures ranged from 90 K to 300 K. We checked the telescope pointing every 1.5-3 h and obtained pointing errors varying around 3”.

We reduced the data with the CLASS program, which is part of the GILDAS software package[1]. A linear baseline was subtracted from the spectra. In order to qualify as a maser detection, we required that the peak flux density of the line exceeds three times the rms noise. Special attention was paid to the possible confusion with interstellar H^{13}CN, which has 3 hyperfine transitions in the 240 MHz VESPA band (Messineo

[1] http://www.iram.fr/IRAMFR/GILDAS

Table 2.1: IRAM 30m observing dates

Epoch	Dates
1	2006 September 29– October 2
2	2008 May 21–23
3	2008 August 9–11

et al. 2002). We detected the $H^{13}CN$ line in all of the Galactic center sources by Blum et al. (2003), none of which shows SiO maser emission at the expected velocities.

2.6 Results

We have detected SiO maser emission from RSGs in the following clusters: RSGC1 and RSGC2, NGC 7419, GLIMPSE13, and Trumpler 27. In addition we have observed maser emission from the two members of the h and χ Per double cluster that are known to harbor SiO masers, S Per (Kaifu et al. 1975) and W Per (Jiang et al. 1996). In total, 13 out of the 88 observed red supergiants were found to exhibit SiO maser emission in the $v = 1, J = 2 - 1$ transition at 86 GHz, with one new detection.

All spectra are presented in Figure 2.1 and the observed line parameter are listed in Table 2.2. The columns specify the RSG's name (taken from SIMBAD), its position by right ascension (R.A.) and declination (Dec.), the peak flux density (S, in Jy), the rms noise (rms, in Jy), the LSR velocity of the peak flux density ($v_{\rm LSR}$, in km s^{-1}), the LSR velocity range covered by the maser emission (v-range, in km s^{-1}), the velocity-integrated flux density ($\int S\, dv$, in Jy km s^{-1}), and a reference number. Table 2.3 lists upper limits for sources toward which no maser emission was found. The columns specify the RSG's name (taken from SIMBAD), its position by right ascension (R.A.) and declination (Dec.), and the rms noise (rms, in Jy).

For comparison, we also observed the maser emission from the Mira variables IK Tau and U Her. From Table 2.2 and Fig. 2.1, it is obvious that the emission from the Miras, while very strong due to the stars' small distance ($\sim$ 100 pc), covers much smaller velocity intervals than the RSGs' emission. Broader line profiles in red supergiants as compared to Miras have been observed before (e.g. Le Bertre & Nyman 1990). Fig. 2.2 shows a histogram of the velocity range covered by the SiO maser line. The Mira variables IK Tau and U Her are shown in a grey color. Clearly, their profiles are more narrow than the average RSG's. Alcolea et al. (1990) found the mean equivalent width, given by (profile-area)/(peak-intensity), of the 86 GHz SiO maser lines to be 8.6 km s^{-1}

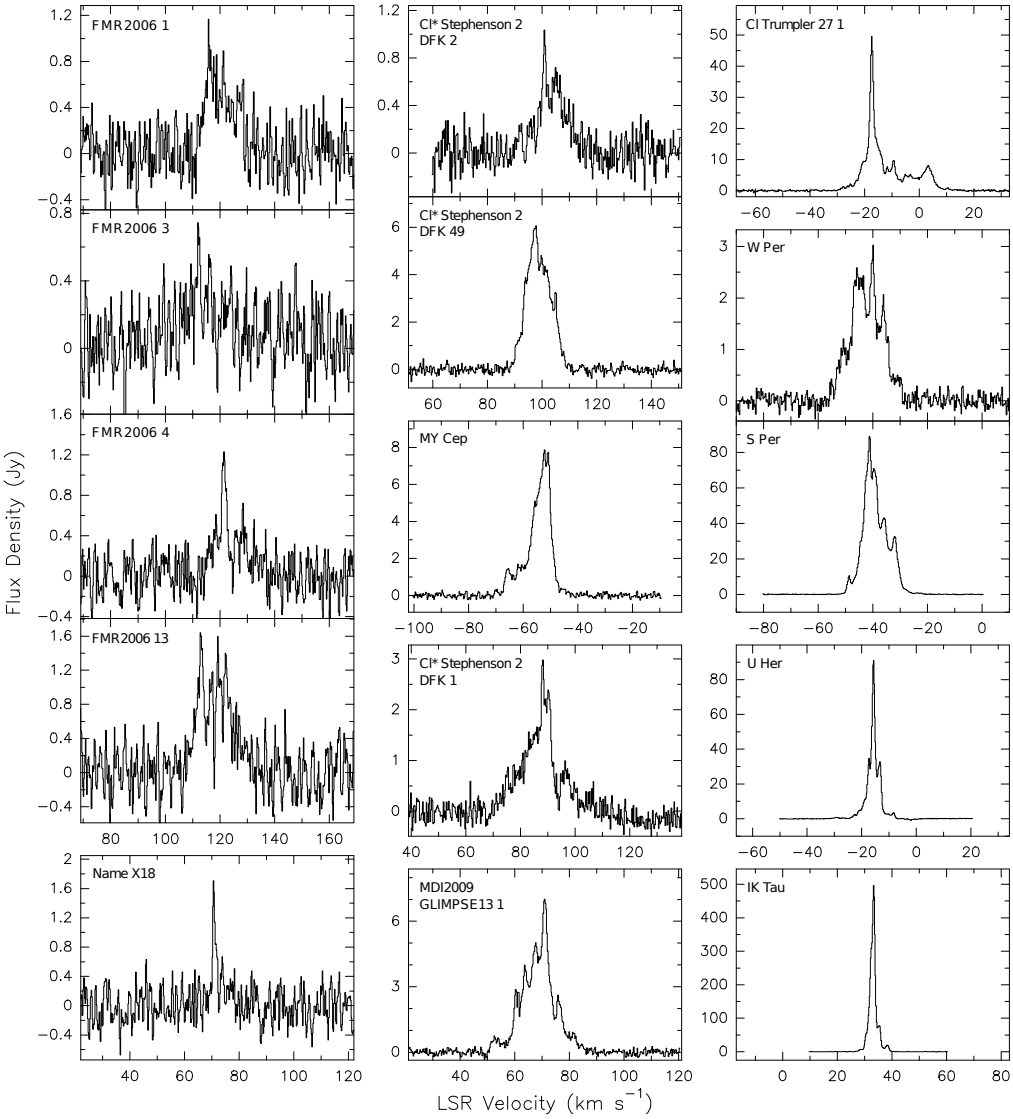

Figure 2.1: Spectra of the stars toward which we detected the SiO ($v = 1, J = 2 - 1$) line. All stars but Name X18, U Her, and IK Tau are RSGs. The latter two are Mira variables and we show their much narrower spectra for comparison.

Table 2.2: SiO ($v = 1, J = 2 - 1$) detections toward red supergiants.

Object	R.A.	Dec.	S [Jy]	rms [Jy]	$v_{\rm LSR}$ [km s^{-1}]	v-range [km s^{-1}]	$\int S\,dv$ [Jy km s^{-1}]	Ref.
RSGC1								
FMR2006 1	18:37:56.29	−06:52:32.2	1.2	0.20	116	[112,129]	8.1±3.0	(1)
FMR2006 3	18:37:59.73	−06:53:49.4	0.6	0.18	112	[110,117]	2.4±1.2	(1)
FMR2006 4	18:37:50.90	−06:53:38.2	1.1	0.18	121	[115,130]	6.1±1.8	(1)
FMR2006 13	18:37:58.90	−06:52:32.1	1.6	0.26	113	[108,128]	14.7±3.0	(1)
Name X18	18:38:01.62	−06:55:23.5	1.7	0.22	71	[69,75]	3.1±1.2	(1)
RSGC2								
Cl* Stephenson 2 DFK 1	18:39:02.40	−06:05:10.6	3.0	0.19	89	[71,101]	30.5±3.0	(2)
Cl* Stephenson 2 DFK 2	18:39:19.60	−06:00:40.8	1.0	0.12	101	[94,113]	6.9±1.8	(2)
Cl* Stephenson 2 DFK 49	18:39:05.60	−06:04:26.6	6.0	0.14	101	[88,109]	59.0±1.8	(2)
MY Cep	22:54:31.66	+60:49:40.3	7.9	0.11	−52	[-71,-42]	64.4±1.8	(3)
S Per	02:22:51.70	+58:35:12.0	91.1	0.21	−41	[-50,-28]	716.4±2.7	(4)
W Per	02:50:37.90	+56:59:00.0	3.0	0.14	−40	[-57,-29]	33.7±2.1	(4)
MDI2009 GLIMPSE13 1	18:53:52.49	+00:39:31.3	7.0	0.15	71	[57,84]	67.9±2.1	(5)
Cl Trumpler 27 1	17:36:10.12	−33:29:40.6	50.3	0.27	−17	[-25,9]	260.5±4.2	(6)
IK Tau (Mira)	03:53:28.84	+11:24:22.6	496.2	0.27	33	[30,36]	1074.0±1.5	(7)
U Her (Mira)	16:25:47.69	+18:53:33.1	90.8	0.22	−16	[-22,-12]	248.0±1.5	(8)

Columns are (from left to right) designation of red supergiant (names are taken from SIMBAD), right ascension, declination, peak flux density, rms noise, LSR velocity of peak flux density, LSR velocity range covered by maser emission, velocity-integrated flux density, and a reference number.
References are:
(1) RSGC1, Figer et al. (2006) (3) NGC 7419, Caron et al. (2003) (5) GLIMPSE13, Messineo et al. (2009) (7) IK Tau
(2) RSGC2, Davies et al. (2007) (4) Per OB1, Pierce et al. (2000) (6) Trumpler 27 cluster, Moffat et al. (1977) (8) U Her

for their sample of RSGs, and only 4 km s^{-1} for the Miras. In our case, using the values of Table 2.2, the RSGs have a mean equivalent width of 7.4 km s^{-1}, while the Miras have a width of 2.4 km s^{-1}. These values are somewhat smaller than those of Alcolea et al. (1990), but follow the same trend.

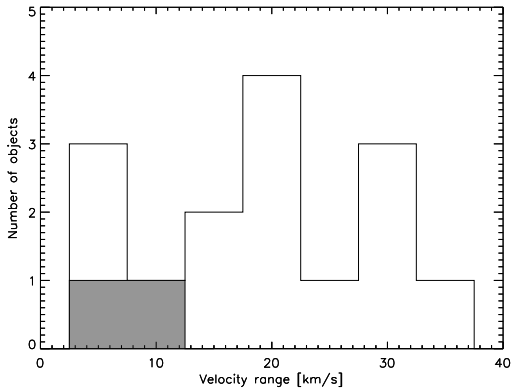

Figure 2.2: Histogram of the LSR velocity range covered by the maser emission. The grey region shows the Mira variables IK Tau and U Her.

Table 2.3: Red Supergiants without SiO ($v = 1, J = 2 - 1$) detection.

Object	R.A. [J2000]	Dec. [J2000]	rms [Jy]
RSGC1 cluster, Figer et al. (2006)			
FMR2006 11	18:37:51.72	−06:51:49.9	0.497
FMR2006 12	18:38:03.30	−06:52:45.1	0.499
FMR2006 14	18:37:47.64	−06:53:02.3	0.567
FMR2006 16	18:38:01.29	−06:52:51.9	0.590
RSGC2 cluster, Davies et al. (2007)			
Cl* Stephenson 2 DFK 3	18:39:24.60	−06:02:13.8	0.186
Cl* Stephenson 2 DFK 5	18:39:08.10	−06:05:24.4	0.192
Cl* Stephenson 2 DFK 6	18:39:18.40	−06:00:38.4	0.320
Cl* Stephenson 2 DFK 8	18:39:19.90	−06:01:48.1	0.325
Cl* Stephenson 2 DFK 9	18:39:06.80	−06:03:20.3	0.332
Cl* Stephenson 2 DFK 10	18:39:14.70	−06:01:36.6	0.338
Cl* Stephenson 2 DFK 11	18:39:18.30	−06:02:14.3	0.331
Cl* Stephenson 2 DFK 13	18:39:17.70	−06:04:02.5	0.337

Continued on next page...

Table 2.3: *Continued*

Object	R.A. [J2000]	Dec. [J2000]	rms [Jy]
Cl* Stephenson 2 DFK 14	18:39:20.40	−06:01:42.6	0.339
Cl* Stephenson 2 DFK 15	18:39:22.40	−06:01:50.1	0.351
Cl* Stephenson 2 DFK 16	18:39:24.00	−06:03:07.3	0.352
Cl* Stephenson 2 DFK 17	18:39:15.10	−06:05:19.1	0.342
Cl* Stephenson 2 DFK 18	18:39:22.50	−06:00:08.4	0.363
Cl* Stephenson 2 DFK 19	18:39:19.50	−05:59:19.4	0.371
Cl* Stephenson 2 DFK 20	18:39:24.10	−06:00:22.8	0.378
Cl* Stephenson 2 DFK 21	18:39:15.80	−06:02:05.5	0.369
Cl* Stephenson 2 DFK 23	18:39:01.50	−06:00:59.9	0.396
Cl* Stephenson 2 DFK 26	18:39:35.10	−05:59:15.8	0.410
Cl* Stephenson 2 DFK 27	18:39:16.00	−06:05:03.2	0.431
Cl* Stephenson 2 DFK 29	18:39:22.20	−06:02:14.7	0.460
Cl* Stephenson 2 DFK 30	18:39:23.40	−05:59:01.3	0.489
Cl* Stephenson 2 DFK 31	18:39:09.30	−06:01:06.9	0.527
Cl* Stephenson 2 DFK 52	18:39:23.40	−06:02:15.9	0.571
Cl* Stephenson 2 DFK 72	18:39:16.20	−06:03:07.2	0.624
RSGC3 cluster, Clark et al. (2009)			
CND2009 S1	18:45:23.60	−03:24:13.9	0.316
CND2009 S2	18:45:26.54	−03:23:35.4	0.196
CND2009 S3	18:45:24.35	−03:22:42.1	0.176
CND2009 S4	18:45:25.32	−03:23:01.1	0.155
CND2009 S5	18:45:23.27	−03:23:44.1	0.313
CND2009 S7	18:45:24.18	−03:23:47.4	0.238
CND2009 S8	18:45:20.06	−03:22:47.2	0.309
CND2009 S9	18:45:28.13	−03:22:54.6	0.303
CND2009 S14	18:45:29.03	−03:22:37.4	0.306
2MASS J18452254-0322261	18:45:22.54	−03:22:26.1	0.307
NGC 7419, Caron et al. (2003)			
Cl* NGC 7419 BMD 435	22:54:16.14	+60:49:29.0	0.138
Cl* NGC 7419 BMD 696	22:54:22.67	+60:48:31.7	0.146
Cl* NGC 7419 BMD 921	22:54:30.49	+60:47:50.7	0.149
Cl* NGC 7419 BMD 139	22:54:01.28	+60:47:42.0	0.154
Per OB1, Pierce et al. (2000); Mermilliod et al. (2008)			
FZ Per	02:20:20.60	+57:09:31.0	0.158

Continued on next page...

Table 2.3: *Continued*

Object	R.A. [J2000]	Dec. [J2000]	rms [Jy]
RS Per	02:22:24.30	+57:06:34.0	0.153
GP Cas	02:39:50.40	+59:35:51.0	0.156
T Per	02:19:21.90	+58:57:40.0	0.152
YZ Per	02:38:25.40	+57:02:46.0	0.150
AD Per	02:20:29.00	+56:59:35.0	0.151
BU Per	02:18:53.30	+57:25:17.0	0.140
V500 Cas	02:51:24.00	+57:50:00.0	0.138
XX Per	02:03:09.40	+55:13:57.0	0.143
SU Per	02:22:06.90	+56:36:14.0	0.111
NGC 457	01:19:53.64	+58:18:31.2	0.138
GLIMPSE9, Messineo et al. (2010)			
MFD2010 1	18:34:09.27	−09:14:00.7	0.159
MFD2010 5	18:34:09.87	−09:14:23.3	0.166
MFD2010 6	18:34:10.37	−09:13:49.5	0.180
MFD2010 8	18:34:10.36	−09:13:52.9	0.160
SGR 1900+14, Davies et al. (2009a)			
SGR 1900+14	19:07:15.35	+09:19:21.4	0.165
MFD2008, Messineo et al. (2008)			
MFD2008 1	18:13:22.26	−17:54:15.6	0.165
Galactic center, Blum et al. (2003)			
BSD96 1	17:45:36.93	−29:00:30.2	0.210
BSD96 14	17:45:38.52	−28:59:56.8	0.206
BSD96 48	17:45:39.69	−29:00:54.2	0.210
BSD96 66	17:45:39.99	−29:00:22.2	0.217
BSD96 79	17:45:40.14	−28:59:39.5	0.198
BSD96 108	17:45:41.08	−29:00:47.9	0.205
BSD96 109	17:45:41.12	−29:00:39.6	0.216
RSGs in the inner Galaxy, Comerón et al. (2004)			
CTC2004 64	18:07:50.72	−20:04:09.2	0.155
CTC2004 70	18:08:37.35	−19:50:05.3	0.152
CTC2004 74	18:09:37.50	−19:28:27.1	0.151
CTC2004 97	18:14:53.10	−17:00:51.3	0.147
CTC2004 121	18:16:38.18	−16:23:34.0	0.151
CTC2004 125	18:16:55.97	−16:09:54.3	0.157

Continued on next page...

Table 2.3: *Continued*

Object	R.A. [J2000]	Dec. [J2000]	rms [Jy]
CTC2004 152	18:18:05.31	−15:57:19.4	0.160
CTC2004 184	18:25:11.20	−12:28:40.2	0.154
CTC2004 194	18:27:39.07	−11:39:23.0	0.161

Columns are (from left to right) designation of red supergiant (names are taken from SIMBAD), right ascension, declination, and rms noise.

In the following we discuss our detections cluster by cluster.

2.6.1 RSGC1

We detected 5 SiO masers in the direction of the RSGC1. Nakashima & Deguchi (2006) already conducted a search for the SiO $v = 1$ and $v = 2$, $J = 1 - 0$ transitions at 43 GHz in the RSGC1 red supergiants. They detected maser emission from four of the 14 RSGs: FMR2006 1, FMR2006 2, FMR2006 4 and FMR2006 13. Only the latter was detected in both transitions, the other three objects only showed the $v = 1$ line. Additionally, in a follow-up observation the 86 GHz $v = 1, J = 2 - 1$ SiO maser line was detected in FMR2006 1 and FMR2006 2. On top of that, they also found emission from both the $v = 1$ and $v = 2$ transitions in Name X18, located 2' south of the RSGC1 cluster (Malizia et al. 2005).

Table 2.4: Comparison between the LSR velocities of the RSGC1 red supergiants obtained from different SiO maser observations.

Object	$v_{\rm LSR}$ [km s^{-1}]	
	ND06[a]	this study
FMR2006 1	115	116
FMR2006 2	120	
FMR2006 3		112
FMR2006 4	121	121
FMR2006 13	116	113
Name X18	74	71

[a] Nakashima & Deguchi (2006)

Our survey resulted in 86 GHz SiO maser detections towards the objects FMR2006 1, FMR2006 3, FMR2006 4, FMR2006 13 and Name X18. Due to time constraints, we didn't observe FMR2006 2, maser source according to Nakashima & Deguchi (2006). In summary, we detected all the maser sources listed in Nakashima & Deguchi (2006), with an additional new detection in FMR2006 3. The LSR velocities determined by Nakashima & Deguchi (2006) compare well with those obtained in our study (see Table 2.4).

We detected SiO maser emission in Name X18 with a velocity of 71 km s^{-1} (see Table 2.2). Our detection at 86 GHz is in agreement with that measured at 43 GHz, but 30 km s^{-1} below the cluster average velocity. A binary system star could deviate from the average cluster velocity, however, the agreement between the two measurements of radial velocities seems to exclude a binary system.

2.6.2 RSGC2

Three SiO masers were detected towards RSGC2 at 86 GHz. Recently, Deguchi et al. (2010) performed a SiO $v = 1$ and $v = 2$, $J = 1 - 0$ maser search at 43 GHz in 18 objects of the RSGC2 cluster, resulting in five detections. Cl* Stephenson 2 DFK 1 and DFK 2 were detected only in the $v = 1$ transition, while DFK 22, DFK 49 and 2MASS J18385699-0606459 showed both the $v = 1$ and $v = 2$ lines.

We detected three of the objects of Deguchi et al. (2010) in the 86 GHz $v = 1, J = 2 - 1$ line: Cl* Stephenson 2 DFK 1, DFK 2 and DFK 49. The LSR velocities derived from the 43 GHz maser lines are 93 km s^{-1}, 103 km s^{-1} and 101 km s^{-1}, respectively. (Deguchi et al. 2010). The velocities based on the 86 GHz lines, presented in Table 2.2, are of the same order: 89 km s^{-1} for Cl* Stephenson 2 DFK 1 and 101 km s^{-1} for both DFK 2 and DFK 49. We note that we detected SiO maser emission associated with star number 1 in the list by Davies et al. (2007). This star is likely a field RSG, not associated with RSGC2 (Davies et al. 2007).

2.6.3 NGC 7419

We only found maser emission at 86 GHz towards the brightest M7.5I member, MY Cep. The 43 GHz SiO maser had been detected before by Nakashima & Deguchi (2007). They derived a radial velociy of -53.7 km s^{-1} from the $v = 1, J = 1 = 0$ transition and -51.9 km s^{-1} from the $v = 2, J = 1 - 0$ line. Our observations resulted in a corresponding LSR velocity of -52 km s^{-1} (see Table 2.2), in agreement with the previous value.

2.6.4 Perseus OB1

Only two RSGs in the Per OB1 cluster were detected in our program, W Per and S Per. The detected stars are among the three RSG members with longer periods (485 and 822 days respectively; Pierce et al. 2000). The authors also noted their redder colors, and suggested a circumstellar envelope.

No SiO maser survey in the complete sample of RSGs in Per OB1 had been conducted so far. Only individual sources have been studied. SiO maser emission was detected before in W Per (Jiang et al. 1996) and S Per (e.g Kaifu et al. 1975). The ^{28}SiO $v = 1$ and $v = 2$, $J = 1 - 0$ and ^{29}SiO $v = 0$, $J = 1 - 0$ masers were searched towards FZ Per and T Per, but no emission was detected (Jiang et al. 1999). SU Per was targeted in a SiO $v = 1$, $v = 2$ and $v = 3$, $J = 1 - 0$ search, but no maser was found (Spencer et al. 1981).

W Per was found to show emission from the 43 GHz $v = 1$, $J = 1 - 0$ transition (Jiang et al. 1996). S Per was observed by various authors, in a number of transitions. The first detection was the $v = 1$, $J = 2 - 1$ line at 86 GHz by Kaifu et al. (1975). Furthermore, maser emission was found in the SiO $v = 1$, $v = 2$ and $v = 3$, $J = 1 - 0$ transitions (e.g. Spencer et al. 1977; Cho et al. 1996), the $v = 0$ and $v = 2$, $J = 2 - 1$ transitions (e.g Morris et al. 1979; Olofsson et al. 1981), and the $v = 1$, $J = 3 - 2$ transition (Herpin et al. 1998). Pardo et al. (1998) studied more than 15 different transitions of the SiO maser in S Per, detecting some high transitions such as $v = 2$ and $v = 3$, $J = 4 - 3$ and $v = 1$, $J = 5 - 4$.

We detected maser emission from S Per and W Per, the same objects with previously detected maser emission. We also extended the list of observed sources without a SiO maser detection. From the maser observation, we obtained a LSR velocity of -41 km s^{-1} for S Per and -40 km s^{-1} for W Per, respectively (see Table 2.2). Jiang et al. (1996) reported a velocity of -41.3 km s^{-1} for W Per based on their 43 GHz maser observations, in agreement with our findings. For S Per, several results can be found in the literature. Alcolea et al. (1990) find a LSR velocity of -40.0 km s^{-1} using the same transition at 86 GHz as presented here. This value is very similar to our result. Other recent studies of SiO masers in S Per also conclude a velocity around -41 km s^{-1} (e.g Kim et al. 2010).

2.6.5 GLIMPSE13

We detected SiO maser emission in the $v = 1$, $J = 2 - 1$ line in the RSG candidate GLIMPSE13 1. Maser emission at 43 GHz had been observed before by Deguchi et al.

(2010) in the $v = 1$, $J = 1 - 0$ transition. They found a LSR velocity of 69.4 km s^{-1} and 72.3 km s^{-1} on two separate observing days, completely in agreement with our value of 71 km s^{-1} (see Table 2.2).

2.6.6 Trumpler 27

We detected SiO maser emission at 86 GHz towards the binary RSG in Trumpler 27. The 43 GHz $v = 1$, $J = 1 - 0$ transition was already observed by Hall et al. (1990). The 86 GHz $v = 1$, $J = 2 - 1$ line was also found before (Haikala et al. 1994). Our corresponding LSR velocity is -17 km s^{-1} (see Table 2.2), slightly higher than the -11 km s^{-1} reported by Haikala et al. (1994).

2.6.7 Clusters without detections

We didn't detect the 86 GHz SiO maser in any of the members of some of our target RSG clusters. RSGC3 (Clark et al. 2009), GLIMPSE9 (Messineo et al. 2010), the Galactic center cluster (Blum et al. 2003) and the collection of RSGs in the inner Galaxy (Comerón et al. 2004) are clusters without maser detections (see Table 2.3). For these clusters, we were the first to study the occurrence of SiO maser emission, and we report the first non-detections in their members. Since the SiO masers are variable with the pulsation phase (e.g. Alcolea et al. 1990, 1999), follow-up observations could be useful to detect possible maser emission.

Recently, several new clusters rich in red supergiants have been identified, e.g. RSGC4 (Negueruela et al. 2010). Radial velocity measurements by means of SiO maser observations could provide important information about the membership of candidate cluster stars. We included the newly discovered RSGC3 in our survey, but unfortunately we didn't detect maser emission from its RSG stars.

2.6.8 Summary

We searched 88 (candidate) RSGs for the presence of the 86 GHz SiO maser. We detected maser emission from 13 RSGs, 1 of which was a new detection. Several of these 13 sources were observed before, and SiO, OH or H_2 masers were found. Table 2.5 gives an overview of the current and previous maser detections.

2.7 SiO maser intensities

In Table 2.6, we list the ratio of the 43 GHz peak flux from the literature over the 86 GHz peak flux derived here. Apart from IK Tau, MY Cep and Cl* Stephenson 2 DFK

Table 2.5: Previous maser information.

Name	H_2O	SiO	OH	v_{LSR}	References	Comment
FMR2006 1		SiO		+115.0	(1)	
FMR2006 3						NEW
FMR2006 4		SiO		+121.5	(1)	
FMR2006 13		SiO		+116.5	(1)	
Name X18		SiO		+74.3	(1)	
Cl* Stephenson 2 DFK 2	H_2O	SiO		+102.7	(2)	
Cl* Stephenson 2 DFK 49	H_2O	SiO		+98.6	(2)	
Cl* Stephenson 2 DFK 1	H_2O	SiO		+92.7	(2)	
MY Cep	H_2O	SiO	OH	−55.8	(3),(4),(5)	
W Per	H_2O	SiO		-40.0	(6)	
S Per	H_2O	SiO	OH	-37.0	(4),(6)	
MDI2009 GLIMPSE13 1		SiO		+72.3	(2)	
Cl Trumpler 27 1		SiO			(7)	
IK Tau	H_2O	SiO	OH	+35.0	(4)	
U Her	H_2O	SiO	OH	−15.0	(4)	

References are:
(1) Nakashima & Deguchi (2006)
(2) Deguchi et al. (2010)
(3) Nakashima & Deguchi (2007)
(4) Benson et al. (1990)
(5) Takaba et al. (2001)
(6) Valdettaro et al. (2001)
(7) Hall et al. (1990)

2, the 86 GHz transition is found to be stronger in all sources. The 86 GHz transition is thus the best transition to determine radial velocities for our sample of RSG stars. Nyman et al. (1993) concluded that the 43 GHz over 86 GHz ratio is higher for OH/IR stars with higher mass-loss rates. An analysis of the K – [12] colors, with the [12] magnitude taken from the MSX C-band (Price et al. 2001), of the RSGC2 members by Davies et al. (2007) shows that DFK 2 is among the higher mass-losing stars in this cluster. Indeed, Whitelock et al. (1994) proved the correlation between the K – [12] colors and the mass-loss rate. This can explain the high 43/86 GHz ratio. The K – [12] color of DFK 49 suggests even higher mass-loss, but both masers have an almost equal intensity. We should note, however, that the SiO maser intensity is found to vary during the stellar variability cycle (e.g. Alcolea et al. 1990, 1999). Since the 43 GHz and 86 GHz observations were not simultaneous, one of the two peak intensities could be measured at a stronger stellar phase. Therefore, the listed ratios are not conclusive, and a simultaneous detection program is needed as a final proof of the advantage of the 86 GHz transition to determine line-of-sight velocities in these RSG stars.

We also calculated the 86 GHz peak flux over the IR 8 μm peak flux ratio (see Table 2.6). The 8 μm fluxes were taken from the MSX (Price et al. 2001) and GLIMPSE (Benjamin et al. 2003) catalogues when available. Previously, Alcolea et al. (1990) performed a SiO maser search in Miras and supergiants, and found that SiO(86 GHz peak flux)/IR(8μm flux) is $\sim$ 1/5 for Miras and the strongest RSGs, but significantly lower for the other supergiants (with 0.003 for SW Vir being the lowest ratio). Again we should note that both SiO maser and IR flux might not be at their maximum.

2.8 Maser occurrence with target colors

In Messineo & Menten (2011) we report 2MASS and GLIMPSE color properties of known evolved mass-losing stars. With a combination of near- and mid-IR colors it is possible to identify mass-losing stars and to distinguish between highly reddened "naked" stars and dust-enshrouded stars. This is possible because stars with circumstellar envelopes deviate from the locus of the reddening vector, and such a deviation is proportional to the mass-loss rate. In Messineo & Menten (2011) we attempt to quantify this effect by defining two extinction-free parameters. The Q parameter ($Q = (J-H) - 1.8\times(H-K)$) is a measure of the deviation from the reddening vector in the $(J-H)$ versus $(H-K)$ plane, while the $Q2$ parameter ($Q2 = (J-K) - 3.26\times(K-[8.0])$) measures the deviation in the plane $(J-K)$ versus $(K-[8.0])$. The angular coefficients are defined using the near-infrared extinction power law by Messineo et al. (2005), and the mid-infrared extinction ratios provided by Indebetouw et al. (2005) for the GLIMPSE bands.

Table 2.6: Flux ratios the 86 GHz SiO peak, the 8 μm IR flux and the 43 GHz SiO peak flux.

Object	$F_{86GHz}/F_{8\mu m}$	F_{43GHz}/F_{86GHz}	Ref. 43 GHz
FMR2006 1	...	0.76	(1)
FMR2006 3	...	...	
FMR2006 4	...	0.89	(1)
FMR2006 13	0.18	0.89	(1)
Name X18	0.90	0.95	(1)
Cl* Stephenson 2 DFK 2	0.08	1.26	(2)
Cl* Stephenson 2 DFK 49	0.82	0.95	(2)
Cl* Stephenson 2 DFK 1	0.10	0.35	(2)
MY Cep	0.09	1.38	(3)
W Per	...	0.41	(4)
S Per	...	0.21	(5)
MDI2009 GLIMPSE13 1	0.07	0.41	(2)
Cl Trumpler 27 1	0.33	0.16	(6)
IK Tau (Mira)	...	1.22	(7)
U Her (Mira)	...	0.37	(7)

Columns are (from left to right) designation of red supergiant, SiO(86 GHz peak flux)/IR(8 μm flux) ratio (see Alcolea et al. 1990), SiO(43 GHz peak flux)/SiO(86 GHz peak flux) ratio, and the reference of the 43 GHz peak flux. The 8 μm fluxes are taken from the MSX and GLIMPSE catalogue. Sources without measurements were not included in these surveys, or saturated in GLIMPSE. References are:
(1) Nakashima & Deguchi (2006)
(2) Deguchi et al. (2010)
(3) Nakashima & Deguchi (2007)
(4) Jiang et al. (1996)
(5) Cho et al. (1996)
(6) Hall et al. (1990)
(7) Kim et al. (2010)

The J, H, K measurements provided by 2MASS are simultaneously taken, as well as the SPITZER/IRAC measurements. As a result, the $Q2$ parameter, which is more sensitive to mass-loss than the $Q1$ parameter, is more uncertain because of non-simultaneity of the 2MASS and GLIMPSE data. AGB stars may have amplitudes up to 2 mag in K-band (Messineo et al. 2004), while RSG stars typically vary only a few tenths of a magnitude in K-band (Yang & Jiang 2011).

A plot of the $Q1$ versus $Q2$ parameters of the targeted RSG stars is shown in Fig. 2.3. The plot shows that with our sensitivity we were able to detect masers only in stars with $Q2$ values smaller than -3. This means that SiO maser emission was detected toward the reddest sources and the strongest mid-infrared sources. The detection of

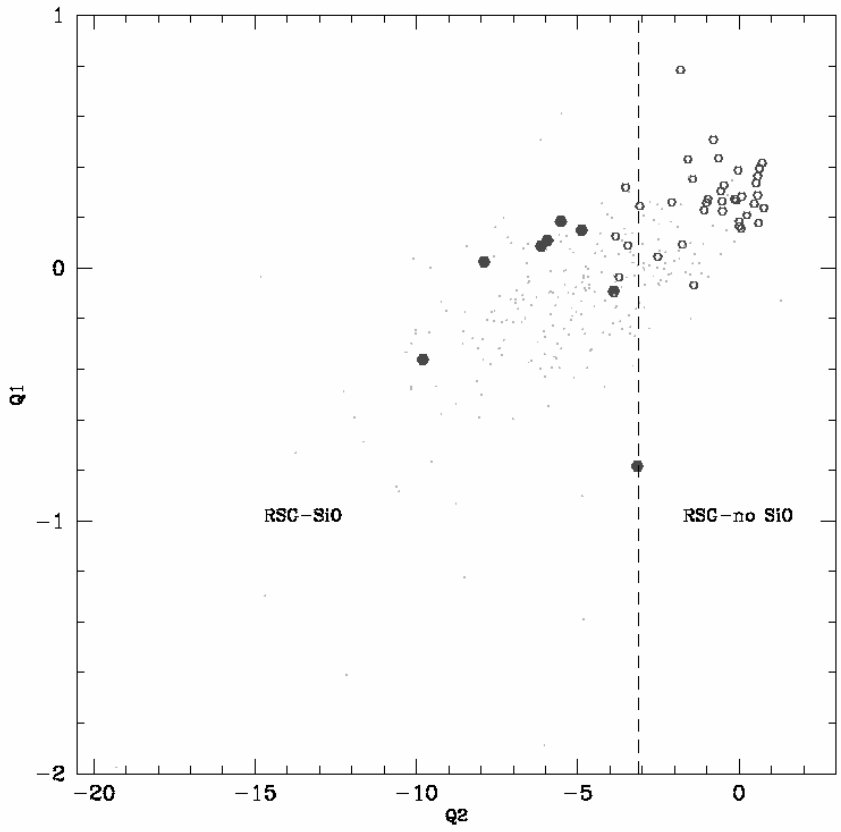

Figure 2.3: The two extinction-free parameters Q1 and Q2 are plotted. Small dots indicate SiO maser detections by Messineo et al. (2002). Empty hexagons are our targeted RSGs without maser detections, and filled hexagons are those with maser emission.

the reddest sources supports a radiative pumping mechanism for the SiO masers in the detected RSG stars (Alcolea et al. 1990).

As a comparison, the SiO masing sample by Messineo et al. (2002) is also plotted in Fig. 2.3. Data are taken with the same telescope and same integration time, therefore directly comparable. However, the sample of Messineo et al. (2002) is mostly composed of stars with lower luminosities (class III), Mira-like stars (Messineo et al. 2004, 2005). The suggested shift in colors between the threshold for SiO masing Miras and SiO masing RSG stars suggests that higher mass-loss rates are required for SiO masing RSG stars. Perhaps, the higher luminosities of RSGs push the dust condensation radius and masing shell farther out. Mass-loss is indeed proportional to density and enve-

lope size (see equation A3 in Sevenster 1999). A large statistics is needed to confirm this suggested color threshold. Alcolea et al. (1990) already noticed that RSGs have generally smaller maser intensity than Mira stars for the same mid-infrared flux.

2.9 Conclusions

We performed an extensive search for the SiO ($v = 1$, $J = 2-1$) maser line at 86 GHz in 88 (candidate) red supergiants in Galactic open clusters. Several of these stellar clusters were never included in a SiO maser survey before. In total, we detected maser emission from 13 RSGs, 1 of which was a new detection. The measurements provided accurate LSR velocities, which can be used in studies of the Galactic structure. We noticed that the velocity range covered by the SiO maser line was broader for the RSGs than for two Mira variables, which we observed for comparison. The 86 GHz transition was stronger than the 43 GHz transition in 11 out of 14 sources detected in both lines, proving the advantage of the 86 GHz maser in studying this sample of Galactic red supergiants. An analysis of the colors of the targeted RSGs showed that the SiO maser was detected in the reddest stars, and the strongest mid-IR sources. The fact that the masers were found towards the reddest stars, supports the radiative pumping mechanism of the SiO maser.

Max-Planck-Institut
für Radioastronomie

3

VY Canis Majoris

3.1 Introduction

One of the most peculiar stars among the red supergiants is the ultra-luminous hypergiant VY Canis Majoris (VY CMa). Since its first registered observation in the Lalande catalogue of 1801, VY CMa has been studied excessively. Originally, the red object was considered a multiple star. In 1917, using a 7.5 inch meridian circle, Guerin discovered VY CMa's famous nebula (Perrine 1923). Herbig (1972) investigated the polarization of this nebula, and found that the apparent companions of the multiple system were in reality dust condensations in the nebula, scattering the stellar light. This was a first glimpse of the complexity of VY CMa's surroundings.

VY CMa has an effective temperature of 2800 K, based on its spectral type M3/4II (Le Sidaner & Le Bertre 1996). The current mass of the supergiant is estimated around 15 $M_{\odot}$ (Wittkowski et al. 1998), although it may be as high as 50 $M_{\odot}$ (Knapp et al. 1993). The RSG phase is a short evolutionary stage. Being such a massive object, VY CMa is about to explode as a supernova in $\sim 10^4$ yr. Initially, the distance to VY CMa was assumed to be 1.5 kpc, which is the distance to the know cluster NGC 2362 associated with the RSG (Herbig 1972; Lada & Reid 1978). Proper motion measurements of 22 GHz water masers in the circumstellar envelope of VY CMa were consistent with a

distance of 1.5 kpc (Richards et al. 1998). Recently, however, this value had to be reviewed. An astrometric monitoring campaign of the H_2O masers yielded a trigonometric parallax of 0.88 mas, and therefore a new, more accurate distance of $1.14^{+0.11}_{-0.09}$ kpc (Choi et al. 2008). At this distance, VY CMa has a luminosity $L \sim 3 \times 10^5\ L_\odot$, making it one of the most luminous stars known. Apart from this extreme luminosity, VY CMa is also characterized by an intense mass-loss, $\dot{M} \sim$ 2-4 $\times 10^{-4}\ M_\odot$ yr^{-1} (Bowers et al. 1983; Danchi et al. 1994), resulting in a thick circumstellar envelope. Table 3.1 summarizes the basic parameters of VY CMa discussed above.

Table 3.1: Basic properties of VY CMa.

Parameter	Value	Reference
R.A.	$07^h22^m58^s.33$	(1)
Dec.	$-25°46'03''.20$	(1)
Distance	1.14 kpc	(2)
$T_{\rm eff}$	2800 K	(3)
L_*	$3 \times 10^5\ L_\odot$	(2)
R_*	1.2×10^{14} cm	(4)
M_*	15-50 $M_\odot$	(5)
$\dot{M}$	2-4 $\times 10^{-4}\ M_\odot$ yr^{-1}	(6)

References: (1) HIPPARCOS catalogue - Perryman et al. (1997); (2) Choi et al. (2008); (3) Le Sidaner & Le Bertre (1996); (4) Monnier et al. (1999); (5) Wittkowski et al. (1998); Knapp et al. (1993); (6) Bowers et al. (1983); Danchi et al. (1994).

Due to the presence of the circumstellar envelope, the central star is highly obscured. At optical wavelengths, only 1% of the total luminosity is detected (Le Sidaner & Le Bertre 1996). The spectral energy distribution shows a large infrared excess caused by thermal emission from dust grains in the CSE. Smith et al. (2001) presented a SED of VY CMa, based on optical and IR photometry, showing the different contributions to the total observed flux (see Fig. 3.1). The solid line represents the total continuum flux. At 2.3 μm, the CO band, typical for cool luminous supergiants, can be seen in absorption. The 9.7 μm and 18 μm silicate features, expected in the spectrum of this oxygen-rich RSG, are present in emission. The dotted and dashed lines show the influence of the central star and the extended emission, respectively. Clearly, at the shorter optical and near-IR wavelengths, scattered light by circumstellar dust grains contributes largely to the flux, while at longer IR wavelengths thermal emission by hot grains becomes dominant.

The circumstellar envelope of VY CMa harbors a multitude of molecules. To date,

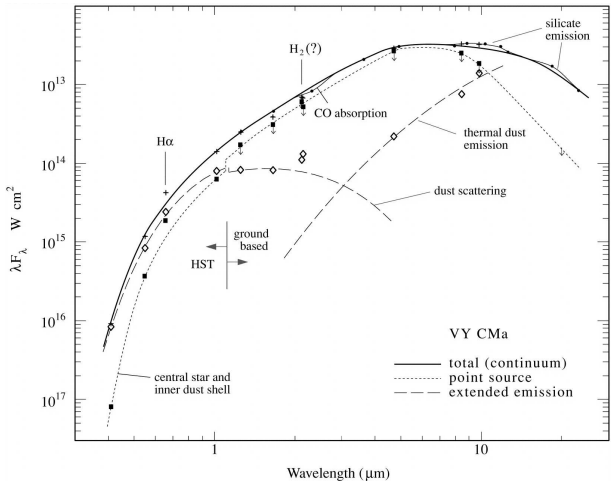

Figure 3.1: SED of VY CMa (Smith et al. 2001). Filled circles and plus signs represent the observations, the solid line shows the total continuum flux. Filled squares and the dotted line denote the flux of the central star. Diamonds and the dashed lines mark the extended emission, divided into scattered light by dust grains at optical and near-IR wavelengths, and thermal dust emission at mid-IR wavelengths.

as many as 18 different molecular species have been identified (Ziurys et al. 2007), among which CO, SiO, SO, SO_2, and more interestingly HCO^+, PN and recently PO, the first detection ever of this species in space (Tenenbaum et al. 2007). Furthermore, strong OH, H_2O and SiO maser emission is present (Eliasson & Bartlett 1969; Knowles et al. 1969; Buhl et al. 1974; Snyder & Buhl 1975). Table 3.2 gives an overview of all molecules detected so far towards VY CMa.

Table 3.2: The 18 molecular species detected in the circumstellar envelope of VY CMa. Molecules marked with a * also show maser emission.

CN	H_2O^*	HCN	NaCl	PN	SiS
CO	H_2S	HNC	NH_3	PO	SO
CS	OH^*	HCO^+	NS	SiO^*	SO_2

3.2 Asymmetry of the circumstellar envelope

Observations show an important characteristic of VY CMa's envelope: it is not spherically symmetric! Optical and near-infrared studies of the circumstellar material reveal a highly asymmetric nebula with several arc-like structures and bright spots (Monnier

et al. 1999; Smith et al. 2001). Thermal-infrared images, however, show more symmetric, though slightly elongated, emission (Smith et al. 2001). Fig. 3.2, 3.3 and 3.4 illustrate the observed structure of the circumstellar envelope, going from optical to IR wavelengths.

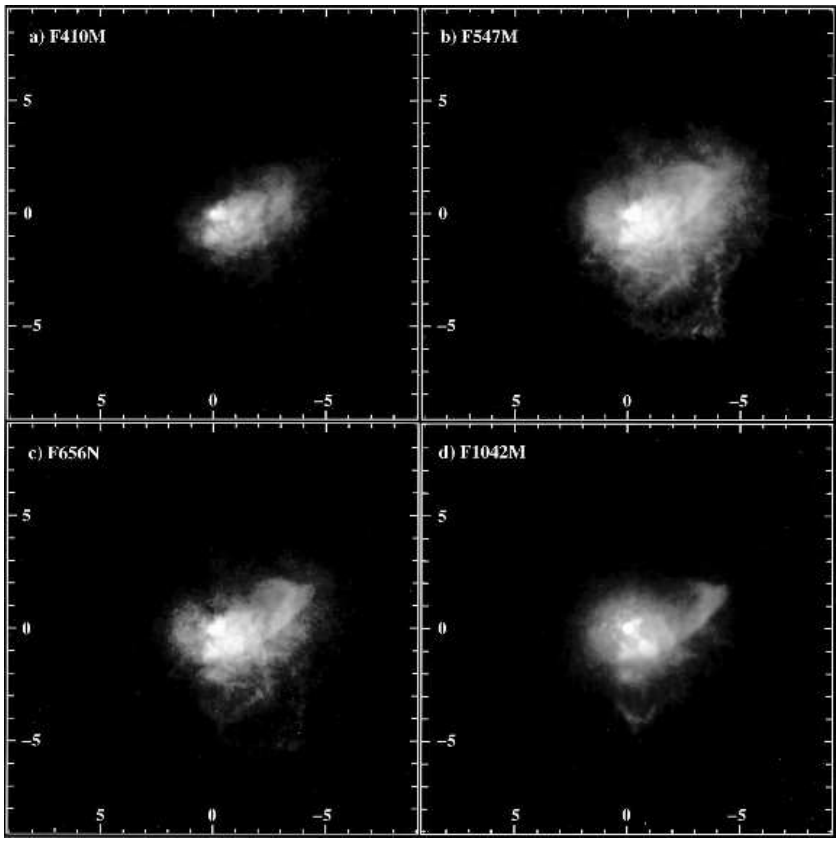

Figure 3.2: HST/WFPC2 images of VY CMa at 409.01 nm, 547.63 nm, 656.37 nm and 1018.35 nm (Smith et al. 2001). The axes denote right ascension (horizontal) and declination (vertical) offset from the central star position in arcseconds.

The optical images of Fig. 3.2, obtained with the Hubble Space Telescope (HST), beautifully show the asymmetry of VY CMa's surroundings. The nebula is brightest south and west of the central star. At the shortest observed wavelength (Fig. 3.2*a*), the northeastern part even seems to be missing completely. Close to the star, several bright knots can be distinguished. Three large reflection arcs are also clearly present: two to the south and southwest, and one to the northwest. This northwestern arc had been discovered and described long before by Herbig (1972), who named it the "curved nebulous tail". The curved nebulous tail appears as well in the near-IR images (Fig. 3.3),

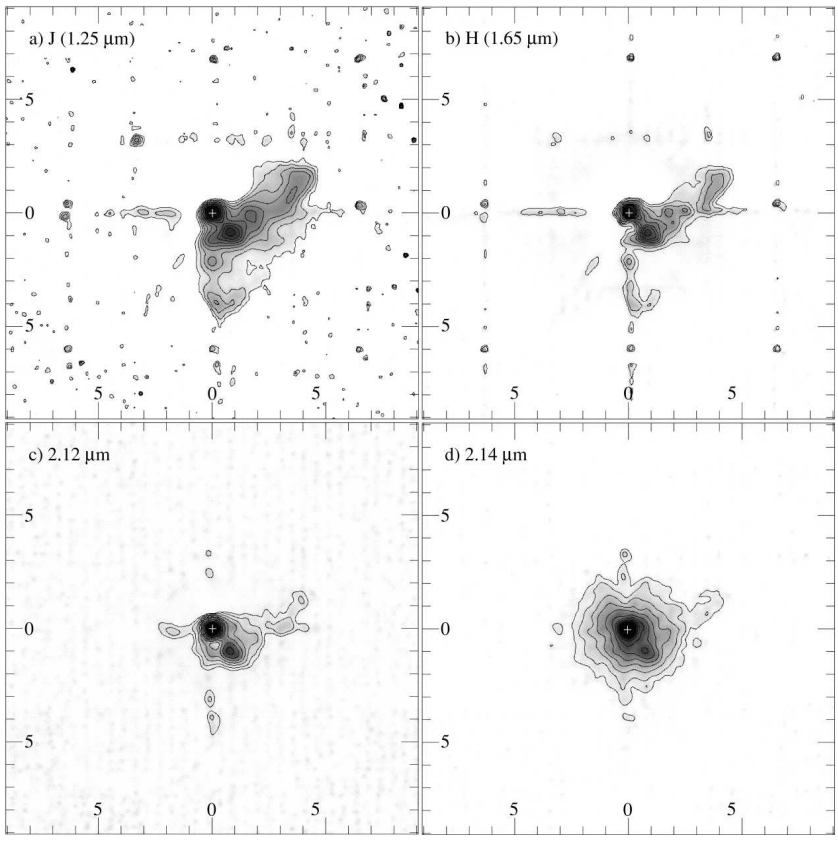

Figure 3.3: Near-IR adaptive optics images of VY CMa (Smith et al. 2001). The axes denote right ascension (horizontal) and declination (vertical) offset from the central star position in arcseconds.

although only at the shortest wavelengths (i.e. 1.25 μm and 1.65 μm). Moving towards mid-IR wavelengths (Fig. 3.4), where thermal emission from warm dust dominates, the images become more symmetric, though elongated in an east-west direction. Fig. 3.5 summarizes the individual structures in VY CMa's nebula, seen at different wavelengths.

The asymmetric appearance of the circumstellar envelope has been attributed to a bipolar outflow or a disk surrounding VY CMa. Herbig (1970a) was the first to introduce the idea of such a thick, equatorial disk of cool gas and dust. Based on the recent optical and IR images of Fig. 3.2–3.4, the disk probably has a northeast-southwest polar axis and is tilted with the southwest lobe closer to us (Monnier et al. 1999; Smith et al. 2001). The apparent absence of emission northeast of the central star in the optical HST images (Fig. 3.2) is a consequence of high extinction in this region, combined

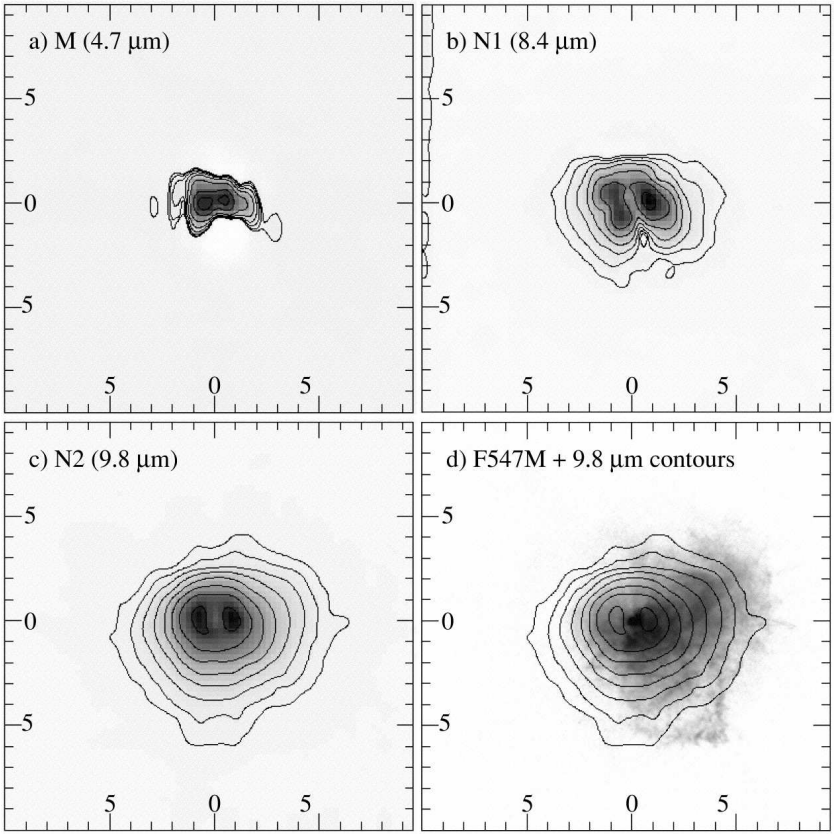

Figure 3.4: Mid-IR images of VY CMa (Smith et al. 2001). The axes denote right ascension (horizontal) and declination (vertical) offset from the central star position in arcseconds.

with backscattering by dust. The so-called "curved nebulous tail", as well as the other arc-like structures, are likely to be produced by localized ejection events. Smith et al. (2001) infer that VY CMa must have undergone a period of enhanced mass-loss over the past 1000 yr. A more detailed study, focusing on the CO rotational lines, explores the complete mass-loss history of VY CMa, and shows that it indeed experienced enhanced mass-loss during the past 1400 yr (Decin et al. 2006). Moreover, around 1000 yr ago, a short ($\sim$ 100 yr), strong peak in the mass-loss rate appears. This was probably the ejection event that created the southwestern arc (*"arc#1"* in Fig. 3.5).

Maser observations also provide indications for the existence of an equatorial disk and bipolar outflow (e.g. van Blerkom 1978; Morris & Bowers 1980). The 1612 MHz OH maser shows a double-peaked profile, and interferometric maps reveal an elongation in the north-south direction. This can be interpreted in terms of a tilted, expanding thick disk (Bowers et al. 1983). H_2O masers at 22 GHz, on the other hand, are elongated

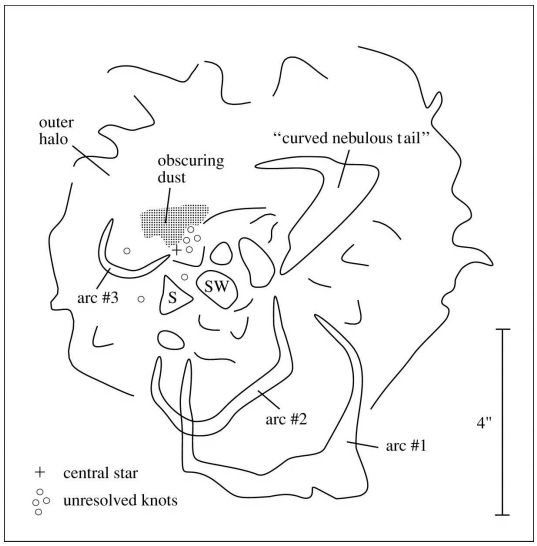

Figure 3.5: Schematic overview of the structures in the envelope of VY CMa, seen at optical and IR wavelengths (Smith et al. 2001).

mainly in an east-west direction, similar to the infrared dust emission. Proper motions are consistent with a bipolar outflow (Richards et al. 1998). Finally, SiO maser profiles are triple-peaked, which can again be explained by an equatorial disk (van Blerkom & Auer 1976).

Several attempts have been made to model the complicated circumstellar envelope of VY CMa, trying to understand its geometrical structure and chemical composition. In the following, we give an overview of existing models. We distinguish between models based on dust, respectively gas properties.

3.3 Models based on dust characteristics

3.3.1 Herbig (1970a,b)

Herbig originally introduced the idea of an expanding equatorial disk (see Fig. 3.6) to explain peculiar optical spectroscopic features of VY CMa, for instance the double-peaked profile of the 1612 MHz OH emission line (Herbig 1970a). In his subsequent paper, he used the same geometry to model the spectral energy distribution between 0.36 μm and 22 μm (Herbig 1970b). The radiative transfer equations are solved under the assumption of grey dust particles, for different radial density distributions and geometrical thickness of the disk. He finds that the disk model fits the observed continuum spectrum well. The disk has a temperature of 1500-1800 K at the inner boundary,

which decreases till 350 K at the outer edge.

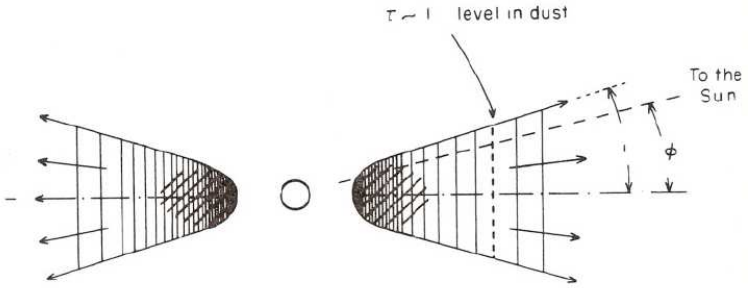

Figure 3.6: Sketch of the disk model proposed by Herbig (1970a,b). VY CMa is surrounded by a thick expanding equatorial disk of grey particles.

3.3.2 Efstathiou & Rowan-Robinson (1990)

VY CMa was used as a test object for the radiative transfer code of Efstathiou & Rowan-Robinson (1990). They developed a method to solve the radiative transfer equation for an axisymmetric distribution of dust around a compact central source, more specifically a flared disk. For simplicity reasons, only a single grain species is considered, in this case dirty silicate grains. VY CMa is represented by a blackbody of temperature $T = 3000$ K. The density distribution in the disk, for which the opening angle is fixed at 45°, is given by

$$n(r, \Theta) \propto r^{-\beta}\, \Theta^{-\gamma} \tag{3.1}$$

in spherical polar coordinates (r, Θ). The best model fit to the SED of VY CMa was found for $\beta = 2$ and $\gamma = 0$, and a viewing angle of 43°. This means we are looking almost right through the outer layers of the flared disk.

3.3.3 Harwit et al. (2001)

Harwit et al. (2001) assumed a spherically symmetric geometry to model the infrared ISO-SWS (Infrared Space Observatory - Short Wavelength Spectrometer) and LWS (Long Wavelength Spectrometer) continuum spectrum of VY CMa. They used a mixture of dust types, consisting mainly of metallic iron and amorphous silicates, and to a lesser extent crystalline silicates. The density follows a simple power law

$$\rho(r) \sim r^{-2}. \tag{3.2}$$

The radiative transfer code MODUST was used to calculate the spectral fit. Even though they considered their model only as a “toy model”, realizing the many shortcomings of a spherically symmetric model to describe VY CMa’s envelope, the results are surprisingly good, as can be seen from Fig. 3.7.

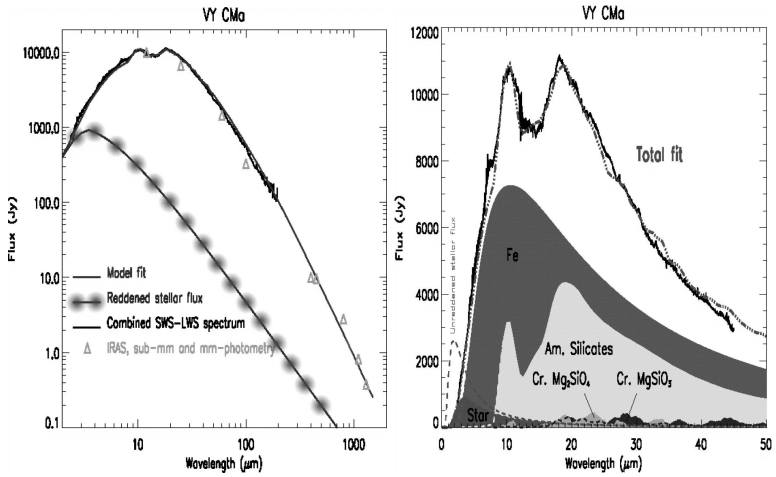

Figure 3.7: *Left*: ISO-SWS and ISO-LWS data of VY CMa (thick line), together with IRAS data and ground-based millimeter and submillimeter data (triangles). The model fit by Harwit et al. (2001) is shown as the smooth solid line. *Right*: Infrared continuum spectrum of VY CMa, with the contributions of the different dust components.

3.4 Models based on gas characteristics

3.4.1 Harwit & Bergin (2002)

Harwit & Bergin (2002) observed the 557 GHz water vapor emission line in VY CMa with the Submillimeter Wave Astronomy Satellite (SWAS). They studied the line shapes and tried to fit several models, based on the biconical structure shown in Fig. 3.8. Inclination and opening angle are varied. Since none of these biconical outflow models were able to reproduce the observed line profiles, they also derived the results for an optically thick disk. First, they calculated the line shapes for a spherically symmetric and a biconal model, and next they subtracted the biconal outflow from the spherical in order to obtain an optically thick disk.

In Fig. 3.9, the observed 557 GHz water vapor line is presented, together with some results for 3 different models: spherically symmetric (solid line), a disk viewed edge-on (dashed line) and a disk inclined at 43° (dotted line). This last model corresponds to

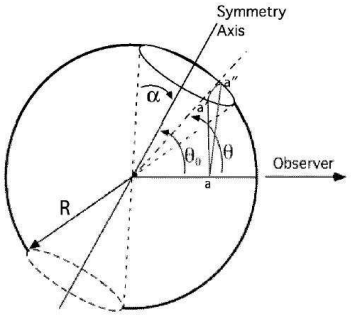

Figure 3.8: Geometry of the biconical model of Harwit & Bergin (2002). The angle θ_0 represents the tilt of the outflow towards the line-of-sight, α denotes the opening angle.

the geometry proposed by Efstathiou & Rowan-Robinson (1990) (see Sect. 3.3.2). Fig. 3.9 shows that the spherically symmetric model and the disk viewed edge-on actually give better results.

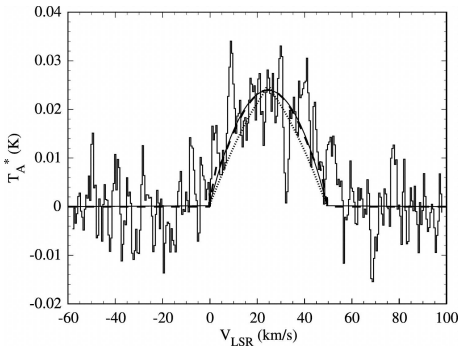

Figure 3.9: The 557 GHz water vapor line of VY CMa observed with SWAS (Harwit & Bergin 2002). Three model fits are shown: a spherically symmetric model (solid line), a disk viewed edge-on (dashed line) and a disk viewed at an inclination angle of 43° (dotted line). The inclined disk was suggested by Efstathiou & Rowan-Robinson (1990) (see Sect. 3.3.2).

3.4.2 Muller et al. (2007)

Muller et al. (2007) obtained 1.3 mm continuum and ^{12}CO(2-1), ^{13}CO(2-1) and SO(6_5-5_4) line emission with the Submillimeter Array (SMA). Channel maps reveal 3 emission peaks, a blueshifted one (-5 km s^{-1}) to the east, a peak centered on the stellar position at the systemic velocity of VY CMa (22 km s^{-1}), and a redshifted peak (45 km s^{-1}) to the west of the star (see Fig. 3.10, *left*). This leads them to construct a model consisting of 2 kinematic components:

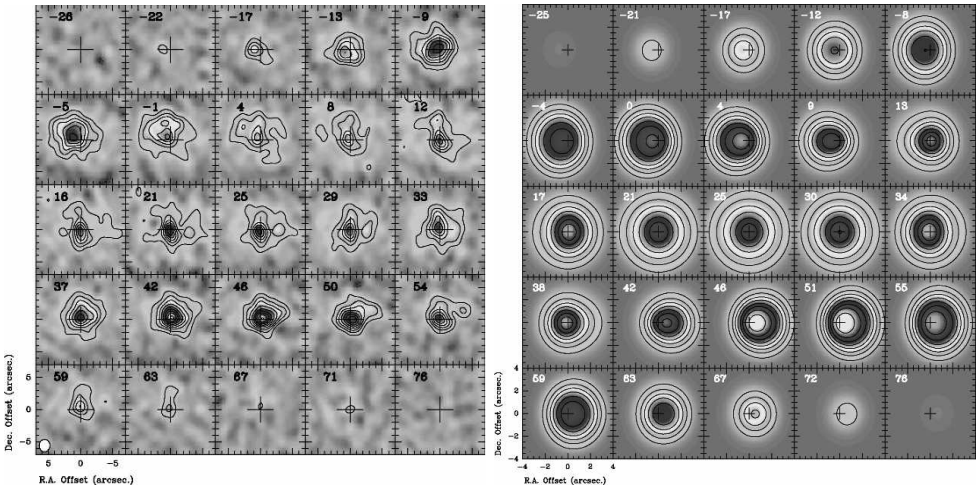

Figure 3.10: *Left*: Channel maps of ^{12}CO(2-1) observed with the SMA (Muller et al. 2007). The velocity of each channel (km s^{-1}) is indicated in the top left corner. Contours are separated by 0.55 Jy/beam, corresponding to 3.9 K. The synthesized beam is shown in the bottom left corner. *Right*: Predicted channel maps of the CO(2-1) emission.

1) a slowly expanding, spherically symmetric shell (15 km s^{-1});

2) a high-velocity bipolar outflow (45 km s^{-1}) with a wide opening angle of 120°, oriented in the east-west direction.

The geometry of the model is illustrated in Fig. 3.11.

Muller et al. (2007) assume a less common H_2 density distribution for the spherical envelope, slightly different from the one for constant mass-loss:

$$n(r) = 4.5 \times 10^5 \, (10^{16} \text{ cm}/r)^{2.5}. \tag{3.3}$$

For the bipolar outflow, a constant H_2 density is taken in the inner region. They introduce a density enhancement towards the outer part, in order to explain the presence of strong emission peaks at larger velocity offsets. This results in the following density distribution for the outflow:

$$n(r) = \begin{cases} 6 \times 10^4 \text{ cm}^{-3} & \text{for} \quad R_{\text{lobe}} < r < 5 \times 10^{16} \text{ cm} \\ 10^5 \text{ cm}^{-3} & \text{for} \quad 5 \times 10^{16} \text{ cm} < r < 7 \times 10^{16} \text{ cm} \\ 10^5 \, (7 \times 10^{16} \text{ cm}/r)^2 \text{ cm}^{-3} & \text{for} \quad r > 7 \times 10^{16} \text{ cm} \end{cases} \tag{3.4}$$

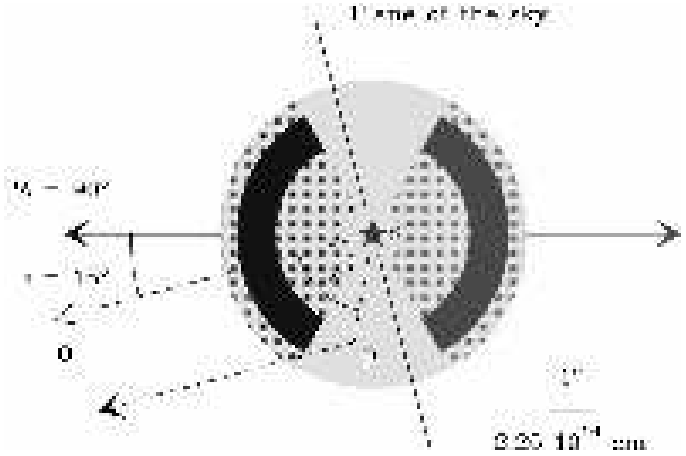

Figure 3.11: Geometry of the model proposed by Muller et al. (2007). The central star is surrounded by a slowly expanding, spherically symmetric envelope (light gray), and a high-velocity bipolar outflow (dotted region). The bipolar lobes contain a density enhancement (filled parts). The outflow has a wide opening angle of 120° and has an inclination angle of 15° with respect to the line-of-sight.

The kinetic temperature profile is given by $T(r) \propto r^{-0.7}$.

Fig. 3.10 (*right*) and 3.12 give some results. In Fig. 3.10, CO(2-1) model channel maps convolved with the corresponding Gaussian beam are shown along the observed maps. Clearly, the 3 observed emission peaks are also present in the model maps. Fig. 3.12 contains the results for the CO spectral lines. The solid lines show the JCMT spectra obtained by Kemper et al. (2003), the dotted lines are the outcome of the model of Muller et al. (2007). Again, both agree nicely.

3.4.3 Ziurys et al. (2007, 2009)

Ziurys et al. (2007) reported the detection of emission from a number of molecular species toward VY CMa, including NaCl and PN, both of which had before only been seen in the exceedingly prolific (carbon-rich) circumstellar envelope of IRC+10216. Most remarkably, they detected HCO^+ emission, which had been predicted to be detectable toward O-rich CSEs (Nercessian et al. 1989), but had only been found toward one such object, the protoplanetary nebula OH231.8+4.2 (Morris et al. 1987). Inspection of their spectra learns that different molecules trace different regions of the envelope: a spherical outflow, with a blueshifted and a redshifted expansion. Certain molecules (e.g. SiO) are only present in the spherical wind. Others, like SO_2, show the typical double-peaked profile of the blue- and redshifted flows. A last group, with SiS

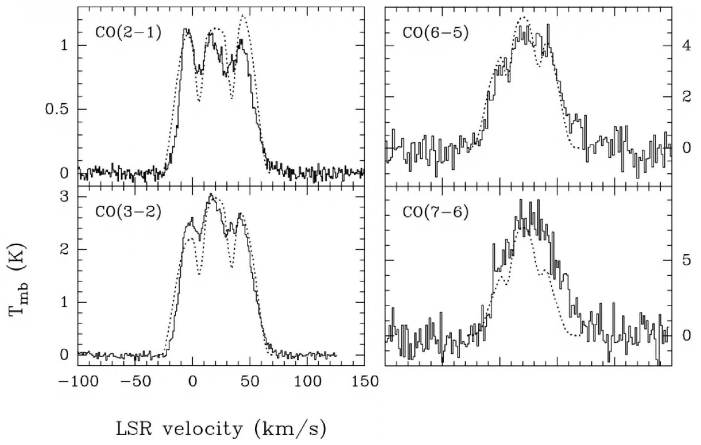

Figure 3.12: Spectra of the CO(2-1), CO(3-2), CO(6-5) and CO(7-6) lines obtained with the JCMT (Kemper et al. 2003) (solid lines). The model fit of Muller et al. (2007) is also shown (dotted lines).

and CO, is found in all three components of the envelope. Some example spectra are shown in Fig. 3.13.

Ziurys et al. (2009) consider a model consisting of a spherically symmetric envelope and a blue- and redshifted outflow. Both flows have an opening angle of 45°, but they have different expansion velocities and inclination angles with respect to the line-of-sight (resp. 38 km s^{-1} and 20° for the blue jet, and 42 km s^{-1} and 45° for the red). They also assign different chemical properties to each flow. The spherically symmetric radiative transfer code of Bieging & Tafalla (1993), adapted for the conical geometry of VY CMa's envelope, is used to calculate abundances, relative to H_2 (with the H_2 column density derived from the star's mass-loss rate), for 6 carbon-bearing molecules (CO, HCN, HNC, CS, HCO^+, CN). The modeling is carried out separately for each of the 3 regions. For the blue- and redshifted flows, a spherically symmetric envelope is assumed in the statistical equilibrium calculations. Next, only the conical parts of the envelope are convolved with the telescope beams, instead of the whole spherical structure.

The density distribution used in their modeling is given by

$$\rho(r) = \frac{\dot{M}}{4\pi v_{\exp}(1 - \frac{R_*}{r})r^2}. \tag{3.5}$$

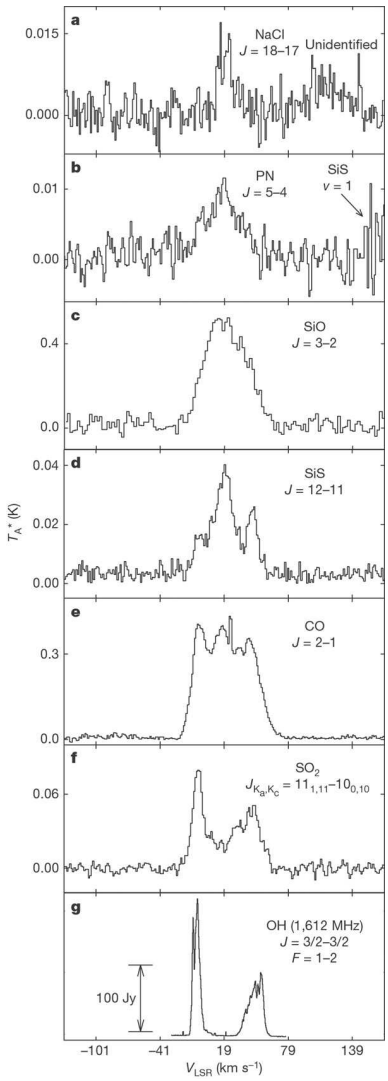

Figure 3.13: Spectra of VY CMa, observed with the Arizona Radio Observatory's Submillimeter Telescope (ARO SMT) by Ziurys et al. (2007).

The gas temperature is determined by the following expression:

$$T_{gas}(r) = 230\left(\frac{10^{16}}{r}\right)^{\gamma}. \tag{3.6}$$

For the spherical part of the outflow, γ is calculated to be 0.62. No values are mentioned for the blue- and redshifted parts. Fig. 3.14 shows the result for CO(2-1).

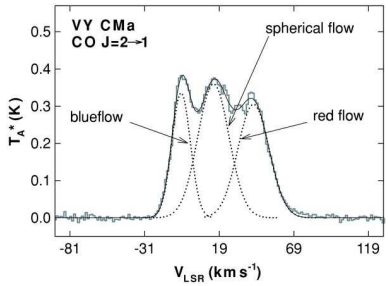

Figure 3.14: Spectrum of CO(2-1) observed with the ARO SMT (blue line). The dotted lines show the contribution of each of the 3 components of the envelope of VY CMa (spherical, blue- and redshifted). The line profile resulting from the modeling of Ziurys et al. (2009) is plotted as the solid black line.

3.5 Dust Composition

Several authors have studied the dust composition of VY CMa, or red supergiants in general. We mention two important works.

3.5.1 Harwit et al. (2001)

The spherically symmetric model used by Harwit et al. (2001) was discussed in Section 3.3.3. As mentioned before, they concentrated on a mixture of dust types: metallic iron, amorphous silicates (Mg-rich olivines) and crystalline silicates (Mg_2SiO_4 and $MgSiO_3$). They applied the radiative transfer code MODUST to calculate the model spectrum. Table 3.3 lists the parameters used for their best-fit model shown in Fig. 3.7. Metallic iron (55%) is the main dust constituent, 41% of the dust consists of amorphous silicates and crystalline silicates represent only 4%.

3.5.2 Verhoelst et al. (2009)

Verhoelst et al. (2009) used the ISO-SWS spectra of 27 RSG stars to study the typical dust composition in these objects. They selected 6 different dust species based on previous results from the literature: alumina, melilite, olivine, MgFeO, metallic iron and carbon (see Table 3.4). They make use of the spherically symmetric radiative transfer code MODUST to model the envelopes of the 27 RSGs with 5 of the selected dust species. Metallic iron is not included in the modeling, since its influence would be similar to that of amorphous carbon. The authors therefore decided to only consider carbon, although it could easily be substituted with iron. The best-fit parameters for each object are shown in Table 3.5. Melilite and alumina are the most important dust

Table 3.3: Dust parameters used in the modeling of Harwit et al. (2001).

Parameters	Metallic Fe	Amorphous silicates	Crystalline Mg_2SiO_4	Crystalline $MgSiO_3$
Inner radius (R_*)	60	25	60	20
Outer radius (R_*)	1500	1550	1000	500
$N_{r,o}$ (g cm^{-3})	3×10^{-20}	9×10^{-20}	2.7×10^{-22}	4.5×10^{-20}
Particle radius, a (μm)	0.01-1	0.01-5	0.01-1	0.01-1
Grain density (g cm^{-3})	7.87	3.10	3.33	2.80
Dust temperature (K)	110-630	50-440	90-360	60-170
Total dust mass ($M_\odot$)	9.4×10^{-3}	6.6×10^{-3}	5.4×10^{-5}	5×10^{-4}
Relative percentage (%)	55	41	1	3

Table 3.4: Dust species used in the modeling of Verhoelst et al. (2009).

Name	Composition	Lattice structure	Size ($N(\alpha) \sim \alpha^{-3.5}$)
Alumina	Al_2O_3	amorphous	0.01-1 μm
Melilite	$Ca_2Al_2SiO_7$	amorphous	0.01-1 μm
Olivine	$Mg_{0.8}Fe_{1.2}SiO_4$	amorphous	0.01-1 μm
MgFeO	$Mg_{0.1}Fe_{0.9}O$	amorphous	0.01-1 μm
Metallic iron	Fe	crystalline	0.01-1 μm
Carbon	C	amorphous	0.01-1 μm

components, followed by olivine. MgFeO and carbon only represent a small fraction of the dust. Verhoelst et al. (2009) also observed PAHs in 4 of their sources.

Table 3.5: The best-fit model parameters of Verhoelst et al. (2009).

Source	Spectral type	$T_{\rm eff}$ [K]	Melilite mass frac	Olivine mass frac	Alumina mass frac	$Mg_{0.1}Fe_{0.9}O$ mass frac	Carbon mass frac
NR VUL	K3Iab	4015	0.56	0.19	0.24	0.00	0.013
IRC +40427	M1:Iab	3745	0.43	0.00	0.55	0.00	0.018
HD 14404	M1Iab	3745	0.48	0.00	0.48	0.04	0.007
α SCO	M1.5Iabb	3710	0.74	0.09	0.12	0.00	0.049
μ CEP	M2Ia	3660	0.31	0.27	0.41	0.00	0.020
HD 90586	M2Iab/Ib	3660	0.57	0.14	0.23	0.05	0.011
α ORI	M2Iab	3660	0.64	0.16	0.20	0.00	0.001
HR 1939	M2Iab	3660	0.82	0.01	0.16	0.00	0.003
YZ PER	M2Iab	3660	0.60	0.14	0.26	0.00	0.003
HD 14826	M2Iab	3660	0.42	0.05	0.52	0.00	0.005
HD 14242	M2Iab	3660	0.59	0.00	0.34	0.05	0.017
V354 CEP	M2.5Iab	3615	0.57	0.14	0.28	0.00	0.008
BD+35 4077	M2.5Iab	3615	0.78	0.03	0.16	0.02	0.010
AD PER	M2.5Iab	3615	0.59	0.03	0.34	0.02	0.017
RW CYG	M3Iab	3605	0.53	0.17	0.30	0.00	0.002
PZ CAS	M3Iab	3605	0.40	0.30	0.30	0.01	0.002
SU PER	M3Iab	3605	0.39	0.19	0.39	0.03	0.008
U LAC	M4Iab:e	3535	0.25	0.44	0.25	0.01	0.053
W PER	M4.5Iab	3535	0.09	0.27	0.63	0.00	0.009
S PER	M4.5Iab	3535	0.03	0.27	0.68	0.01	0.022
RS PER	M4Iab	3535	0.42	0.21	0.31	0.04	0.017
R CEN	M5IIevar	3450	0.33	0.06	0.60	0.00	0.009

Max-Planck-Institut
für Radioastronomie

4

Modeling the spectral energy distribution of VY CMa

4.1 Introduction

In this chapter we study the spectral energy distribution of VY CMa. Dust particles located in the circumstellar envelope absorb the stellar photons and reemit them at longer IR wavelengths. Therefore, the SED is dominated by a huge infrared excess. In order to understand the absorption and emission processes taking place in the CSE, and their effects on the observed continuum spectrum, we will first take a look at the theory of radiative transfer in Section 4.2. Next, we will present three different methods to model the spectral energy distribution. In Section 4.4 we start with a simple spherically symmetric geometry and a basic Monte Carlo program. However, as discussed in the previous chapter, VY CMa has a rather complex envelope and spherical symmetry is not a realistic assumption. Therefore, in Sections 4.5 and 4.6 we introduce a dusty disk around VY CMa. Two different approaches to solving the radiative transfer problem are described: LELUYA and MCMax. We give a short overview of the theory behind these two methods, and present the results of the model fitting. Finally, in Section 4.7 we summarize our findings.

4.2 Radiative transfer

If one wants to study an astronomical object embedded in a dusty environment, it is essential to understand the theory of radiative transfer. Observational data of such an object do not directly represent the radiation as it leaves the source. Photons are absorbed, emitted and scattered, thereby changing direction and frequency, before they reach the observer. The radiative transfer equation describes exactly how the radiation behaves when traveling through a dusty medium. Solving this equation is not always straightforward, though of high importance for instance when modeling the observed source. Only after the radiative transfer equation has been applied to the model spectrum, can it be compared to the observations to examine the accuracy of the model.

VY CMa, as red supergiants in general, is surrounded by a dusty envelope (see Chapters 1 and 3). Evidence for the dust can be found in the infrared excess that is typically present in the spectral energy distribution of these objects. As described above, in order to model VY CMa's envelope, we need to find a solution for the radiative transfer equation.

In this section, we will introduce the basic concepts of the theory of radiative transfer. The section is based on the textbooks by Rybicki & Lightman (1979), Peraiah (2001), Rutten (2003) and Krügel (2003).

4.2.1 Specific intensity and flux

Consider a surface area dA with normal unit vector $\vec{n}$. The energy transported through dA within a solid angle $d\Omega$ around the direction $\vec{n'}$ with polar coordinates θ and ϕ, in a time dt and within a frequency range $d\nu$ is given by

$$dE_\nu = I_\nu \cos\theta \, dA \, dt \, d\Omega \, d\nu. \tag{4.1}$$

I_ν is called the specific intensity or brightness. It has dimensions erg s^{-1} cm^{-2} Hz^{-1} $ster^{-1}$. The mean intensity, averaged over all directions, is

$$J_\nu = \frac{1}{4\pi} \int I_\nu \, d\Omega \, . \tag{4.2}$$

This is the zeroth moment of the intensity. The net flux F_ν through a surface area in the direction $\vec{n}$ is related to the first moment of the intensity:

$$F_\nu = \int I_\nu \cos\theta \, d\Omega \, . \tag{4.3}$$

The dimensions of F_ν are erg s^{-1} cm^{-2} Hz^{-1}, or Jy.

4.2.2 The transfer equation

When a ray of light travels through a medium, its intensity will generally change. On the one hand, energy will be lost due to extinction, while on the other hand, emission processes will add energy and increase the intensity. We can quantify the intensity gain by introducing the monochromatic emission coefficient j_ν. The intensity added to a beam by local emission per length unit ds is given by

$$dI_\nu = j_\nu \, ds. \tag{4.4}$$

j_ν has units erg s^{-1} cm^{-3} Hz^{-1} ster^{-1}. In the same way, we can define the extinction coefficient α_ν to describe the intensity loss over a distance ds:

$$dI_\nu = -\alpha_\nu \, I_\nu \, ds. \tag{4.5}$$

Note that the loss is proportional to the intensity of the beam. The extinction coefficient α_ν has units cm^{-1}. It can also be written as $\alpha_\nu = \sigma_\nu n$, with σ_ν the monochromatic cross section per particle (cm^2) and n the particle density (cm^{-3}), or as $\alpha_\nu = \kappa_\nu \rho$, with κ_ν the extinction coefficient per unit mass (cm^2 g^{-1}) and ρ the mass density (g cm^{-3}). Since both absorption and scattering cause a decrease in intensity, the extinction coefficient is really a sum of two factors: $\alpha_\nu = \alpha_\nu^{\mathrm{abs}} + \alpha_\nu^{\mathrm{sca}}$.

Combining (4.4) and (4.5), we find the radiative transfer equation, describing the variation of the intensity

$$\frac{dI_\nu}{ds} = -\alpha_\nu I_\nu + j_\nu. \tag{4.6}$$

We define the optical depth τ_ν along a path as

$$d\tau_\nu = \alpha_\nu \, ds, \tag{4.7}$$

so that

$$\tau_\nu(s) = \int_{s_0}^{s} \alpha_\nu(s') \, ds'. \tag{4.8}$$

The optical depth is a measure for the opacity of the medium. When $\tau_\nu > 1$, the medium is called optically thick. Photons are likely to be absorbed along the path. When $\tau_\nu < 1$, the medium is optically thin and photons can travel more easily throughout the medium without being absorbed on the way. Next, we introduce the source function S_ν as the

ratio of the emission and extinction coefficients

$$S_\nu = \frac{j_\nu}{\alpha_\nu}. \tag{4.9}$$

This allows us to rewrite the transfer equation (4.6) as

$$\frac{dI_\nu}{d\tau_\nu} = -I_\nu + S_\nu. \tag{4.10}$$

A formal solution can be obtained if we multiply (4.10) by e^{τ_ν} and integrate by parts, which gives

$$I_\nu(\tau_\nu) = I_\nu(0)\, e^{-\tau_\nu} + \int_0^{\tau_\nu} S_\nu(\tau'_\nu)\, e^{-(\tau_\nu - \tau'_\nu)}\, d\tau'_\nu \tag{4.11}$$

In case of a constant source function S_ν, the solution can easily be simplified to

$$I_\nu(\tau_\nu) = I_\nu(0)\, e^{-\tau_\nu} + S_\nu\,(1 - e^{-\tau_\nu}). \tag{4.12}$$

For instance, under the conditions of local thermodynamic equilibrium (LTE), the source function is equal to the Planck function, $S_\nu = B_\nu(T)$, hence

$$I_\nu(\tau_\nu) = I_\nu(0)\, e^{-\tau_\nu} + B_\nu(T)\,(1 - e^{-\tau_\nu}). \tag{4.13}$$

In general, however, (4.11) is only a formal solution. This can be seen if we assume isotropic scattering, in which case the source function, defined in (4.9), takes the form

$$S_\nu = \frac{\alpha_\nu^{\text{abs}} B_\nu(T) + \alpha_\nu^{\text{sca}} J_\nu}{\alpha_\nu} \tag{4.14}$$

with α_ν the extinction coefficient, made up of the sum of α_ν^{abs} and α_ν^{sca}, respectively the absorption and scattering coefficient, as explained before. Thus, in order to solve (4.11) for I_ν, one needs to know S_ν, which is a function of J_ν according to (4.14), which in turn depends on I_ν itself (see (4.2)). Therefore, in general an analytical approximation or a numerical method is needed to solve the radiative transfer equation.

An approximation that is often used to simplify the numerical computation in case of high optical depth is the Rosseland mean extinction coefficient α_R, defined as

$$\frac{1}{\alpha_R} = \frac{\int \frac{1}{\alpha_\nu} \frac{\partial B_\nu(T)}{\partial T}\, d\nu}{\int \frac{\partial B_\nu(T)}{\partial T}\, d\nu}. \tag{4.15}$$

It is a weighted mean, giving more importance to frequencies with a lower extinction coefficient.

Several methods to solve the transfer equation (4.10) exist. In the rest of this chapter, we will use 3 different radiative transfer codes in our attempt to model the spectral energy distribution of VY CMa. We will explain each method in the corresponding section.

4.3 Data

We searched the literature for available continuum data of VY CMa to construct its spectral energy distribution. Table 4.1 gives an overview of the data we have at our disposal.

Table 4.1: Overview of the data used for the modeling of VY CMa.

Reference	Range	Description
Hyland et al. (1969)	0.36 - 19.5 μm	Mount Wilson, 24 and 60 inch[a]
Low et al. (1970)	0.36 - 22.0 μm	Catalina Observatory, 28 and 60 inch[b]
Smith et al. (2001)	0.41 - 23.0 μm	ESO 3.6 m telescope
IRAS	12/25/60/100 μm	IRAS 12, 25, 60 and 100 μm fluxes
ISO-SWS	2.37 - 45.0 μm	ISO Short Wavelength Spectrometer
ISO-LWS	43.1 - 196.9 μm	ISO Long Wavelength Spectrometer

[a] ~0.6 m and ~1.5 m, respectively
[b] ~0.7 m and ~1.5 m, respectively

The spectral energy distribution resulting from these data is shown in Fig. 4.1. Note that the ISO-SWS data are properly calibrated (Neufeld et al. 1999), while the ISO-LWS data are highly processed data from the ISO archive. Shifts between the different bands can still be seen.

4.4 Monte Carlo radiative transfer

As a first step towards modeling the dust envelope of VY CMa, we study a spherically symmetric Monte Carlo code, in order to familiarize ourselves with the problems of radiative transfer. This will help us in the next phase, when we apply more complex methods to solve the transfer equation. We start by describing the Monte Carlo technique, next we look at some results obtained with the spherical code.

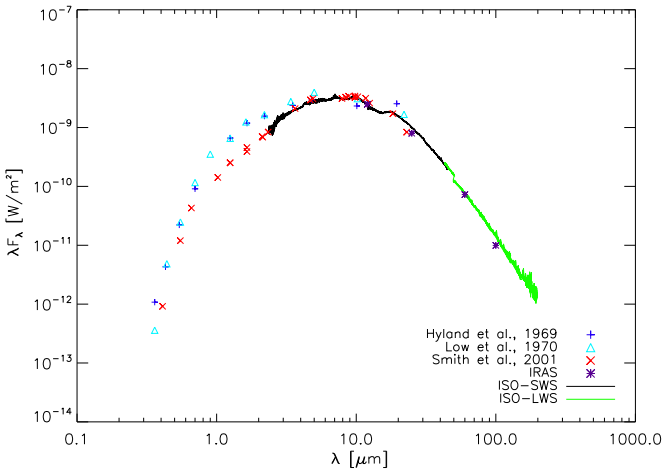

Figure 4.1: Spectral energy distribution of VY CMa, comprised of the data listed in Table 4.1.

4.4.1 The Monte Carlo technique

The basic idea behind the Monte Carlo method of solving the radiative transfer problem, is to follow each packet of photons as it leaves the star, travels through the dusty envelope, gets scattered or absorbed and reemitted on its way, thereby changing direction and/or frequency, until it leaves the envelope and is detected by an observer. Each absorption event leads to an increase of the local temperature, in such way that after all photon packets have escaped, the envelope has reached its radiative equilibrium temperature. The theoretical description given below is based on the work of Lucy (1999), Bjorkman & Wood (2001) and Krügel (2008).

Monte Carlo radiative transfer codes consider packets of photons, rather than focusing on every photon individually. Each packet is made up of a number of photons of the same frequency ν_i, such that all packets have equal energy ε. Therefore, the number of photons per packet, n_i, depends on the frequency according to $\varepsilon = n_i h\nu_i = \text{constant}$. If we take m_γ different frequencies into account, and we let the star emit n_γ packets of each frequency per time unit, the total number of emitted photon packets is $N_{\text{tot}} = n_\gamma m_\gamma$. This means we can write the bolometric luminosity of the source as $L = N_{\text{tot}}\varepsilon$.

The frequencies ν_i ($i = 1, \ldots, m_\gamma$) at which the photon packets are emitted, are determined from

$$\frac{i - \frac{1}{2}}{m_\gamma} = \int_0^{\nu_i} L_\nu \, d\nu \Big/ \int_0^{\infty} L_\nu \, d\nu, \tag{4.16}$$

with $L = \int_0^\infty L_\nu \, d\nu$. The packets leave the star in a random direction, represented by the direction cosine μ, which is set to

$$\mu = -1 + 2\,z, \tag{4.17}$$

with z a random number from the interval $[0, 1]$. This implies an isotropic emission of photon packages. The dusty envelope is placed in a rectangular grid. Each grid cell is characterized by its density ρ, temperature T, absorption coefficient per mass unit $\kappa_\nu^{\rm abs}$, and scattering coefficient per mass unit $\kappa_\nu^{\rm sca}$. Note that the extinction coefficient per mass unit, $\kappa_\nu = \kappa_\nu^{\rm abs} + \kappa_\nu^{\rm sca}$, is related to the extinction coefficient α_ν defined in (4.5) through $\alpha_\nu = \kappa_\nu \rho$. Initially, the temperature is set to zero in all grid cells.

The source emits the photon packets one by one, and each packet is followed on its way. After leaving the star in random direction μ, the packet enters grid cell j. Whether the photon packet will interact with the dust in cell j, depends on the optical depth τ_ν. The optical depth can be calculated from the local density, and the absorption and scattering coefficients as follows:

$$\tau_\nu = (\kappa_\nu^{\rm abs} + \kappa_\nu^{\rm sca})\rho l, \tag{4.18}$$

with l the distance traveled by the photon packet (see (4.7)). If the optical depth is such that

$$d\tau_\nu \geq -\ln(z), \tag{4.19}$$

with z again a random number from the interval $[0, 1]$, the packet will interact with the dust in the cell. Otherwise, it will continue its outward movement uninterrupted in the direction μ, until it reaches the next grid cell.

In case of interaction, there are two possibilities: the photon packet gets either absorbed by the dust particles in the cell, followed by immediate reemission, or it gets scattered. The probability for each event is related to the albedo, the ratio of the scattering and extinction coefficients:

$$A = \frac{\kappa_\nu^{\rm sca}}{\kappa_\nu^{\rm abs} + \kappa_\nu^{\rm sca}} = \frac{\kappa_\nu^{\rm sca}}{\kappa_\nu}. \tag{4.20}$$

Let z once more be a random number from $[0, 1]$, then the photon packet will be scattered if

$$\frac{\kappa_\nu^{\rm sca}}{\kappa_\nu^{\rm abs} + \kappa_\nu^{\rm sca}} > z. \tag{4.21}$$

Else, the packet will be absorbed by the dust particles.

We consider first the more simple situation of scattering. The photon package keeps its original frequency, but continues its path in a new direction μ, assigned in a random

way according to (4.17). The dust within the cell of interaction remains unaltered.

Next, we study the effects of absorption. When the photon packet is absorbed, it will add energy to the envelope, and consequently the temperature in the grid cell will increase. In order to conserve energy and obtain radiative equilibrium, the photon packet must be reemitted immediately, at a new frequency determined by the local temperature, and in a new direction μ given by (4.17). In this way, the temperature throughout the envelope, initially set to zero everywhere, will rise as more and more photon packets get absorbed. After a cell has absorbed k packets, its temperature T_k can be derived from

$$\int \kappa_\nu^{\mathrm{abs}} B_\nu(T_k)\, d\nu = \frac{k\varepsilon}{4\pi\rho v}, \tag{4.22}$$

where $B_\nu(T_k)$ represents the Planck function at temperature T_k, and v the volume of the grid cell. When all the packets have been released, the final temperature has to be equal to the radiative equilibrium temperature. In order to fulfill this requirement, the k-th absorbed photon package has to be reemitted at the smallest frequency ν_i for which

$$\int_0^{\nu_i} \kappa_\nu^{\mathrm{abs}} \left(\frac{dB_\nu}{dT}\right)_{T=T_k} d\nu \geq z \int_0^{\infty} \kappa_\nu^{\mathrm{abs}} \left(\frac{dB_\nu}{dT}\right)_{T=T_k} d\nu, \tag{4.23}$$

where T_k is the new temperature of the cell after the k-th absorption event, determined from (4.22), and z a random number from the interval $[0, 1]$.

After a photon package has undergone an interaction, it travels in its newly assigned direction μ to the next grid cell. The whole process is then repeated, until the packet leaves the envelope and can be registered by an observer. When all photon packets have gone through this cycle and left the cloud, we can construct the spectral energy distribution and temperature structure of the dusty envelope with an embedded source.

4.4.2 First results

Since VY CMa is surrounded by a highly asymmetric, complex circumstellar nebula, no spherically symmetric model will succeed in reproducing the exact spectral energy distribution. This has to be kept in mind when comparing the results of our Monte Carlo modeling with the observed SED. We are not aiming to accurately fitting every feature of this SED, but we merely want to match the general shape and flux level. Once we find a satisfactory fit, we can change some of the model parameters to check their influence, which will give us more insight into radiative transfer. Later, when applying 2-dimensional codes, this knowledge will help us to improve the modeling results.

We used a standard Monte Carlo code written by E. Krügel. VY CMa is represented

by a black body of 2800 K in the center of a rectangular grid. We adopt the standard stellar parameters as given in Table 3.1, i.e. $L = 3 \times 10^5\ L_\odot$ and $d = 1.1$ kpc. Because we assume spherical symmetry, only one octant of the grid has to be considered. This octant, measuring 3×10^{16} cm in each dimension, is divided into $2^8 \times 2^8 \times 2^8$ grid cells. Next, we place the dusty circumstellar envelope in the grid. We assume a standard density distribution, $\rho \propto 1/r^2$. The proportionality constant is adjusted in order to obtain the best visual correspondence between model and observations. Two different dust types are taken into account, silicates and carbonaceous grains, with a size distribution between 0.2 μm and 1 μm. The dust temperature in each grid cell, for both silicates and C-grains, is initially set to zero. Then, we let the star emit 10000 photon packages per cycle, at frequencies determined from (4.16). We repeat this process for 1000 cycles. The resulting SED is shown in the left panel of Fig. 4.2. Although we reach the correct flux level around the 9.7 μm silicate feature, there are still many shortcomings. Below $\sim$2 μm, we underestimate the flux, while our model shows some excess compared to the observations between 2 and 7 μm. From 20 μm on, the flux level of our model SED is again too low to fit the ISO data. Increasing the dust density as to produce more scattering (short wavelengths) and thermal emission (long wavelengths) events didn't help to reduce the underestimation of the flux.

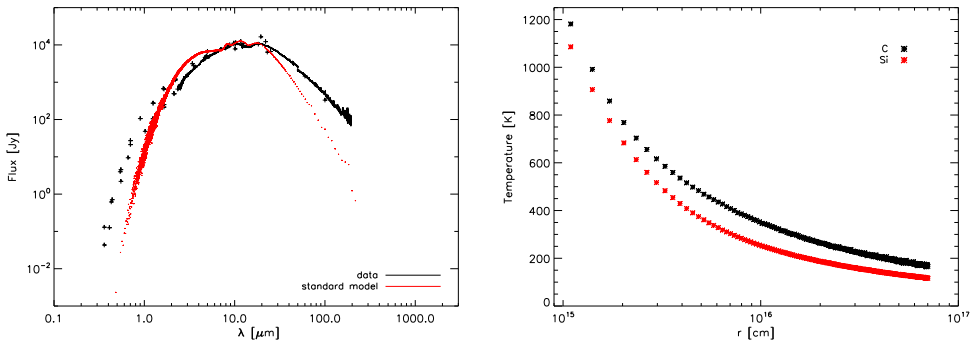

Figure 4.2: *Left*: Best-fit model obtained with a spherically symmetric Monte Carlo radiative transfer code (red), compared to the observed SED of VY CMa (black). *Right*: Temperature distribution of the silicates (red) and carbonaceous dust grains (black) throughout the envelope, calculated for the best-fit SED on the left side.

The Monte Carlo code also gives us information about the temperature distribution throughout the envelope. At the start of the calculations, the temperature was set to zero in all the grid cells. As the program runs through the 1000 cycles, emitting 10000 photon packets every time, absorption processes heat the dust in the grid cells. The final

temperature is determined by the number of absorptions that occurred within the cell, as explained in (4.22). Since the temperature calculated as such depends on the absorption coefficient ($\int \kappa_\nu^{\rm abs} B_\nu(T_k)\, d\nu = \frac{k\varepsilon}{4\pi\rho v}$), each grain species will have its own temperature distribution. The temperature profile resulting from our Monte Carlo transfer program is shown in the right panel of Fig. 4.2.

We changed the important input parameters of our model and inspected the differences in the resulting SEDs. Some examples are given in Fig. 4.3. Luminosity and distance are closely related. An increase in luminosity translates in a logical increase of the flux level, while a decrease of the distance has the same effect. The stellar temperature seems to have few influence on the SED. Changing the density distribution, on the other hand, causes a substantial shift in the spectral energy distribution. Substituting $\rho \propto 1/r^{2.5}$ for the usual $1/r^2$ density distribution produces a similar SED, although the underestimation of the ISO data becomes worse. If we assume a less steep density law ($\rho \propto 1/r^{1.5}$ or even $1/r$), the problem of the overestimation of the flux between 2-7 μm is solved, but we get a huge excess around 10-30 μm. Therefore, we conclude that $\rho \propto 1/r^2$ results in the best-fitting SED, under the assumption of spherical symmetry. It is clear that we will have to drop this assumption if we want to construct a more accurate model of VY CMa's envelope. Thus, in the next section we introduce a different radiative transfer code, which can handle 2-dimensional geometries.

4.5 LELUYA

LELUYA is developed by Dejan Vinković (Vinković 2003) as a 2-dimensional version of the radiative transfer program DUSTY (Ivezić, Nenkova, & Elitzur 1999). It uses a triangular adaptive grid, which traces gradients in dust density and optical depth. The radiative transfer is calculated by solving a matrix equation. The strength of LELUYA is that it can be used to model both SED and images, and it has successfully been applied to IRC+10011 (Vinković et al. 2004). The disadvantage, however, is the huge computational time (up to 4 days/model).

4.5.1 The program

LELUYA aims to solve the radiative transfer equation for an arbitrary axially symmetric two-dimensional dust distribution around a central source. It applies an entirely different strategy than the Monte Carlo approach. The core of LELUYA is the grid generation. Where other radiative transfer codes use a fixed grid, or at most a grid that is adaptive to a certain (low) level, LELUYA generates a completely adaptive, optimal triangular spatial grid that automatically traces dust density and optical depth gradients. Starting with a regular grid, each triangle is split into smaller triangles as long as the

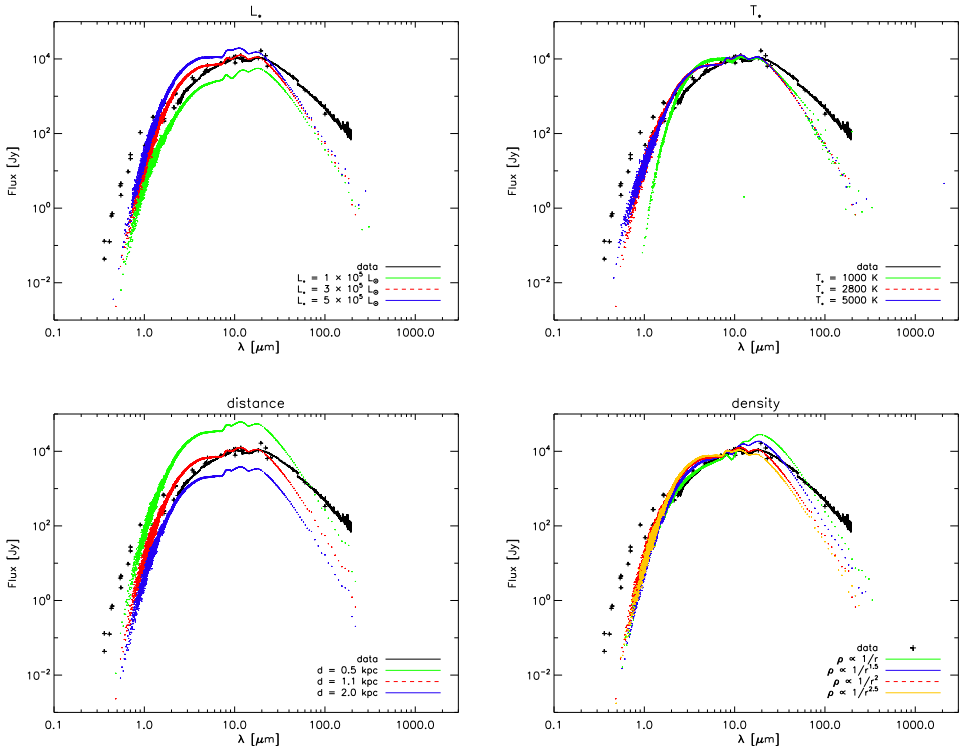

Figure 4.3: Model SEDs calculated with a spherically symmetric Monte Carlo code, showing the influence of L_* (*top left*), T_* (*top right*), the distance to VY CMa (*bottom left*) and the density distribution (*bottom right*). In the legend, the best-fit model of Fig. 4.2 is indicated by the dashed line.

optical depth along its sides is too large. This process is repeated until a refined grid is reached, which reflects regions of sharp changes in optical depth and density. Fig. 4.4 (*left*) shows an example of such a grid generation. On the right panel, the grid used for the modeling of IRC+10011 is displayed (Vinković et al. 2004). The model consists of a bipolar cone within a spherically symmetric dusty wind. The grid clearly traces the density jump between the $1/r^2$ wind and $1/r^{0.5}$ outflow. The angular grid, used to integrate over 4π steradian, is calculated in a similar way.

LELUYA follows the scaling approach introduced by Ivezić & Elitzur (1997). These authors describe how the radiative transfer calculations can be highly simplified when working with dimensionless quantities. Therefore, there will be no need for specifying the real units of e.g. luminosity, dust density or extinction coefficients. All but one important parameters are scaled and become dimensionless. The only parameter that has to be defined is the temperature of dust destruction/creation, in Kelvin. With this

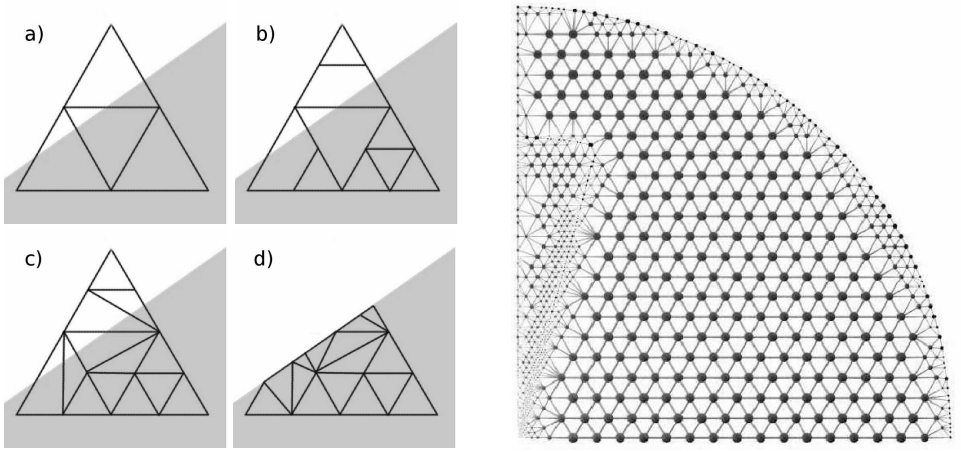

Figure 4.4: *Left*: Example of the generation of an adaptive grid. The triangles are divided into smaller ones, until the optical depth along their sides is below a certain limit. The final grid traces the sharp transition from one dust species to another, represented by the different colors (Vinković 2003). *Right*: The spatial grid used in the LELUYA calculations of IRC+10011. This AGB star has a spherically symmetric dusty wind with a $1/r^2$ density distribution. Within the wind, a bipolar outflow with density $1/r^{0.5}$ is assumed. The grid is automatically refined in such way that the sharp jump in density between wind and cone is traced (Vinković et al. 2004).

temperature fixed, all other parameters can be scaled. For instance, if the spatial position of the dust condensation point is marked $\vec{r}_1$, every other position vector $\vec{r}$ can be scaled as $\vec{\rho} = \vec{r}/|\vec{r}_1|$. Of course, as the true temperature distribution is not known at the beginning of the calculations, the spatial position of the condensation point has to be guessed, and updated after each iteration cycle, as described below. Thus, also the scaling will have to be changed after each cycle.

LELUYA makes use of the formal solution of the transfer equation (4.11). After an additional integration over $d\Omega$, the intensity I_ν is replaced by the mean intensity J_ν (see (4.2)). Furthermore, LELUYA assumes isotropic scattering, which allows to write the source function in terms of J_ν as well (see (4.14)). We also introduce the scaled, dimensionless position vector $\vec{\rho}$ defined above. Altogether, the formal solution (4.11) transforms to

$$J_\nu(\vec{\rho}) = J^*_\nu(\vec{\rho}) + \iint \sum_i \left[\frac{\alpha^{\rm abs}_\nu(\vec{\rho'})}{\alpha_\nu(\vec{\rho'})} B_\nu(T_i(\vec{\rho'})) + \frac{\alpha^{\rm sca}_\nu(\vec{\rho'})}{\alpha_\nu(\vec{\rho'})} J_\nu(\vec{\rho'}) \right] e^{-\tau_\nu(\vec{\rho'},\vec{\rho})} d\tau_\nu(\vec{\rho'},\vec{\rho}) \frac{d\Omega_{\vec{\rho}}}{4\pi}, \tag{4.24}$$

where J^*_ν is the stellar contribution to the mean intensity and T_i is the temperature of the i-th dust species in the dust mixture used by LELUYA. Next, all quantities in (4.24) are replaced by their scaled, dimensionless equivalent. LELUYA splits the formal solution

into two parts, a vector $\mathcal{B}$ which depends on the stellar energy source (J_ν^*) and the dust temperature ($[\alpha_\nu^{\rm abs}/\alpha_\nu]B_\nu(T_i)$), and a $N \times N$ correlation matrix $\mathcal{A}$, which connects all N gridpoints through dust scattering ($\alpha_\nu^{\rm sca}/\alpha_\nu$). We can then rewrite the radiative transfer problem (4.24) as a matrix equation:

$$(1 - \mathcal{A})\,[J_\nu] = \mathcal{B}, \tag{4.25}$$

which is solved for J_ν by matrix inversion.

The program works as follows. First, the initial adaptive grid is calculated. Then, the matrix $\mathcal{A}$ and vector $\mathcal{B}$ are determined, so the radiative transfer equation (4.25) can be solved and the mean intensity J_ν computed. Once the mean intensity is known, the dust temperature can be updated. This is done under the assumption of local thermodynamic equilibrium. In this case, the dust temperature can be derived from the energy balance between radiative heating and cooling:

$$\int \alpha_{\nu,i}^{\rm abs} J_\nu \, d\nu = \int \alpha_{\nu,i}^{\rm sca} B_\nu(T_i) \, d\nu. \tag{4.26}$$

When the dust temperature for each species i has been calculated, the program checks if the luminosity is conserved. Next, the position of the dust sublimation radius has to be updated according to the new dust temperatures. Finally, a new grid is generated and the process is repeated until the temperature converges. LELUYA then provides the SED and 2-dimensional images at a range of wavelengths.

4.5.2 Modeling results

As illustrated in Section 4.4, we need to abandon the assumption of a spherically symmetric envelope around VY CMa, and explore a 2-dimensional geometry. The option offered by LELUYA is an axially symmetric geometry consisting of a flared disk, described by

$$\rho \sim \rho_0 x^{-p} \exp\left(-\frac{h_0\, z^2}{x^{2m}}\right), \tag{4.27}$$

where ρ_0, p, h_0 and m are user defined input parameters. The program also requires a stellar temperature and the temperature of dust sublimation, the outer radius of the envelope, the optical depth in the equatorial plane and the dust composition. We used a mixture of carbonaceous grains and silicates. The major drawback of LELUYA is the long computational time. One model calculation easily takes up to 4 days. Therefore, we could not scan the parameter space, but we had to start with a smart initial guess of the model parameters. Our third attempt, with rather rough input parameters, already produced an adequate fit to the data. We show this model SED in the left panel of Fig.

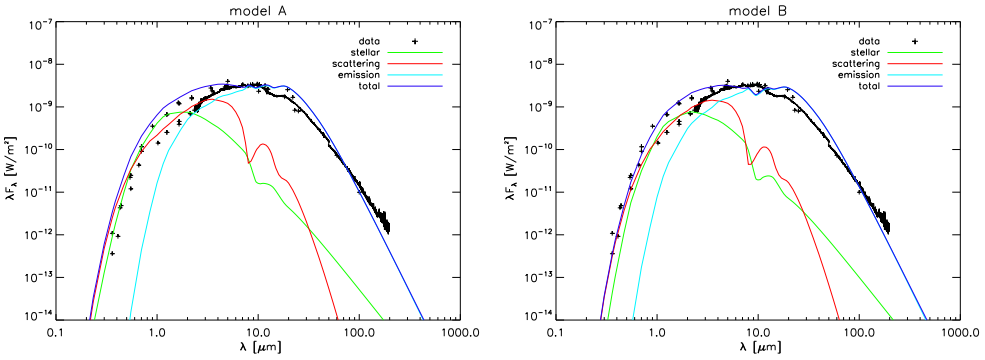

Figure 4.5: Our 2 best LELUYA model fits to the SED of VY CMa. The data references are given in Table 4.1. The different contributions to the total flux (dark blue) are shown: a stellar component (green), dust scattered light (red) and thermal emission (light blue). Table 4.2 summarizes the input parameters used for both models.

Table 4.2: Input parameters for LELUYA. The corresponding model SEDs are shown in Fig. 4.5.

Parameter	Model A	Model B
$T_{\rm eff}$	3500 K	2800 K
$T_{\rm subl}$	1500 K	1500 K
$R_{\rm out}$	100 $R_{\rm subl}$*	150 $R_{\rm subl}$*
dust	70% carbon + 30% silicates	60% carbon + 40% silicates
ρ_0	1.0	1.0
p	2	2
h_0	10.0	10.0
m	1.5	1.0

* Because of the scaling approach used in LELUYA, the outer radius is defined in function of the dust sublimation radius $R_{\rm subl}$, which is not a priori known but can be derived at the end of the calculations.

4.5, marked as “model A”. The different contributions (stellar radiation, scattered light and thermal emission) to the total continuum emission are indicated as well. Table 4.2 lists the input parameters of “model A” in the second column. The central black body has a high temperature of 3500 K, dust sublimation starts at a distance from the star where the temperature has dropped to 1500 K. The outer radius of the disk is 100 times this sublimation radius. The dust in the disk consists of 70% of carbon and 30% of silicates. Although the calculated spectrum is an acceptable fit to the observed SED, the parameters mentioned in Table 4.2 are not optimal. The stellar temperature should be reduced to 2800 K, and the silicate dust fraction has to be increased. LELUYA

also reproduces 2-dimensional images. In Fig. 4.6, we show the observed HST, near-IR and mid-IR images of VY CMa, together with the predicted images produced by LELUYA for "model A". In the optical, we already see a good agreement between model and observations, despite the fact that our model emission is less extended than the observed one. The emission is clearly one-sided at the shortest wavelengths, while some more emission shows up in the NE towards longer wavelengths. We can also distinguish the central object in both model and observations. When we look at the results for the IR, however, we are less satisfied. Our model produces images where the emission is too concentrated towards the center. Therefore, we should also increase the outer radius of the model to get better agreement, mainly with the IR images.

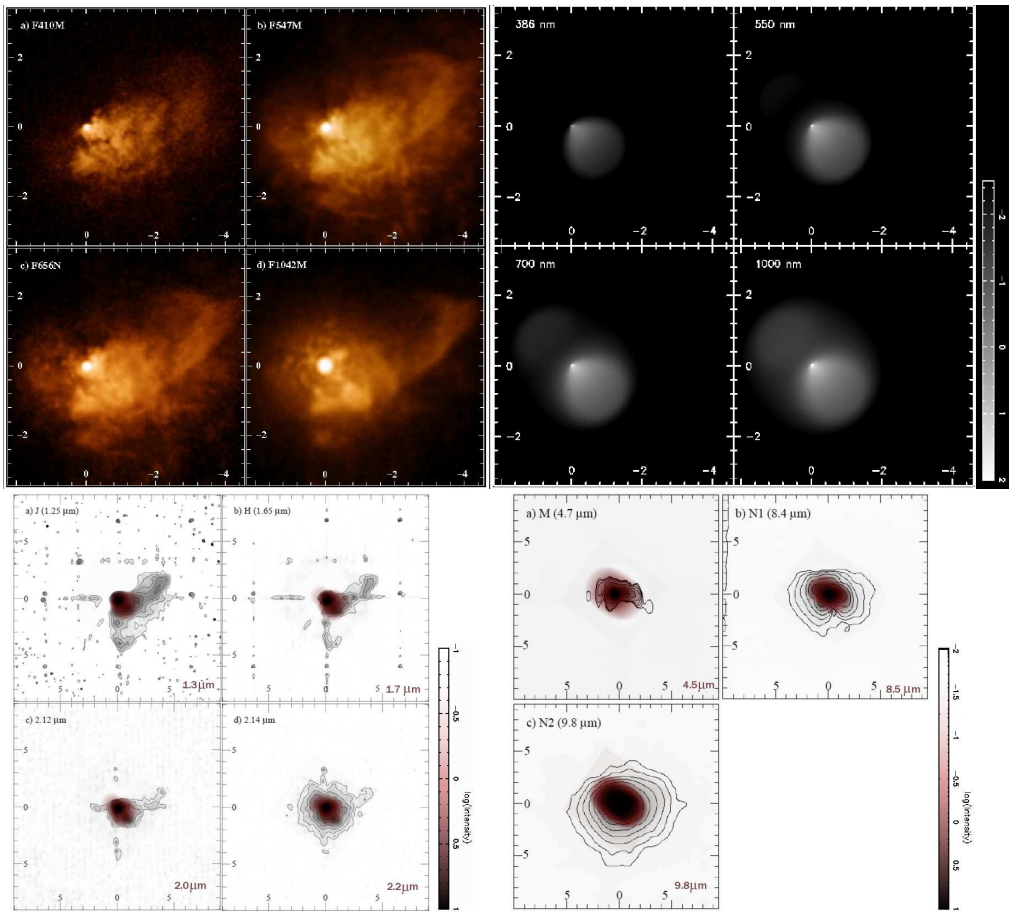

Figure 4.6: Images for "model A" obtained with LELUYA. *Top*: The HST/WFPC2 images of Fig. 3.2 are shown to the left, and the corresponding LELUYA model to the right. *Bottom*: The near-IR images of Fig. 3.3 (*left*) and the mid-IR images of Fig. 3.4 (*right*), with the LELUYA model results overlayed in red.

We tried to improve the input parameters. After a few unsuccessful trials, we identified a new set of suitable parameters. These are marked as "model B" and listed in the third column of Table 4.2. The central black body of "model B" has the more realistic temperature of 2800 K. The dust sublimation temperature is still 1500 K, but the outer radius is increased with respect to the sublimation radius: $R_{\rm out} = 150\ R_{\rm subl}$. The carbon fraction is slightly reduced to 60%, compared to 70% in "model A". The resulting SED is shown in the right panel of Fig. 4.5. Overall, "model B" fits the observed SED as well as "model A", but if we focus on the region around 10 μm, there is a large discrepancy between "model B" and the observations. "Model B" shows the 9.7 μm silicate feature in absorption, which is not observed in the ISO-SWS data. "Model A" follows the SWS data much better in this wavelength range. It should also be noted that, although "model B" has the correct stellar temperature, the percentage of silicates in the dust mixture is still too low for a M-type star. Fig. 4.7 compares the continuum emission at 9.8 μm of Smith et al. (2001) with the LELUYA model image for both "model A" and "model B". The extent of the emission is slightly increased for "model B", but we still don't reach the observed range.

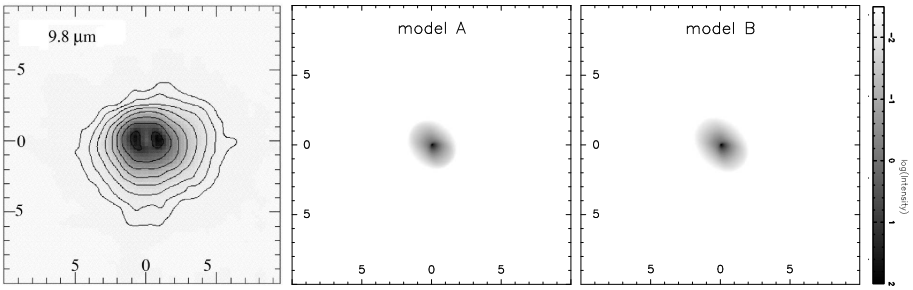

Figure 4.7: *Left*: Observed emission at 9.8 μm (see Fig. 3.4). *Middle*: LELUYA image calculated for "model A" at 9.8 μm. *Right*: LELUYA image calculated for "model B" at 9.8 μm.

Due to the long computational time of LELUYA, it is difficult to develop a smart algorithm to generate the best set of input parameters. Moreover, the influence of each individual parameter is not easy to predict. Therefore, we only ran a limited number of models in our attempt to improve the results. We further increased the outer radius, and used a dust mixture with a higher concentration of silicate grains, but we didn't manage to obtain a good fit to the observed SED. In Fig. 4.8, we show the calculated SED for one of such models. Even though we would have expected a better agreement with these more realistic parameters, the results are worse than those of "model A" and "model B" (Fig. 4.5).

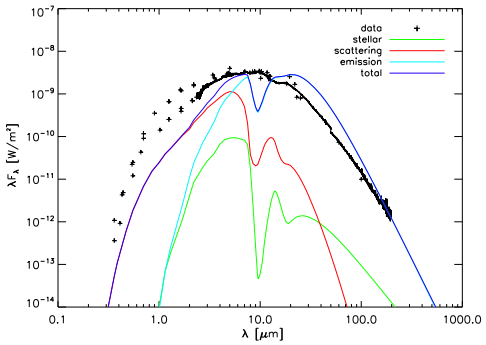

Figure 4.8: Example of an SED calculated with LELUYA with a more "ideal" set of input parameters.

LELUYA is too time consuming to explore the complex geometry of VY CMa's envelope. Nevertheless, it had the advantage of offering 2-dimensional model images, where basic radiative transfer codes often only provide a fit to the spectral energy distribution. We calculated the LELUYA images for a whole range of wavelengths for "model A" and present them in Fig. 4.9. This gives a compact overview of how the observed continuum emission changes as the wavelength increases. The next step is now clear: we need to advance to a new radiative transfer program, that incorporates the imaging capabilities of LELUYA and can handle two-dimensional geometries, but at the same time allows to scan the parameter space (i.e. the computational time should be considerably shorter than for LELUYA) and predict the influence of the different input parameters. In the following section, we present this new method, along with the results for VY CMa.

4.6 MCMax: two-dimensional Monte Carlo radiative transfer modeling

We started using the Monte Carlo radiative transfer code MCMax (Min et al. 2009) to overcome the problem of the long computation time of LELUYA. Instead of the 4 days needed by the latter, we are now able to calculate a model with MCMax in approximately 30 to 60 minutes, thanks to the implemented modified random walk. This allows us to explore the input parameter space, and create a extensive grid of possible models. Moreover, MCMax also produces images at any desired wavelength. The results of our analysis are presented later in this section. First, we explain the specifics of the MCMax transfer code in the next subsection.

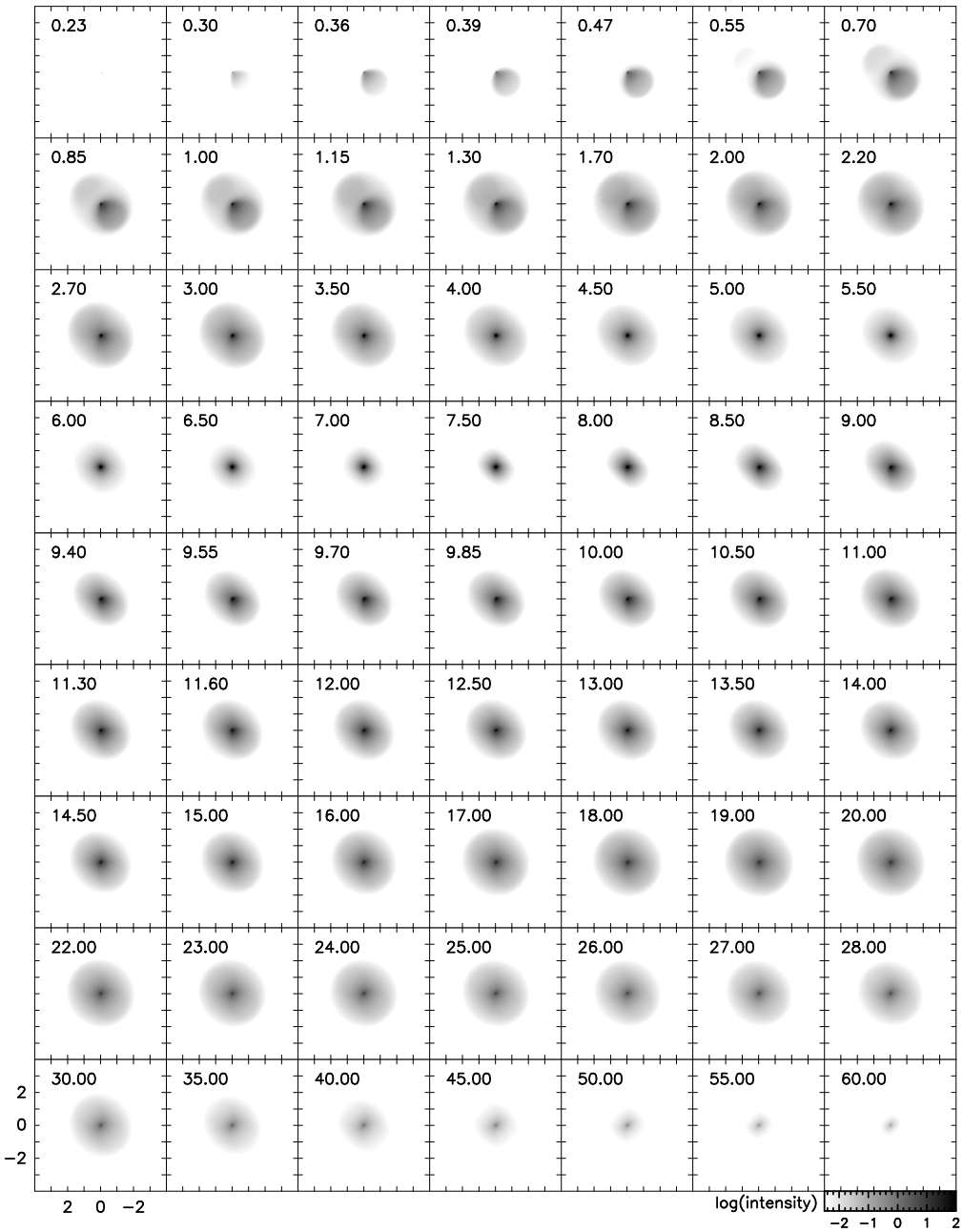

Figure 4.9: Images calculated with LELUYA for "model A". The wavelength, in μm, is indicated in the top left corner of each panel.

4.6.1 Partial diffusion approximation and modified random walk

MCMax is a two-dimensional Monte Carlo radiative transfer code developed by Min et al. (2009) for optically thick circumstellar disks, which can solve the vertical structure of the disk self-consistently. The radiative transfer part is based on the Monte Carlo method described by Bjorkman & Wood (2001), presented in Section 4.4 of this work. In order to determine the vertical structure, an iterative scheme is applied, using the equation for hydrostatic equilibrium

$$\frac{dP(r,z)}{dz} = -\rho(r,z)\frac{GM_*}{r^3}z, \tag{4.28}$$

where r is the distance to the central star, z the height above the midplane of the disk, $\rho(r,z)$ the dust density in the disk, G the gravitational constant, M_* the stellar mass and $P(r,z) = k_{\rm B}\rho T/(\mu m_u)$ the pressure, with $k_{\rm B}$ the Boltzmann constant, $\mu = 2.3$ the mean molecular weight and m_u the proton mass. As discussed in Section 4.4, the Monte Carlo radiative transfer code calculates the temperature structure of the model. The iteration process starts by calculating the Monte Carlo temperatures for an initial guess of the density ρ. With these temperatures, equation (4.28) can be solved. The updated density is then used to repeat the Monte Carlo computations, until convergence is reached.

Clearly, an accurate determination of the vertical structure as described above, requires adequate temperature estimates. However, in the midplane of an optically thick disk, photon counts are usually low since only few photon packages manage to penetrate this shielded region during the Monte Carlo calculations. Thus, the statistical noise on the temperature determination can be rather high in the severely obscured regions. Therefore, MCMax employs a partial diffusion approximation (PDA) to reduce the photon noise in such regions. Because of the very high optical depth, the mean free path of the photons will be much smaller than the length scale over which the density and temperature change. In this case, the energy transport takes place by radiative diffusion, regulated by the diffusion equation (Rosseland 1924):

$$\nabla\cdot(D\nabla E) = \frac{1}{c}\frac{\partial E}{\partial t}, \tag{4.29}$$

where D is the diffusion coefficient (which will be defined later), E the local energy density and c the speed of light. MCMax first calculates the temperature structure by means of the Monte Carlo method. Only after that, the partial diffusion approximation is applied in the regions with low photon counts. The PDA consists of solving $\partial E/\partial t = 0$, the time independent version of the diffusion equation (4.29), which comes down to solving

$$\nabla\cdot\left(D\nabla T^4\right) = 0 \tag{4.30}$$

for the temperature T. The above equation (4.30) only needs to be solved in those regions where photon counts are low. Usually, the limit can be set to less than 30 photon packages per cell. The necessary boundary conditions to solve the set of linear equations resulting from (4.30) are given by the previously calculated Monte Carlo temperatures at the edge of these regions.

Apart from the partial diffusion approximation, MCMax also applies a modified random walk (MRW) approximation. The MRW aims at reducing the computation time. Indeed, when complicated, optically thick geometries are assumed, the duration of the calculations can increase considerably. Our basic one-dimensional Monte Carlo code described in Section 4.4 didn't suffer too much from this problem, but with the two-dimensional disk geometry we want to investigate with MCMax, computing time will definitely rise. In general, computational speed is a crucial point of any radiative transfer program. It was the major drawback of LELUYA (see Section 4.5) which forced us to move on to a more time efficient transfer code.

The modified random walk approximation implemented in MCMax is based on the theory developed by Fleck & Canfield (1984). The computation time is largely determined by a few photon packages that can get lost in highly optically thick regions in the midplane of the disk. Because of the extreme optical depth, any reemission or scattering event will immediately be followed by a new interaction, sending the package back and forth through the dense region. Although only a handful of photons actually enter these shielded regions, the ones that do so might undergo a very large number of interactions before they finally manage to leave the region, thereby tremendously increasing the computing time. The idea behind the MRW procedure is to replace the real, complicated path of these photons by a random walk approximation, which allows to calculate all the interaction events in one computational step. Fleck & Canfield (1984) studied the statistical properties of the photon paths, and found that the random walk corresponds to a solution of the diffusion equation (4.29), namely

$$\psi(\vec{r},t) = \frac{1}{(4\pi Dct)^{3/2}} \exp\left(-\frac{r^2}{4Dct}\right), \tag{4.31}$$

where $\psi(\vec{r},t)$, solution of $D\nabla^2\psi = \frac{1}{c}\frac{\partial E}{\partial t}$, is the energy fraction that has diffused to position $\vec{r}$, with $|\vec{r}| = r$, at time t. However, (4.31) is a solution of the diffusion equation only in the case of a homogeneous, infinite medium. The random walk that MCMax wants to treat takes place within a limited region of the disk. Therefore, Fleck & Canfield (1984) introduced a boundary condition

$$\psi(r = R_0, t) = 0, \tag{4.32}$$

with R_0 the radius of the homogeneous sphere, centered at the starting point of the photon path, within which the random walk has to be enclosed. This boundary condition translates to assuming an absorbing barrier at the edge of the sphere. Taking condition (4.32) into account, solution (4.31) can be rewritten for the modified random walk as

$$\psi(\vec{r},t) = \frac{1}{R_0^2}\sum_{n=1}^{\infty}\left(\frac{n}{r}\right)\exp\left\{-\left(\frac{\pi n}{R_0}\right)^2 Dct\right\}\sin\left(\frac{n\pi r}{R_0}\right). \tag{4.33}$$

The probability that a photon package traveling according to the modified random walk is still inside the sphere of radius R_0 after a time t is given by the integral expression

$$P(t) = 4\pi\int_0^{R_0} r^2\psi(\vec{r},t)\,dr. \tag{4.34}$$

To apply the modified random walk in the Monte Carlo calculations, a random number P_0 is taken between 0 and 1. The time t_{R_0} it takes for the photon package to travel to the edge of the sphere can then be found by solving $P(t_{R_0}) = P_0$. Instead of considering every individual interaction event that the package would undergo in the sphere with radius R_0, as in traditional Monte Carlo routines, the photon's coordinates are advanced to a position on the surface of the sphere, determined from a uniform distribution, and its time is progressed to $t + t_{R_0}$. This will considerably decrease the computation time. In order to keep the energy balance intact, we have to keep track of the energy added to the dust grains in the sphere due to absorption of the photon package during the random walk. This energy is given by

$$E = \varepsilon ct\rho\bar{\kappa}_{\rm abs}, \tag{4.35}$$

where ε is the energy of the photon package (see Section 4.4.1), and $\bar{\kappa}_{\rm abs}$ is the average mass absorption coefficient defined by

$$\bar{\kappa}_{\rm abs} = \frac{\int_0^\infty \frac{\kappa_\nu^{\rm abs}}{\kappa_\nu}\kappa_\nu^{\rm em}\,d\nu}{\int_0^\infty \frac{1}{\kappa_\nu}\kappa_\nu^{\rm em}\,d\nu}, \tag{4.36}$$

where κ_ν is the mass extinction coefficient (as defined in Section 4.4.1), $\kappa_\nu^{\rm abs}$ the mass absorption coefficient and $\kappa_\nu^{\rm em}$ the emission coefficient. The process of determining the MRW statistics, advancing the photon package to its new position on the edge of a homogeneous sphere, and calculating the new energy balance within the sphere is repeated as long as the package is in the specific, very high optical depth region. Once it leaves this region, it will be handled by the normal Monte Carlo scheme. In order to discriminate between a standard Monte Carlo treatment or a modified random walk path for a certain photon package at a certain location in the disk, a criterion has to be

set. Generally, the MRW will be applied if

$$R_0 > \frac{\gamma}{\rho\kappa_R}, \tag{4.37}$$

with $\rho\kappa_R = \alpha_R$, the Rosseland mean extinction coefficient (4.15). Recommended values for γ range between 1 and 10, depending on the desired speed and accuracy.

The diffusion coefficient D to be used in equation (4.29) is calculated in Fleck & Canfield (1984) as

$$D = \frac{\langle d^2 \rangle}{6\langle d \rangle}. \tag{4.38}$$

Min et al. (2009) determined the appropriate expressions for $\langle d \rangle$ and $\langle d^2 \rangle$ to be used in MCMax:

$$\langle d \rangle = \frac{\int_0^\infty \frac{\kappa_\nu^{\rm em}}{\rho\kappa_\nu}\, d\nu}{\int_0^\infty \kappa_\nu^{\rm em}\, d\nu} \quad , \quad \langle d^2 \rangle = 2\frac{\int_0^\infty \frac{\kappa_\nu^{\rm em}}{\rho^2\kappa_\nu^2}\, d\nu}{\int_0^\infty \kappa_\nu^{\rm em}\, d\nu}. \tag{4.39}$$

With the partial diffusion approximation and modified random walk procedure included, MCMax allows for a faster calculation than traditional Monte Carlo codes. Even very optically thick disk models can be treated within a reasonable time thanks to the MRW. The PDA ensures an accurate temperature structure, leading to a self-consistent determination of the vertical structure.

4.6.2 Study of the input parameters

The first step towards modeling the circumstellar envelope of VY CMa with MCMax is a parameter study. By looking at the influence of each of the important input parameters separately, we will be able to narrow the parameter space before constructing a large grid of models. We start by generating a model with standard values for the input. The main ones, which will be under investigation in the parameter study, are listed in Table 4.3. Furthermore, we assume a position angle of -120° and the distance is set to 1.14 kpc (Choi et al. 2008). The dust composition is taken equal to the one used in "model A" of LELUYA (see Table 4.2). Even though we know that the carbon fraction in this mixture is much too high for a M-type star, "model A" proved to be the best-fit LELUYA model. Nevertheless, we will obviously change the dust composition throughout the modeling process with MCMax. The mixture with 70% of carbonaceous grains and 30% of silicates is merely adopted as a starting value, since it is the result our previous modeling effort left us with.

We assume a disk geometry, and the temperature of the central star is represented by a

Table 4.3: Input parameters of the "standard model" of VY CMa used in MCMax.

Parameter	Value
T_*	2800 K
M_*	25 $M_\odot$
Inclination angle	50°
$M_{\rm dust}$	10^{-3} $M_\odot$
$R_{\rm in}$	45 AU
Dust composition	70% carbon + 30% silicates

black body of 2800 K (see Table 4.3). The surface density of the dusty disk is given by

$$\Sigma(r) \propto r^{-p} \exp\left\{-\left(\frac{r}{R_0}\right)^{2-p}\right\}, \tag{4.40}$$

where R_0 is a turnover point at which the surface density starts to decrease exponentially. We set $R_0 = 1000$ AU, so that basically $\Sigma(r) \propto r^{-p}$. For our "standard model" we utilize the common surface density $\Sigma(r) \propto r^{-1}$, i.e. we use $p = 1$. The vertical structure is calculated self-consistently from hydrostatic equilibrium, as described in the previous section (see e.g. equation (4.28)). We use 10^5 photon packages per iteration cycle. The resulting SED and optical and IR images are shown in Fig. 4.10.

Although this "standard model" is not intended to be a representative model, due to for instance the questionable dust composition, we still discuss some general conclusions that can be drawn from the results presented in Fig. 4.10. From the SED, it is clear that our model overestimates the optical and near-IR flux. Around 4 μm, this behavior changes and the flux level of our model becomes too low compared to the observations in the mid-IR. Only at far-IR wavelengths, the model fits the ISO-LWS data. The optical images produced with MCMax follow the trend of the Hubble observations (see Fig. 3.2), with purely one-sided emission in the southwest at the shortest visible wavelengths, and some more emission towards the northeast at longer observing wavelengths. In the infrared, the predicted images are less optimal. The observed emission is more extended than the one reproduced by our model, a problem also encountered with LELUYA. We scaled the infrared images to the units used by Smith et al. (2001) and the contours are drawn at the same levels, to facilitate comparison with Fig. 3.3 and 3.4. We furthermore notice that the emission in the mid-IR is still rather concentrated towards the southeast, whereas the observed emission is more symmetric at these longer wavelengths.

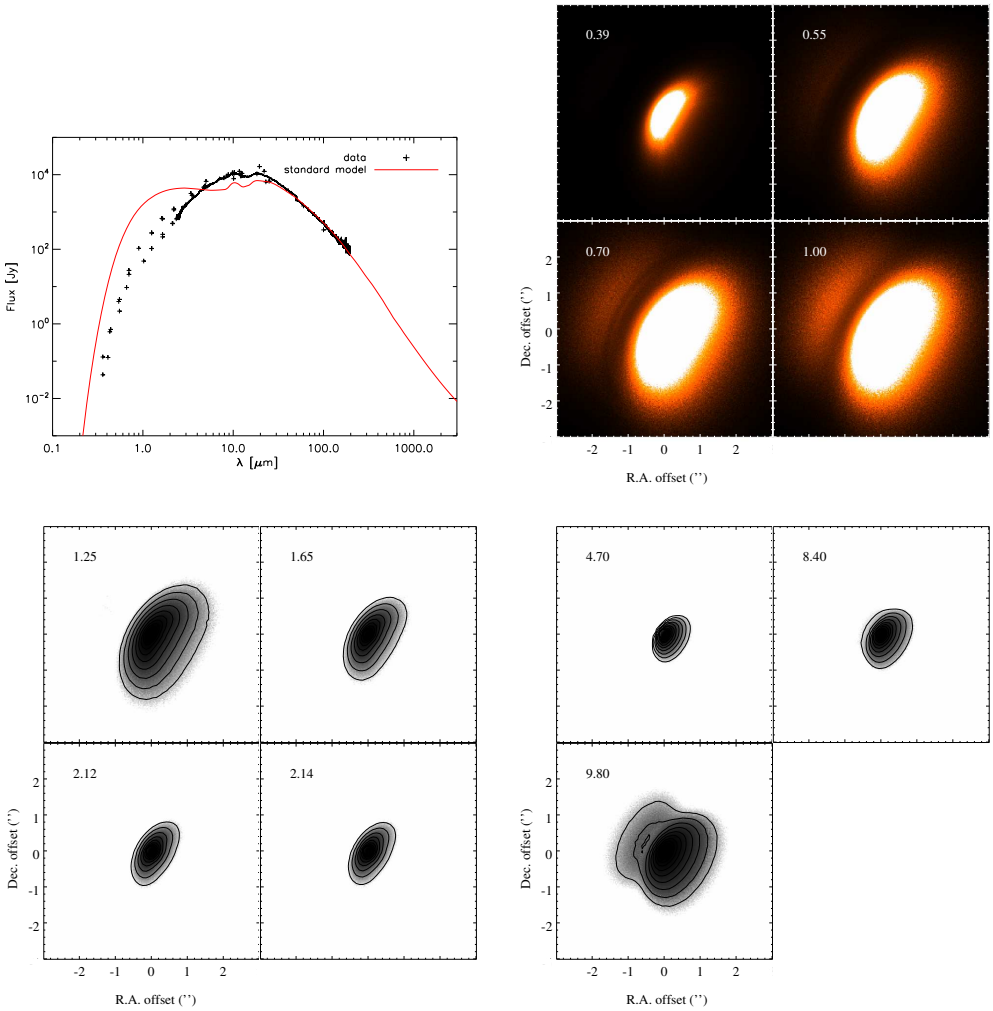

Figure 4.10: Results for the "standard model" obtained with MCMax. *Top left*: Model SED (red) compared to the literature data summarized in Table 4.1 (black). *Top right*: Model optical images at 0.39 μm, 0.55 μm, 0.70 μm and 1 μm, to be compared with the HST observations of Fig. 3.2. The wavelength, in μm, is indicated in the top left corner of each panel. *Bottom left*: Model near-IR images, to be compared with Fig. 3.3. The lowest contour is drawn at 1.2×10^{-17} W cm^{-2} μm^{-1} arcsec^{-2} for the 1.25 μm image and at 2.4×10^{-17} W cm^{-2} μm^{-1} arcsec^{-2} for the 1.65 μm, 2.12 μm and 2.14 μm images, as in Fig. 3.3. Each contour is a factor of 2 above the previous one. *Bottom right*: Model mid-IR images, to be compared with Fig. 3.4. The lowest contour is drawn at 2.2×10^{-17} W cm^{-2} μm^{-1} arcsec^{-2} for the 4.7 μm image, at 2.7×10^{-17} W cm^{-2} μm^{-1} arcsec^{-2} for the 8.4 μm image and at 10^{-17} W cm^{-2} μm^{-1} arcsec^{-2} for the 9.8 μm image, as in Fig. 3.4. Each contour is a factor of 2 above the previous one.

The next step, after the construction of the "standard model", is studying the influence of the different input parameters. Therefore, we vary each of the parameters listed in Table 4.3 independently and look at the changes they cause in the spectral energy distribution. Fig. 4.11 gives an overview of the outcome of this study. In each of the 6 plots, one input parameter is varied while the others are kept constant, and the results for 3 different values of the parameter under investigation are shown. As for the "standard model", an immediate conclusion we can draw from Fig. 4.11 is that almost all our models overestimate the optical and near-IR flux. A detailed discussion of each parameter separately is given next.

- **Stellar temperature T_***
  When the temperature increases, the total flux increases as well, due to the larger contribution of the stellar flux. We could use a low temperature to solve the problem of overestimation in the optical and near-IR (see the model with T = 2000 K). When we look at the longer wavelengths, however, the high temperature model (T = 3000 K) is the one closest to the observations, and low temperatures severely underestimate the flux.

- **Stellar mass M_***
  The influence of the stellar mass is not as important as that of the temperature. From about 70 μm on, all three models give more or less the same result, in agreement with the ISO-LWS data. However, when looking at lower wavelengths, we conclude that the model with the lowest mass (M_* = 15 $M_\odot$) gives the best results. Below 2 μm, this model has the lowest flux, and thus reduces the overestimation at these wavelengths. Above 2 μm, on the other hand, the 15 $M_\odot$ model has the highest flux and therefore fits the mid-IR data much better than more massive models.

- **Inclination angle i**
  If we observe VY CMa under different angles, the SED will change significantly as we are looking through different material. An inclination angle of 90° gives us an edge-on view on the disk, where a big amount of dust is obscuring the central star, hence reducing the flux at the shorter wavelengths (as compared to a small inclination angle, in which case our line-of-sight passes through less dense material). The inclination angle is therefore an important parameter regarding the reduction of the overestimation of the flux in the optical and near-IR. An instructive example of the influence of the inclination angle on the observational results is given in Fig. 4.12, where we compare the theoretical optical and infrared images for two extreme values of the inclination angle. In the top panel, images for a nearly face-on view of the disk (i.e. an inclination angle of 5°) are displayed. The emission is spherically symmetric as expected. The images resulting from an edge-on view of the disk (i.e.

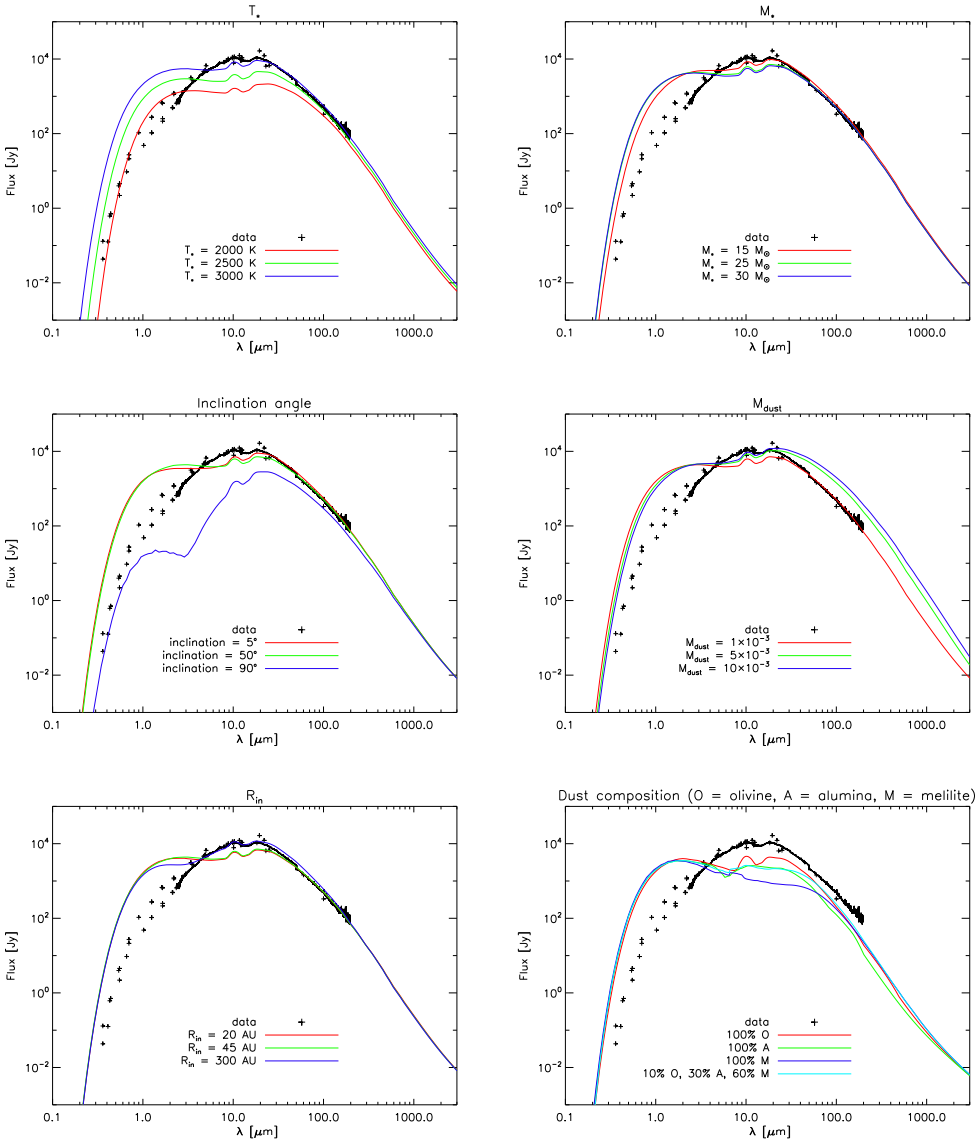

Figure 4.11: MCMax model results for different input parameters. For a discussion, see text.

an inclination angle of 90°) are entirely different. The dusty disk clearly shows its presence as the completely obscured region in the images. The "standard model" represents a case in between these two extremes, with an inclination angle of 50° (see Fig. 4.10).

- **Dust mass M_{dust}**
  Increasing the dust mass mainly influences the flux at higher wavelengths. As the total mass of the dust increases, more dust emission will be observed. The test model with the highest dust mass ($M_{\mathrm{dust}} = 10^{-2}\ M_{\odot}$) compares best to the data at mid-IR wavelengths below 20 μm, but in the far-IR the lowest mass model ($M_{\mathrm{dust}} = 10^{-3}\ M_{\odot}$) fits perfectly to the ISO-LWS data.

- **Disk inner radius R_{in}**
  This parameter represents the radius where the dust formation starts. The biggest difference appears in the mid-IR, where models with the dust formation radius closer to the central star underestimate the flux, while the model with the largest dust-free cavity ($R_{\mathrm{in}} = 300$ AU) provides a close fit to the data.

- **Dust composition**
  For our standard model, we used a very simple mixture of carbon and silicates, derived from the best-fit model obtained with LELUYA. A look at the results of Verhoelst et al. (2009), who studied the typical dust composition in red supergiants, shows that more complicated dust mixtures should be considered when dealing with such objects (see Section 3.5.2 in Chapter 3). Based on Table 3.5, we decided to work with a mixture of olivine, melilite and alumina. The last plot of Fig. 4.11 shows the SEDs for the 3 extreme cases with only 1 dust component, and for a mixture of 10% olivine, 30% alumina and 60% melilite (as a rough average obtained from Table 3.5). The dust composition shows its main importance around 10-40 μm. Once we find the best model fit to the general shape of the SED, we can fine-tune the dust composition to optimize the result in this important wavelength range.

We shortly come back on the overestimation of the flux at the shorter wavelengths by our models. The discussion of the different parameters shows that the stellar temperature and the inclination angle are the parameters with most influence on the optical and near-IR spectral appearance. Indeed, from the results obtained with LELUYA, we can see that in this wavelength range the stellar radiation dominates (see the green line in Fig. 4.5), thus by decreasing the temperature of the central black body, we might be able to reduce the flux in the optical and near-IR. If we choose to work with a low temperature (e.g. $T = 2000$ K), however, we clearly underestimate the flux at wavelengths beyond 3 μm. Moreover, the literature states a temperature value of 2800 K. It thus seems that the main difficulty will be to reduce the flux level in the optical and near-IR.

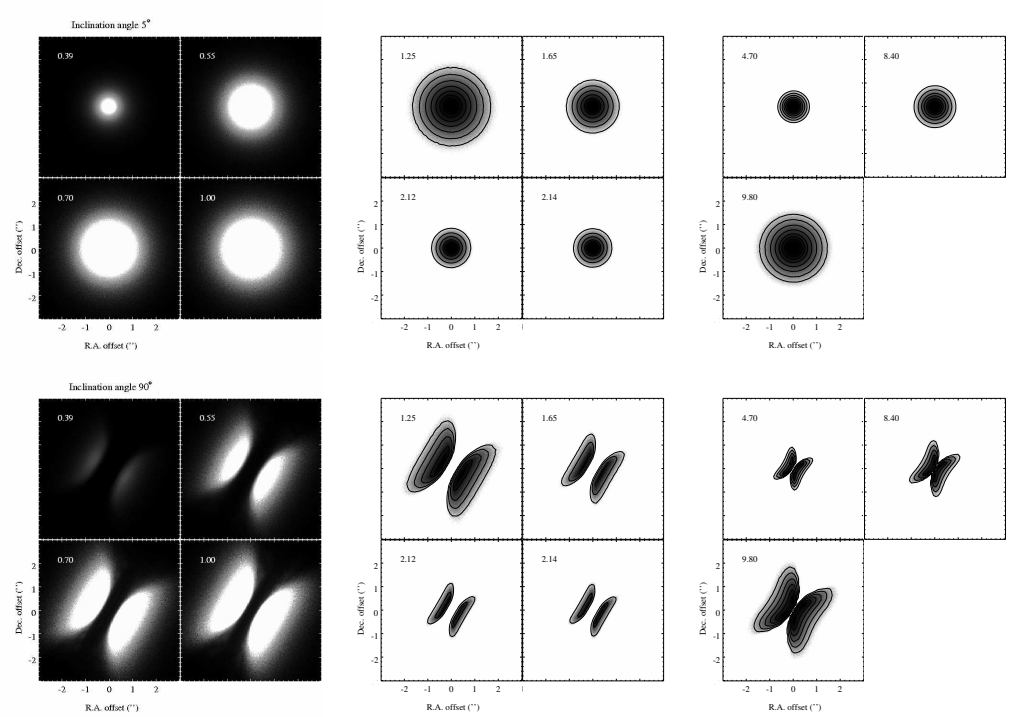

Figure 4.12: Theoretical optical and IR images calculated with MCMax, for a face-on view of the disk (*top*) and an edge-on view (*bottom*).

4.6.3 Constructing a grid of models

After exploring the parameter space, we are ready to construct a meaningful grid of models. We selected the most important input parameters and let them vary between two to five different values, which resulted in more than 2000 models. We used a dust mixture consisting of 10% olivine, 30% alumina and 60% melilite, based on the results of Verhoelst et al. (2009) as explained in the previous section. The setup of our first grid is shown in Table 4.4.

We calculated χ^2 to determine the best-fit model. To compare our model SEDs with the photometric data points, we convolved the models with the corresponding filter bands, as described in Robitaille et al. (2007). We performed the analysis in both the (λ, F_ν) and $(\lambda, \lambda F_\lambda)$ space. In Fig. 4.13, we show the SEDs for the five best models when comparing F_ν (*left*) and λF_λ (*right*). Table 4.5 lists the parameters of these models.

Clearly, even our best model highly overestimates the optical and near-IR flux (red line in Fig. 4.13). Therefore, it is hard to draw any conclusions from Table 4.5, because the

Table 4.4: Overview of the input parameters used in the first grid.

GRID 1

Parameter	Value	
T_*	2500 - 2800 - 3000	[K]
R_*	2000 - 3000 - 4000	[$R_\odot$]
M_*	15 - 25 - 35	[$M_\odot$]
Inclination angle i	5 - 50 - 60 - 75 - 90	[°]
$M_{\rm dust}$	10^{-2} - 10^{-3}	[$M_\odot$]
$R_{\rm in}$	20 - 45 - 100 - 300	[AU]
Surface density*	r^{-1} - r^{-2}	

* For the surface density of the disk (Σ), we assume a power law $\Sigma \propto r^{-p}$, where r is the distance to the star (see equation (4.40)).

parameters listed there don't result in accurate fits. We can merely say that the models with $M_* = 15\ M_\odot$ and $R_{\rm in} = 100$ AU are "favored" (but not acceptable). Already in the parameter study presented before, we realized that a lower stellar mass and a larger disk inner radius result in the best models. We also note that models with $M_{\rm dust} = 10^{-3}\ M_\odot$ fit the data better in a F_ν plot, while $M_{\rm dust} = 10^{-2}\ M_\odot$ gives better results when considering λF_λ. In an attempt to minimize the overestimation of the flux, we neglected the longer wavelengths and only looked at models that fit well in the optical and near-IR range. The result is displayed in Fig. 4.14. While this model follows the observed SED much better in the optical and near-IR, the longer wavelengths now become problematic.

In the first grid, MCMax represents the central star by a black body at a given temperature (see T_* in Table 4.4). Alternatively, we can use a MARCS model atmosphere (Gustafsson et al. 2008). Since the first grid didn't yield an accurate model fit, we chose to construct a second grid, this time employing a MARCS model with a temperature of 3000 K. The other parameters are kept as in grid 1. The setup of this second grid, consisting of around 500 models, is shown in Table 4.6.

Again, we calculated the best-fit models by means of a χ^2 computation. The five best models are plotted in Fig. 4.15 and their input parameters are summarized in Table 4.7. We immediately conclude that the flux level is still too high in the short wavelength range. The best-fit λF_λ model (the green line in Fig. 4.15) minimizes this problem, but it overestimates the far-IR flux, while the other models follow the ISO data well. Unfortunately, MARCS models with a temperature below 3000 K are not yet available, so we couldn't calculate a model with a lower temperature (e.g. 2800 K), which would

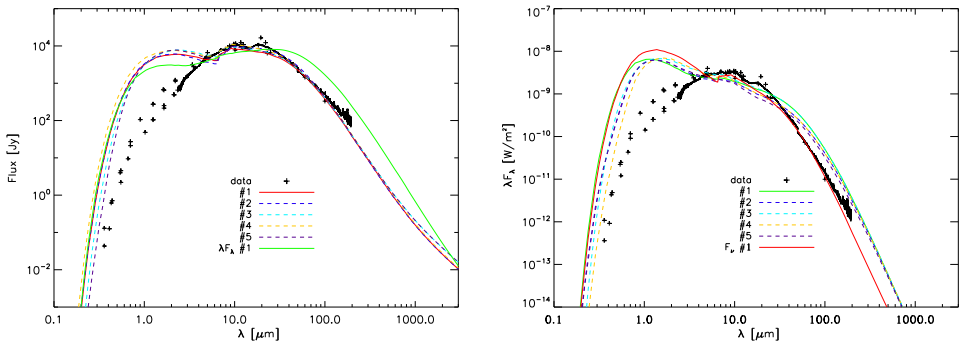

Figure 4.13: SEDs of the five best MCMax models of grid 1, when looking at F_ν (*left*) or λF_λ (*right*). The best model for the other option (i.e. for λF_λ in the F_ν-plot and for F_ν in the λF_λ-plot) is also shown. For clarity, the red line in both plots corresponds to the best-fit F_ν model, and the green line to the best-fit λF_λ model. See Table 4.5 for the details of the models.

Table 4.5: Results for grid 1. The 5 best MCMax models for F_ν (*top*) and λF_λ (*bottom*) are listed. The corresponding SEDs are shown in Fig. 4.13.

	#	T_* [K]	R_* [$R_\odot$]	M_* [$M_\odot$]	i [°]	$M_{\rm dust}$ [$M_\odot$]	$R_{\rm in}$ [AU]	p ($\Sigma \propto r^{-p}$)
	1	2800	3000	15	5	10^{-3}	100	2
	2	2800	3000	15	5	10^{-3}	100	1
F_ν	3	2500	4000	15	5	10^{-3}	100	2
	4	3000	3000	15	5	10^{-3}	100	2
	5	2500	4000	15	50	10^{-3}	100	1
	1	3000	2000	15	5	10^{-2}	100	1
	2	3000	2000	15	50	10^{-2}	100	1
λF_λ	3	2500	3000	15	5	10^{-2}	100	1
	4	2500	3000	15	50	10^{-2}	100	1
	5	3000	2000	15	50	10^{-2}	100	2

probably reduce the flux level in the optical and near-IR.

In an application of MCMax to the transitional disk LkCa15, Mulders et al. (2010) explore the option of dust settling implemented in the MCMax code. In order to obtain the most accurate model, they need to define different settling parameters for each dust component. Although a study among T Tauri stars by D'Alessio et al. (2006) showed that dust settling will mainly reduce flux overestimations in the far-IR, we still decided to investigate the influence on our model SEDs. Therefore, we constructed another grid of models, where we varied the dust settling parameter of each of the three components

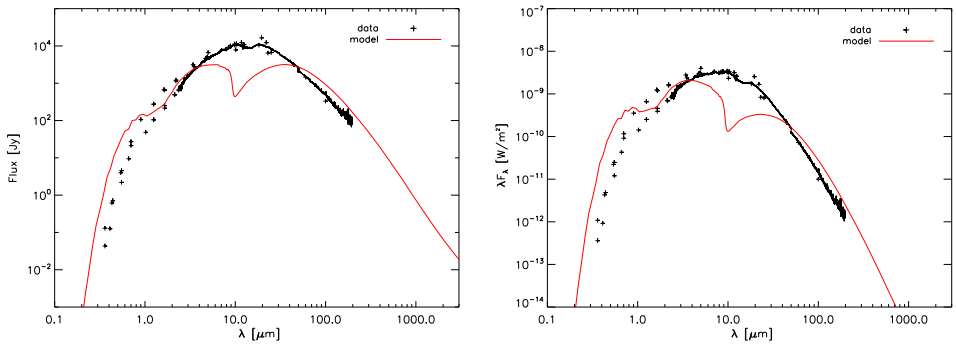

Figure 4.14: SED of the best-fit model of grid 1, when only considering the optical and near-IR wavelengths.

Table 4.6: Overview of the input parameters used in the second grid.

GRID 2		
Parameter	Value	
L_*	3×10^5 - 5×10^5	$[L_\odot]$
M_*	15 - 25 - 35	$[M_\odot]$
Inclination angle	5 - 50 - 60 - 75 - 90	[°]
$M_{\rm dust}$	10^{-2} - 10^{-3}	$[M_\odot]$
$R_{\rm in}$	20 - 45 - 100 - 300	[AU]
Surface density*	r^{-1} - r^{-2}	

* For the surface density of the disk (Σ), we assume a power law $\Sigma \propto r^{-p}$, where r is the distance to the star (see equation (4.40)).

of our dust mixture (i.e. olivine, alumina and melilite) independently. Unfortunately, as expected there was no improvement in the model. The optical and near-IR flux remained unaltered when changing the dust settling parameters, only the mid-IR flux level was reduced.

4.6.4 Final modeling results

Until now, we based the dust composition on the results of Verhoelst et al. (2009) for a large sample of RSGs. We used an average composition derived from Table 3.5, consisting of olivines, alumina and melilite. VY CMa, however, was not included in this study. Clearly, the standard RSG dust composition doesn't apply to VY CMa, as all our models highly overestimate the optical and near-IR flux. It thus seems necessary to consider a more dedicated dust mixture. In Chapter 3, we discussed the modeling

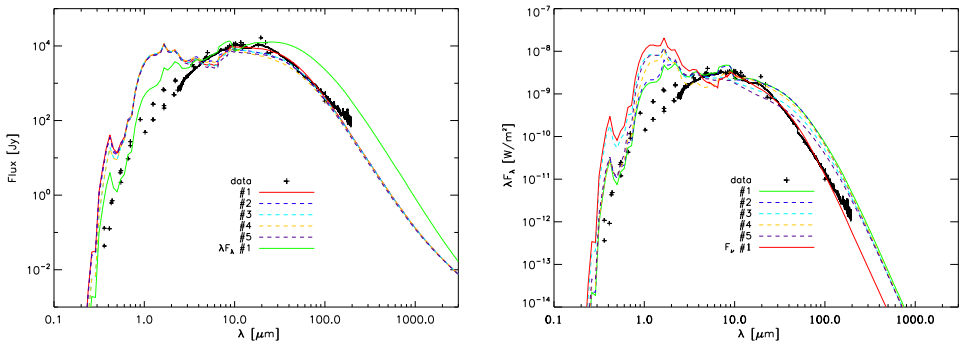

Figure 4.15: SEDs of the five best MCMax models of grid 2, when looking at F_ν (*left*) or λF_λ (*right*). The best model for the other option (i.e. for λF_λ in the F_ν-plot and for F_ν in the λF_λ-plot) is also shown. For clarity, the red line in both plots corresponds to the best-fit F_ν model, and the green line to the best-fit λF_λ model. See Table 4.7 for the details of the models.

Table 4.7: Results for grid 2. The 5 best MCMax models for F_ν (*top*) and λF_λ (*bottom*) are listed. The corresponding SEDs are shown in Fig. 4.15.

	#	L_* [$L_\odot$]	M_* [$M_\odot$]	i [°]	$M_{\rm dust}$ [$M_\odot$]	$R_{\rm in}$ [AU]	p ($\Sigma \propto r^{-p}$)
	1	5×10^5	15	5	10^{-3}	100	1
	2	5×10^5	15	5	10^{-3}	100	2
F_ν	3	5×10^5	15	50	10^{-3}	100	1
	4	5×10^5	15	50	10^{-3}	100	2
	5	5×10^5	25	5	10^{-3}	100	1
	1	5×10^5	15	60	10^{-2}	300	1
	2	5×10^5	15	60	10^{-2}	300	2
λF_λ	3	3×10^5	15	5	10^{-2}	100	1
	4	3×10^5	15	50	10^{-2}	300	1
	5	3×10^5	15	50	10^{-2}	100	1

effort of VY CMa by Harwit et al. (2001). Although they used a spherically symmetric setup, their proposed dust composition could provide better results than the standard RSG composition. Section 3.5.1 summarizes the results of Harwit et al. (2001). Unlike Verhoelst et al. (2009), they find that metallic iron is the main dust component. For their sample of RSGs, Verhoelst et al. (2009) conclude that only a small fraction of typically 1% or less (with a maximum of 5%) of metallic iron is needed. Note that in Table 3.5 metallic iron is not listed, but the authors mention that it can be substituted for carbon. Harwit et al. (2001), on the other hand, add 55% of metallic iron to their dust mixture. While silicates are poor absorbers at short wavelengths, iron absorbs radiation

much more efficiently in this wavelength domain. Therefore, including metallic iron could provide the necessary opacity at short wavelengths to reduce the overestimation of the flux.

We constructed a final grid of models. Since a temperature of 2800 K is stated in the literature, and MARCS models below 3000 K are not available, we assumed a central black body at 2800 K. The stellar mass is set to 15 $M_\odot$, as this proved to be the best value in our previous models. We varied the stellar radius between 1700 $R_\odot$, 2000 $R_\odot$ and 3000 $R_\odot$. The inner radius of the dusty disk was taken to be 100 AU, 200 AU and 300 AU, and the total dust mass 10^{-3} $M_\odot$ and slightly higher 2×10^{-3} $M_\odot$. Finally, we studied inclination angles of 45°, 50° and 55°, based on the parameter study we performed earlier. Four components were included in the dust mixture: metallic iron, olivine, alumina and melilite. We tried different fractions of each component, until the best agreement with the observed SED was found.

The input parameters of the best-fit model are listed in Table 4.8. The model consists of a central black body with a temperature of 2800 K. The stellar radius and mass are 2000 $R_\odot$ and 15 $M_\odot$, respectively. The inner radius of the dusty disk, which has a total dust mass of 10^{-3} $M_\odot$, is 200 AU. The surface density of the disk follows a power law $\Sigma \propto r^{-1}$, according to equation (4.40). The dust in the disk consists of a mixture of 10% olivine, 30% alumina, 10% melilite and 50% metallic iron. The disk is observed under an inclination angle of 55°. The resulting SED is shown in Fig. 4.16. The flux is still slightly too high in the optical and near-IR, but compared to Fig. 4.13 and 4.15 the improvement is enormous. Obviously, the inclusion of metallic iron was absolutely necessary in order to reduce the flux level at short wavelengths. A drawback is the small increase of far-IR flux. More radiation is absorbed by metallic iron at the shorter wavelengths, and consequently a larger amount is reemitted again. Reducing the dust mass lowers the flux in the far-IR, but at the same time results in a larger excess in the optical and near-IR. Therefore, we decided to settle for an intermediate solution, where both the shortest and longest wavelengths are slightly overestimated, but the average excess is minimized.

Once the best-fit model was obtained, we tested the influence of very small variations of each of the input parameters, as to find the most optimal set of parameters. None of these variations caused significant effects on the calculated SED, thus we decided to keep the input listed in Table 4.8 as the final result. The images calculated from the best-fit model are shown in Fig. 4.17. Towards longer IR wavelengths, our model still doesn't reproduce the more symmetrical emission observed in Fig. 3.4, but the optical images compare well to the observed HST images of Fig. 3.2, with asymmetrical one-

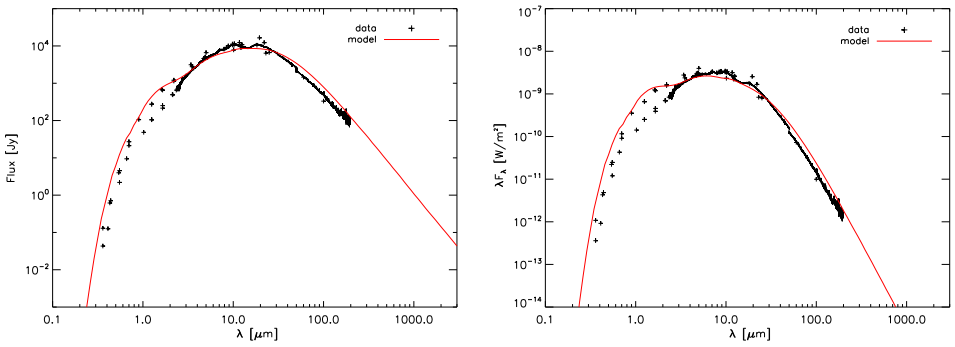

Figure 4.16: SED of the best-fit model calculated with MCMax. Table 4.8 summarizes the input parameters.

Table 4.8: Input parameters for the best-fit model calculated with MCMax. The corresponding model SED is shown in Fig. 4.16.

Parameter	Value
T_*	2800 K
R_*	2000 $R_\odot$
M_*	15 $M_\odot$
Inclination angle i	55°
$M_{\rm dust}$	10^{-3} $M_\odot$
$R_{\rm in}$	200 AU
Surface density[a]	r^{-1}
Dust composition[b]	10% O + 30% A + 10% M + 50% Fe

[a] For the surface density of the disk (Σ), we assume a power law $\Sigma \propto r^{-p}$, where r is the distance to the star (see equation (4.40)).
[b] O = olivine, A = alumina, M = melilite, Fe = metallic iron.

sided emission to the southwest.

4.7 Conclusions

The spectral energy distribution of the RSG VY CMa is characterized by a large infrared excess, caused by the dusty circumstellar envelope. Observations at optical and infrared wavelengths showed the asymmetrical continuum emission, providing evidence for the existence of a dusty disk around VY CMa. In this chapter, we constructed a model of VY CMa's circumstellar environment, and we studied three different radiative transfer methods to try and reproduce the observed SED and optical and IR images.

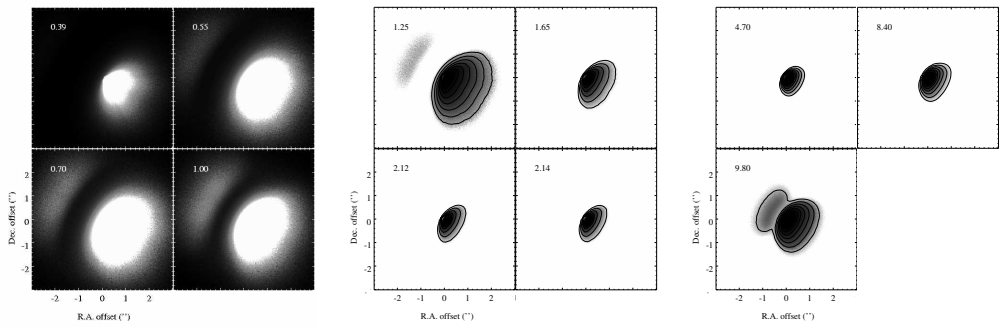

Figure 4.17: Theoretical optical and IR images calculated with MCMax for the best-fit model summarized in Table 4.8. *Left*: Model optical images at 0.39 μm, 0.55 μm, 0.70 μm and 1 μm, to be compared with the HST observations of Fig. 3.2. The wavelength, in μm, is indicated in the top left corner of each panel. *Center*: Model near-IR images, to be compared with Fig. 3.3. The lowest contour is drawn at 1.2×10^{-17} W cm^{-2} μm^{-1} arcsec^{-2} for the 1.25 μm image and at 2.4×10^{-17} W cm^{-2} μm^{-1} arcsec^{-2} for the 1.65 μm, 2.12 μm and 2.14 μm images, as in Fig. 3.3. Each contour is a factor of 2 above the previous one. *Right*: Model mid-IR images, to be compared with Fig. 3.4. The lowest contour is drawn at 2.2×10^{-17} W cm^{-2} μm^{-1} arcsec^{-2} for the 4.7 μm image, at 2.7×10^{-17} W cm^{-2} μm^{-1} arcsec^{-2} for the 8.4 μm image and at 10^{-17} W cm^{-2} μm^{-1} arcsec^{-2} for the 9.8 μm image, as in Fig. 3.4. Each contour is a factor of 2 above the previous one.

Since previous modeling attempts were often based on a spherically symmetric envelope, we used this simple geometry as the input for our first radiative transfer program. Through a Monte Carlo calculation, the spectral energy distribution was calculated. Because of the assumption of spherical symmetry, we could not obtain an optimal fit. The best-fit model underestimated the flux in the optical and far-IR wavelength range.

Next, we considered a more realistic 2-dimensional geometry, where VY CMa is surrounded by a disk. Radiative transfer was solved with the program LELUYA, which rewrites the transfer problem as a matrix equation. Moreover, the program uses a scaling approach, which allows to work with dimensionless quantities. The main drawback of LELUYA is its long computational time. One model calculation takes up to 4 days. Therefore, we could only compute a small number of models, and we were not able to refine the input parameters as to obtain the optimal fit. The best-fit model was found to have a temperature of 3500 K and the dust mixture in the disk consists of 70% of carbonaceous grains and 30% of silicates. These parameters are questionable, as VY CMa is expected to have a stellar temperature of only 2800 K, and the carbon fraction is not supposed to be this large for a M-type star. However, when testing a model with more realistic input parameters, the resulting SED didn't fit to the observations.

In the last section, we introduced a third radiative transfer program, MCMax, which is also based on the Monte Carlo technique. MCMax is developed to solve the vertical structure of the dusty disk in a self-consistent way. Furthermore, as opposed to LELUYA, a model calculation only takes about 30-60 minutes, which enabled us to scan the parameter space and calculate a large amount of possible models. We used both a black body and a MARCS model atmosphere to represent the central energy source. Unfortunately, MARCS models are only available from 3000 K on. A study of the input parameters showed that models with a high stellar temperature systematically overestimate the flux at optical and near-IR wavelengths. Therefore, we could not investigate models with a MARCS atmosphere at the desired temperature of 2800 K, and we decided to focus on a black body of 2800 K in the final calculations.

Metallic iron proved to be an essential dust component in VY CMa's disk. Models without the inclusion of iron reached too high flux levels in the optical and near-IR since silicates, unlike metallic iron, are poor absorbers at these wavelengths. The best-fit model is that of a disk with surface density $\Sigma \propto r^{-1}$ starting at a radius of 200 AU, containing 10^{-3} $M_\odot$ of dust. The dust is a mixture of 50% metallic iron, 30% alumina, 10% olivine and 10% melilite. The central star is a black body of 2800 K with a stellar radius of 2000 $R_\odot$ and a mass of 15 $M_\odot$. The disk is observed under an inclination angle of 55°.

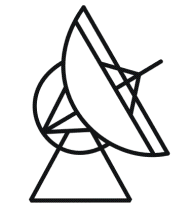

Max-Planck-Institut
für Radioastronomie

5

Molecular line interferometry of VY Canis Majoris: Probing different regions of its envelope

5.1 Introduction

Early in the history of molecular radio astronomy, very strong maser emission in the 1612 MHz satellite hyperfine structure line of OH was found toward the extremely luminous peculiar red M3/M4II supergiant VY CMa, pinpointing it as a remarkable object. Apart from strong maser emission from the OH, H_2O, and SiO molecules thermal emission has been detected toward VY CMa from CO and a number of other species, namely SiO, SO, and SO_2 (Omont et al. 1993). The flux densities of such emissions are moderate and, consequently, their antenna temperatures in single-dish beams are relatively low, mostly less than a Kelvin even for optically thick CO emission. However, this is solely due to the distance, D, to this object (D $\approx$ 1.1 kpc, see Table 3.1). If VY CMa were at 140 pc like the brightest stellar molecular line source IRC+10216, its CO emission would outshine the latters!

VY CMa, with its extreme luminosity $L > 10^5\ L_\odot$, is characterized by a very high mass-loss rate, $\sim 2 \times 10^{-4}\ M_\odot\ \mathrm{yr}^{-1}$ (Bowers et al. 1983), and is close to exploding as

a supernova. Many supernova remnants (SNRs) are distinctly asymmetric and while a clumpy interstellar medium may be responsible for this in some cases, in others, such as Keplers SNR, the reason may be an asymmetric circumstellar shell. As discussed in Chapter 3, recent optical/near-IR HST imaging reveals complex structure around VY CMa, whose morphology is difficult to interpret, since a combination of real density enhancements and reflected light is observed (Smith et al. 2001). However, the latter authors state that "thermal-infrared images reveal a more symmetric distribution, elongated along a nearly east-west direction. VY CMa probably has a flattened disk-like distribution of dust with a northeast-southwest polar axis". Recent multi-mid-infrared wavelength imaging reveals that "spherically symmetric models failed to fit recent VY CMa data, implying that emission from the inner dust shell is highly asymmetric and/or time variable" (Monnier et al. 2000).

From the above we see that there are good reasons for imaging VY CMa's molecular shell. In fact, little is known about the small-scale spatial extent of thermal emission from most molecules around VY CMa. An early measurement with the Plateau de Bure Interferometer (PdBI) yielded a 1.3 arcsec = 1500 AU upper limit to the radius of the 86 GHz $v = 0$, $J = 2 - 1$ SiO emission region, assuming a distance of 1100 pc (Lucas et al. 1992).

Recently, Muller et al. (2007) used the SMA to image the CO $J = 2 - 1$ and a SO line at $\sim 2''$ resolution. They find emission regions of size $\sim 5''$ which is comparable to the extent of the mid-IR dust structure described above. Channel maps reveal 3 emission peaks, a blueshifted one (-5 km s^{-1}) to the east, a peak centered on the stellar position at the systemic velocity of VY CMa (22 km s^{-1}), and a redshifted peak (45 km s^{-1}) to the west of the star. Muller et al. assign two components to their observed CO distribution: a slowly expanding (15 km s^{-1}), spherically symmetric shell, plus a high-velocity bipolar outflow (45 km s^{-1}) with a wide opening angle of 120°, oriented in the east-west direction.

Also recently, Ziurys et al. (2007) reported the detection of emission from a number of molecular species toward VY CMa, including NaCl and PN, both of which had before only been seen in the exceedingly prolific (carbon-rich) circumstellar envelope of IRC+10216. Most remarkably, they detected HCO^+ emission, which had been predicted to be detectable toward O-rich CSEs (Nercessian et al. 1989), but had only been found toward one such object, the protoplanetary nebula OH231.8+4.2 (Morris et al. 1987). Inspection of their spectra learns that different molecules trace different regions of the envelope: a spherical outflow, with a blueshifted and a redshifted expansion. Certain molecules (e.g. SiO) are only present in the spherical wind. Others, like SO_2, show

the typical double-peaked profile of the blue- and redshifted flows. A last group, with SiS and CO, is found in all three components of the envelope. Ziurys et al. (2009) consider a model consisting of a spherically symmetric envelope and a blue- and redshifted outflow. Both flows have an opening angle of 45°, but they have different expansion velocities and inclination angles with respect to the line-of-sight (resp. 38 km s^{-1} and 20° for the blue jet, and 42 km s^{-1} and 45° for the red). They also assign different chemical properties to each flow. The spherically symmetric radiative transfer code of Bieging & Tafalla (1993), adapted for the conical geometry of VY CMa's envelope, is used to calculate abundances, relative to H_2 (with the H_2 column density derived from the star's mass-loss rate), for 6 carbon-bearing molecules (CO, HCN, HNC, CS, HCO^+, CN). Different abundances are obtained for the spherical, red and blue flow.

Ziurys et al. (2007) separate the emission into contributions from a red- and a blue-shifted and a spherically symmetric part purely based on the spectral appearance. Since they have no information about the spatial distribution of the emission from the various components, their abundance estimates are arbitrarily uncertain. Therefore, we have used the PdB interferometer to image the emission regions of several molecules observed by Ziurys et al. (2007, 2009). For the first time, such a wide variety of molecules will be mapped around VY CMa. The observations are discussed in Sect. 5.3 and analyzed in Sect. 5.4. We construct a model of the envelope of VY CMa and determine molecular abundances in Sect. 5.6. Finally, Sect. 5.7 summarizes our results. Before we describe the scientific part, we give a short introduction to radio interferometry in Sect. 5.2.

5.2 Introduction to radio interferometry

In this section, we give an overview of the general principles of radio interferometry. We wish to provide the reader with the necessary background to interpret the observations described and analyzed in the rest of this chapter. Therefore, we only concentrate on the essentials, without going into theoretical or technical details. This section is largely based on the proceedings of two summer schools: "*Synthesis Imaging in Radio Astronomy II*" (Taylor, Carilli, & Perley 1999) and "*IRAM Millimeter Interferometry Summer School 2*" (Dutrey 2000), and the book "*Tools of Radio Astronomy*" (Wilson, Rohlfs, & Hüttemeister 2009).

5.2.1 Basic principles

Diffraction theory shows that the angular resolution of a single antenna is given by

$$\theta = 1.22 \frac{\lambda}{D} \tag{5.1}$$

with θ the angular resolution in radians, λ the observing wavelength and D the diameter of the telescope. Therefore, if we want to improve the angular resolution for a given observing wavelength in order to observe smaller source structure, the diameter D needs to be increased. Technical feasibility places an upper limit on the size of a telescope, and hence restrains the angular resolution. To overcome this problem, one could replace the single large telescope by an interferometer, an array of smaller telescopes covering an equivalent aperture. When combining the light of 2 small antennas, an interference pattern is created, similar to Young's 2 slit experiment. This is called the fringe pattern. The fringe visibility, a complex quantity which can be measured by correlating the output of 2 interferometer antennas, contains all the information about the source intensity distribution. The van Cittert-Zernike theorem states that this complex visibility is the Fourier transform of the intensity distribution on the sky. Thus, by measuring the visibility function in each point of the Fourier space, the source intensity can be derived. In reality, however, only a limited number of visibilities can be obtained, which highly complicates the imaging process. To illustrate this, we start by looking at a two-element interferometer.

Fig. 5.1 shows a simplified version of such a two-element interferometer. The two antennas are separated by the baseline vector $\vec{b}$ and are pointed towards a distant source in the direction of $\vec{s}$. If the source is not at zenith, a wavefront from the source will reach one antenna a time τ_g later than the other, with

$$\tau_g = \vec{b} \cdot \vec{s}/c \tag{5.2}$$

the geometrical delay. The antennas register a signal at radio frequency ν_{RF}. Subsequently, this signal is mixed with a local oscillator at frequency ν_{LO}, creating a new signal at intermediate frequency ν_{IF}, given by $\nu_{\mathrm{RF}} = \nu_{\mathrm{LO}} \pm \nu_{\mathrm{IF}}$. Thus, the mixer is sensitive to two input frequency bands of width $\Delta\nu$ centered around ν_{RF}, the upper side band (USB) and lower side band (LSB), for which

$$\begin{aligned} \mathrm{USB} &: \nu_{\mathrm{IF}} = \nu_{\mathrm{RF}} - \nu_{\mathrm{LO}}, \\ \mathrm{LSB} &: \nu_{\mathrm{IF}} = \nu_{\mathrm{LO}} - \nu_{\mathrm{RF}}. \end{aligned} \tag{5.3}$$

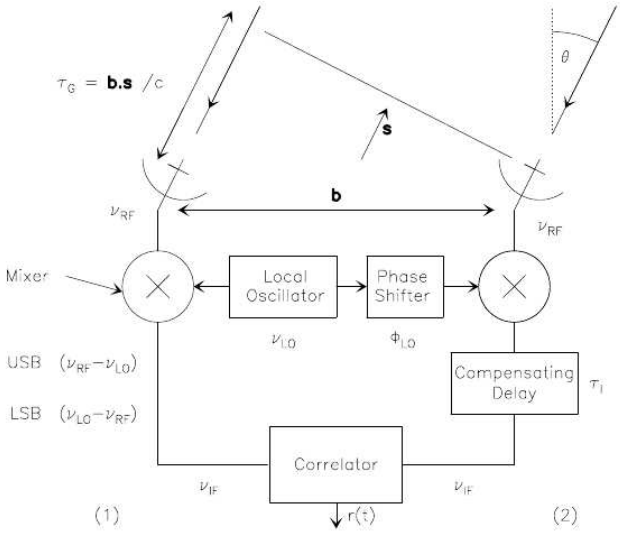

Figure 5.1: Simplified two-element interferometer, with frequency conversion and instrumental delay tracking. The two antennas are separated by baseline vector $\vec{b}$ (Dutrey 2000).

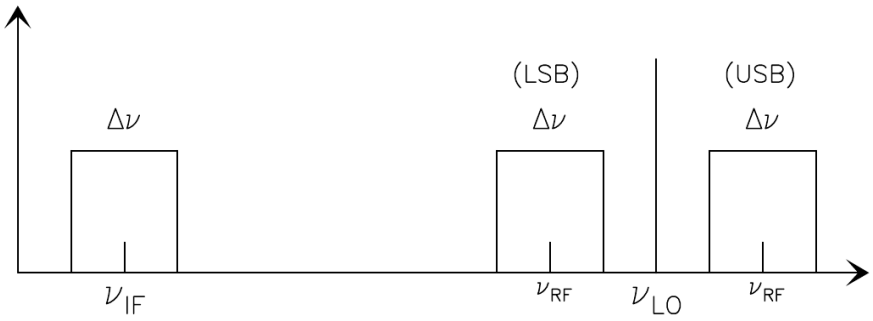

Figure 5.2: Relationship between the radio frequency ν_{RF}, local oscillator frequency ν_{LO} and intermediate frequency ν_{IF} for the lower and upper sideband (Dutrey 2000).

This is illustrated in Fig. 5.2. The aim of the frequency conversion is to facilitate the next steps such as delaying and cross-correlation, which are easier to carry out on signals at a lower frequency ν_{IF}. Before reaching the correlator, where the signals of both antennas will be combined, an instrumental delay τ_i is added to one of the signals, to compensate for the geometrical delay τ_g described in (5.2).

Now consider the correlator, which consists of a voltage multiplier and an integrator. In the following, we want to examine the output of the correlator, in order to understand

the steps involved in creating intensity maps from interferometric observations. Therefore, we will only present a simplified derivation of the correlator output, neglecting receiver noise, gain factors, polarization, frequency conversion, instrumental delay and other complications, and making the necessary assumptions where needed. The input to the correlator are two voltages, induced by a wavefront from the source at the two antennas of the interferometer. These voltages can be written as

$$\begin{aligned} V_1 &= v_1 e^{2\pi i\nu(t-\tau_g)}, \\ V_2 &= v_2 e^{2\pi i\nu t}. \end{aligned} \tag{5.4}$$

The correlator combines the two signals, resulting in the output

$$r(\tau_g) = v_1 v_2 e^{-2\pi i\nu\tau_g}. \tag{5.5}$$

We can describe the observed source in terms of its radio brightness, expressed in W m^{-2} Hz^{-1} sr^{-1}. Let $I_\nu(\vec{s})$ be the radio brightness in the direction of $\vec{s}$ at frequency ν. The power received from a source element $d\Omega$ within the bandwidth $\Delta\nu$ is then $A(\vec{s})I_\nu(\vec{s})\,\Delta\nu\,d\Omega$, with $A(\vec{s})$ the effective collecting area in the direction $\vec{s}$. Combining this with (5.5), the output of the correlator for radiation from a segment $d\Omega$ in direction $\vec{s}$ is

$$dr = A(\vec{s})I_\nu(\vec{s})e^{-2\pi i\nu\tau_g}\Delta\nu\,d\Omega. \tag{5.6}$$

Using (5.2) and writing $\vec{s} = \vec{s}_0 + \vec{\sigma}$, where $\vec{s}_0$ points towards the phase center, we can derive

$$r = \Delta\nu \int_S A(\vec{s})I_\nu(\vec{s})e^{-2\pi i\nu\frac{\vec{b}\cdot\vec{s}}{c}}\,d\Omega \tag{5.7}$$

$$= \Delta\nu e^{-2\pi i\nu\frac{\vec{b}\cdot\vec{s}_0}{c}} \int_S A(\vec{\sigma})I_\nu(\vec{\sigma})e^{-2\pi i\nu\frac{\vec{b}\cdot\vec{\sigma}}{c}}\,d\Omega. \tag{5.8}$$

We now define an important function in interferometry, namely the complex visibility, given by the integral part of (5.8):

$$V_\nu = \int_S A(\vec{\sigma})I_\nu(\vec{\sigma})e^{-2\pi i\nu\frac{\vec{b}\cdot\vec{\sigma}}{c}}\,d\Omega. \tag{5.9}$$

The final output of the interferometer is thus a set of visibilities, which are related to the source brightness as shown in (5.9).

In order to derive the sky brightness distribution from the measured visibilities, we introduce a new coordinate system (u, v, w), such that u points east, v north and w towards the phase center (see Fig. 5.3). The baseline vector $\vec{b}$ can now be expressed in terms of

these coordinates, which are measured in wavelengths. Positions on the sky are represented by l and m, direction cosines with respect to the u and v axes. It can be shown that with these new coordinates, (5.9) can be rewritten as

$$V_\nu(u,v) = \iint A(l,m) I_\nu(l,m) e^{-2\pi i(ul+vm)}\, dl\, dm. \tag{5.10}$$

This can be recognized as a Fourier transform. Performing the inverse Fourier transformation, we get

$$A(l,m) I_\nu(l,m) = \iint V_\nu(u,v) e^{2\pi i(ul+vm)}\, du\, dv. \tag{5.11}$$

Thus, we can calculate the source brightness by Fourier transforming the measured visibility. Unfortunately, it is impossible to obtain a visibility measurement at every point of the uv plane. An interferometer only measures one visibility per baseline, corresponding to one point in the uv plane. Therefore, increasing the number of antennas increases the number of uv points. Moreover, as the Earth's rotation changes the uv components of the baseline vectors, observing over a longer period of time will drastically improve the uv coverage. We represent the coverage of the uv plane by the sampling function $S(u,v)$, which is zero at points without visibility measurement. The Fourier transform of the sampling function is the so-called dirty beam

$$B(l,m) = \iint S(u,v) e^{2\pi i(ul+vm)}\, du\, dv. \tag{5.12}$$

What an interferometer really provides us with is not (5.11), but

$$I_\nu^{\text{dirty}}(l,m) = \iint V_\nu(u,v) S(u,v) e^{2\pi i(ul+vm)}\, du\, dv, \tag{5.13}$$

the dirty image. Combining (5.11), (5.12) and (5.13), and using the convolution theorem for Fourier transforms, we find

$$I_\nu^{\text{dirty}} = (A.I_\nu) * B. \tag{5.14}$$

The outcome of an interferometric observation is a dirty image, which is the true brightness distribution (modified by the primary beam A), convolved with the dirty beam. This is the most important relation to keep in mind when reconstructing interferometric images.

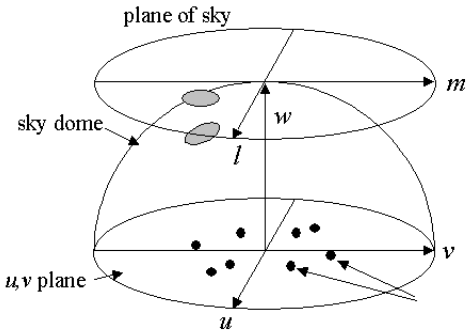

Figure 5.3: Graphical representation of the (u, v, w) coordinate system (`http://web.njit.edu/~gary/728/Lecture6.html`).

5.2.2 Imaging and deconvolution

As described above, an interferometer measures complex visibilities in the *uv* plane. By performing a Fourier transformation of the visibilities, applying the appropriate gridding and weighting scheme, the brightness distribution in the image plane is obtained. However, due to the limited sampling of the *uv* plane, only the dirty image can be derived directly from the measured visibilities. The dirty image contains the sky brightness distribution, convolved with the dirty beam (i.e. the Fourier transform of the sampling function), as shown by the important relation $I_\nu^{\text{dirty}} = I_\nu * B$, calculated above (see (5.14), where we omit A for simplicity). Thus, if we want to create an image of the true brightness distribution, we need to deconvolve the dirty image.

A widespread deconvolution method is the CLEAN algorithm (Högbom 1974). The radio source is assumed to be made up of a finite collection of point sources. The CLEAN algorithm identifies these point sources in an iterative way. First, the strongest peak in the dirty image is determined. This point source, multiplied by a loop gain $0 \leq \gamma \leq 1$, is added to the clean component list. Next, the peak, multiplied by the dirty beam and γ, is subtracted from the dirty image. The process is then repeated, until there is no peak above a certain user-defined limit left in the residual map, or a specified number of peaks has been found. The clean component list contains all the point sources that constitute the radio source. In the final step, this point source model is convolved with a clean beam to form the clean image. The clean beam is usually an elliptical Gaussian fit to the main lobe of the dirty beam. Often, the residual map is added to the clean image, for instance to provide an estimation of the noise. If it is a priori known that the source is confined to a specific region, it might be helpful to define a support around this area, and only search for clean components within the support. Variations on the

method of Högbom (1974) are the Clark and MX Cotton-Schwab algorithms (Clark 1980; Schwab 1984). A popular alternative for the CLEAN algorithm is the Maximum Entropy Method (MEM). The idea is to select the optimal image from a set of possible images, thereby maximizing its entropy. In general, CLEAN is used for point sources and simple, small sources, while MEM is better suited for extended sources.

Visibilities have units of flux density, Jy, whereas the clean intensity map has units of surface brightness, i.e. the flux density per unit of solid angle. Commonly, the clean maps are expressed in Jy/beam. This can easily be converted to brightness temperature T_b using the Rayleigh-Jeans relation

$$T_b = \frac{\lambda^2}{2k\,\Omega_b} S_\nu, \tag{5.15}$$

where λ is the observing wavelength, k the Boltzmann constant, S_ν the surface brightness and $\Omega_b = \frac{\pi\theta_b^2}{4\log 2}$ with θ_b the clean Gaussian beam FWHM.

5.2.3 The Plateau de Bure interferometer

Located in the French Alps at an altitude of 2550 m, is the IRAM (Institut de Radioastronomie Millimétrique) Plateau de Bure interferometer (Fig 5.4). The phase center is positioned at longitude 05:54:28.5 E and latitude 44:38:02.0 N. Originally a three antenna system, the interferometer now consists of six operational 15 m antennas. The antennas are movable along a "*T*" shaped track, with an angle of 75° between the two arms. The north-south arm is 368 m long, the east-west rail has a length of 760 m, which is the maximum separation between 2 antennas. Four predefined antenna configurations exist, listed A through D, A being the most extended and D the most compact. The resulting angular resolution ranges from ∼5" to ∼0.8" at 100 GHz. Combinations of the different configurations are possible to obtain the desired sensitivity, angular resolution and *uv* coverage.

The six antennas are equipped with dual polarization receivers operating at 3 mm, 2 mm and 1.3 mm. The 3 mm band has a frequency range of 80 GHz to 116 GHz, the 2 mm band ranges between 129 GHz and 174 GHz and the 1.3 mm band between 201 GHz and 267 GHz. The frequency bands cannot be observed simultaneously. The mixers are single-sideband. The two IF channels, one for each polarization, are 4 GHz wide. These are split in quarters of 1 GHZ, of which two are selected as input to the narrow-band correlator. The correlator has 8 spectral units, ranging from a narrow bandwidth of 20 MHz with 0.039 MHz channel spacing, to 320 MHz bandwidth with 2.5 MHz spacing. Typical system temperatures are 100 K below 110 GHz, 170/180 K

Figure 5.4: The IRAM Plateau de Bure interferometer in the French Hautes-Alpes, with six 15 m antennas (Image courtesy IRAM).

at 115 GHz, 150/180 K at 150 GHz and 200/250 K at 230 GHz, depending on winter/-summer conditions. The antenna efficiency is 22 Jy K^{-1} at 3 mm, 29 Jy K^{-1} at 2 mm and 35 Jy K^{-1} at 1.3 mm.

5.3 Observations

We observed VY CMa with the IRAM Plateau de Bure Interferometer with the six antennas in the B configuration. The phase center was positioned at $\alpha = 07^{\rm h}22^{\rm m}58^{\rm s}.33$, $\delta = -25^\circ 46' 03''.20$. We used 2 different frequency setups. During the first observing period between January and March 2008 the 3 mm receiver was tuned to 88.95 GHz. Due to bad conditions, we observed the same setup again in January 2009 under excellent weather conditions. In the same period we also observed the second setup at 104.20 GHz. We used continuum bands with 320 MHz bandwidth and 2.5 MHz channel spacing. The 160 MHz line bands with 1.25 MHz channel separation were centered on the different lines of our interest (see Table 5.1). At 88.95 GHz, the primary beam had a FWHM of $\sim 56''$, and at 104.20 GHz the FWHM $\sim 48''$. The absolute flux density scale was determined from observations of MWC349 and 3C454.3. Phase and amplitude calibration were done using 0627-199, 0646-306 and 0823-223.

We used the GILDAS software package[1] to calibrate and analyze the data. Fig. 5.5 shows the *uv* coverage for the two frequency setups, and the corresponding dirty beam obtained by Fourier transformation, according to (5.12). The beams are highly elon-

[1] `http://www.iram.fr/IRAMFR/GILDAS`

Table 5.1: Target lines for the PdB interferometer.

Line	Rest Frequency [GHz]	Synthesized Beam [arcsec]	PA [°]
HCN(1-0)	88.632	3.09×1.32	4
HCO^+(1-0)	89.189	3.08×1.32	5
HNC(1-0)	90.664	3.06×1.29	5
SiS(5-4)	90.772	3.05×1.28	6
NaCl(7-6)	91.170	3.04×1.28	5
$SO_2(3_{1,3}\text{-}2_{0,2})$	104.029	2.72×1.09	9
$SO_2(16_{2,14}\text{-}15_{3,13})$	104.034	2.72×1.09	9
NaCl(8-7)	104.190	2.75×1.09	9
$SO_2(10_{1,9}\text{-}10_{0,10})$	104.239	2.71×1.09	9

gated. The continuum emission, estimated from the line-free parts of the observing bands, was removed from the line observations in the *uv* plane. The continuum maps are presented in Fig. 5.6. The flux densities reach 19 mJy at 88.95 GHz and 27 mJy at 104.20 GHz. We created clean channel maps (512 × 512 pixels of size 0.2") using the CLEAN deconvolution method developed by Högbom (1974), and synthesized beams of ∼ 3.1″ × 1.3″ with PA 5° and ∼ 2.7″ × 1.1″ with PA 9°, at 88.95 GHz and 104.20 GHz respectively. Due to the highly elongated synthesized beams, the emission shows an apparent elongation along the north-south axis (see e.g. the continuum maps in Fig. 5.6). To remove this misleading effect, we repeated the cleaning process, using a symmetrical beam (2″ × 2″) as restoring beam. The result can be found in Fig. 5.7 for the continuum emission.

5.4 Results

5.4.1 Continuum emission

Continuum measurements with the VLA (Very Large Array) at centimeter wavelengths (15 GHz, 22 GHz and 43 GHz) have been presented by Lipscy et al. (2005). They find flux densities of the order of ∼1 mJy. Muller et al. (2007) used the SMA to map the 1.3 mm continuum emission of VY CMa, obtaining a flux density of ∼288 mJy. This is similar to the ∼270 mJy at 215 GHz found by Shinnaga et al. (2004), also with the SMA. JCMT (James Clerk Maxwell Telescope) observations by Knapp et al. (1993) yield flux densities of ∼620 mJy at 1.3 mm and ∼330 mJy at 2 mm. The PdB allowed us to measure the continuum emission around 3 mm. We could fit the continuum visibilities in the *uv* plane by a point source with a flux density of 19 mJy at 88.95 GHz and

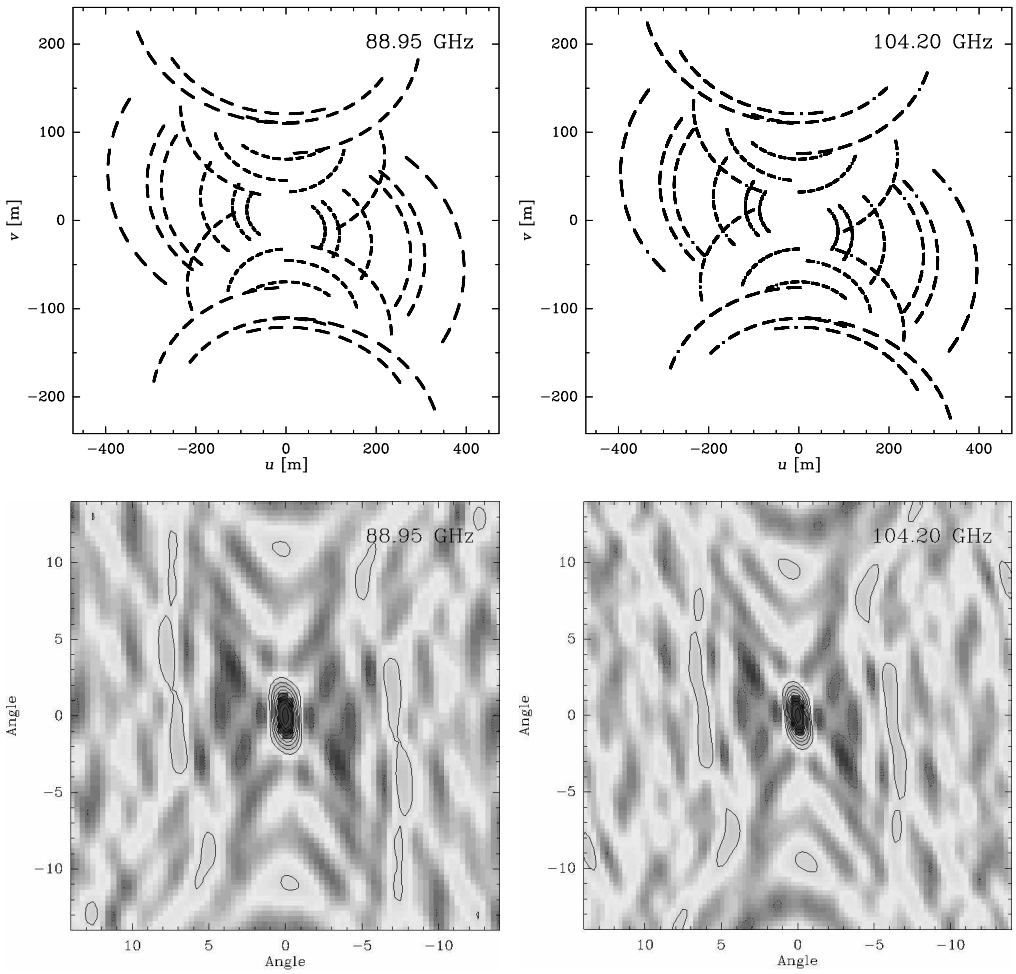

Figure 5.5: *Top*: *uv* coverage of the PdB observations at 88.95 GHz (*left*) and 104.20 GHz (*right*) for an observing time of ∼ 6 hours. *Bottom*: Corresponding dirty beam at 88.95 GHz and 104.20 GHz, respectively.

27 mJy at 104.20 GHz. The cleaned continuum maps for both frequencies are shown in Fig. 5.6 (synthesized beam) and 5.7 (symmetrical beam).

Assuming that the continuum emission is almost exclusively thermal dust emission, we can estimate the total dust mass (Lipscy et al. 2005; Muller et al. 2007). The contribution of the central star, represented by a blackbody of $T = 2800$ K and with $R_* = 1.2 \times 10^{14}$ cm (see Table 3.1), is $S_* \sim 2.7$ mJy at 88.95 GHz and ∼ 3.7 mJy at

104.2 GHz. The total dust mass is given by

$$M_d = \frac{2c^2 D^2 a_g \rho_g (S_\nu - S_*)}{3 Q_\nu k T_d \nu^2}, \tag{5.16}$$

where D represents the distance to the source, a_g the radius of the dust grains, ρ_g the mass density of the dust, Q_ν the grain emissivity, S_ν the continuum flux density and T_d the temperature of the dust envelope. Based on modeling results of Knapp et al. (1993), we use $a_g = 0.2\,\mu$m, $\rho_g = 3.5$ g cm^{-3} and $Q_\nu = 5.65 \times 10^{-4} (\nu/274.6$ GHz). The average dust envelope temperature, derived from the ratio of *IRAS* fluxes, is $T_d \sim 250$ K (Lipscy et al. 2005; Muller et al. 2007). With the flux densities respectively 19 mJy and 27 mJy, we find a total dust mass $M_d = 0.79 \times 10^{-3}\ M_\odot$ for $\nu = 88.95$ GHz and $M_d = 0.71 \times 10^{-3}\ M_\odot$ for $\nu = 104.20$ GHz. Rescaling the results of Lipscy et al. (2005) and Muller et al. (2007), which were calculated for a distance of 1.5 kpc, to the revised value of 1.1 kpc used here, they obtain $M_d = 0.71 \times 10^{-3}\ M_\odot$ (Lipscy et al. 2005) and $M_d = 0.82 \times 10^{-3}\ M_\odot$ (Muller et al. 2007), comparable to our dust mass.

5.4.2 Molecular lines

Channel maps of the observed transitions are presented in Fig. 5.8-5.19. We did not detect any emission from HNC(1-0), but the other lines (see Table 5.1) are clearly present. HCN(1-0) shows, apart from more moderate emission at $v_{\rm sys}$ (~ 22 km s^{-1}), 2 strong peaks, reaching their maximum around -3 km s^{-1} and 45 km s^{-1} (Fig. 5.8-5.9). The blueshifted peak is the strongest (up to ~ 0.55 Jy/beam) and appears close to the phase center, while the weaker redshifted one (~ 0.3 Jy/beam) has an offset of $\sim 1''$ to the west. We observe these 2 peaks at the same velocities and positions in the channel maps of SiS(5-4), though a factor of 10 weaker (Fig. 5.10-5.11). The prominent feature is the strong emission at the systemic velocity of 22 km s^{-1}, seen at the stellar position.

HCO^+(1-0) is mainly detected at a position $4''$ to the west (Fig. 5.12-5.13), where it reaches its maximum around a velocity of 40 km s^{-1}. There is no clear blueshifted component, as seen in HCN(1-0) and SiS(5-4). At the stellar position, emission shows up only around 50 km s^{-1}.

In Fig. 5.14-5.15, the channel maps for NaCl(7-6) and NaCl(8-7) are displayed. Both have only one peak around the systemic velocity (22 km s^{-1}), slightly to the west of the stellar position for NaCl(7-6), and at $\sim 1''$ to the south-west for NaCl(8-7).

Finally, the results for SO_2 are presented in Fig. 5.16-5.17 for a blend of $SO_2(3_{1,3}$-$2_{0,2})$ and $SO_2(16_{2,14}$-$15_{3,13})$ and in Fig. 5.18-5.19 for $SO_2(10_{1,9}$-$10_{0,10})$. Two separate peaks are visible: a strong blueshifted peak around -6 km s^{-1} at an offset of $\sim 1''$ to the north-

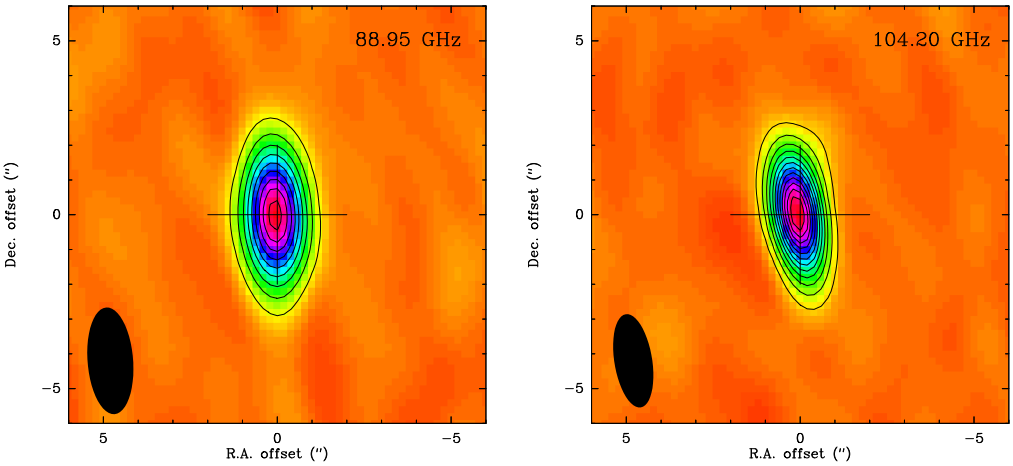

Figure 5.6: Continuum emission map of VY CMa observed with the PdBI at 88.95 GHz (*left*) and 104.20 GHz (*right*). The axes denote right ascension and declination offset from the phase center (indicated by the cross) in arcseconds. Contours are separated by 2 mJy/beam, corresponding to 0.08 K. The synthesized beam (3.08″ × 1.31″ with PA 4° and 2.70″ × 1.08″ with PA 9°, respectively) is shown in the bottom left corner.

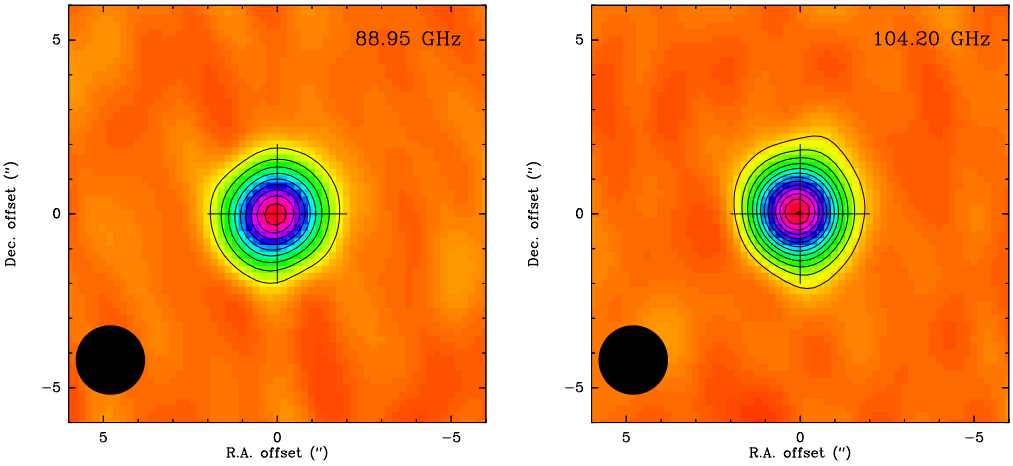

Figure 5.7: Same as Fig. 5.6, but convolved with a 2″ × 2″ symmetrical beam (shown in the bottom left corner). Contours are separated by 2 mJy/beam, corresponding to 0.08 K at 88.95 GHz and to 0.06 K at 104.20 GHz.

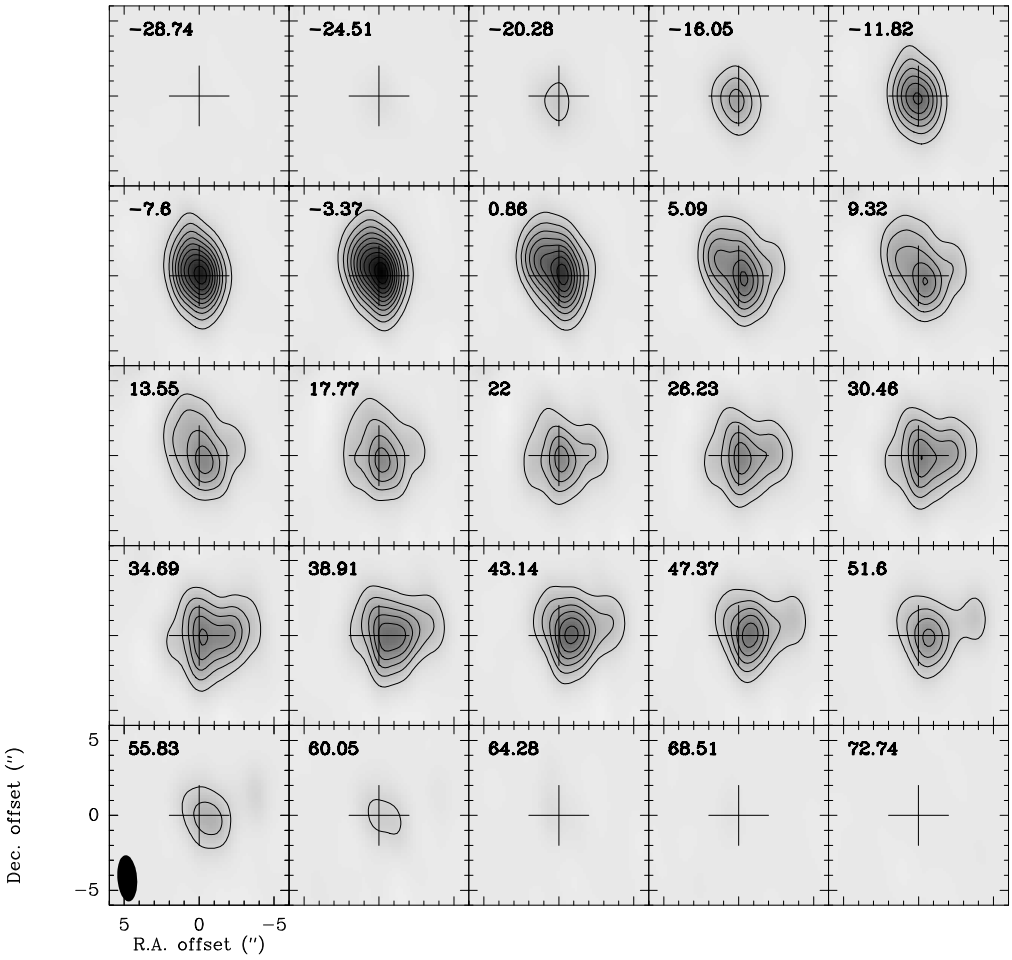

Figure 5.8: Channel maps of HCN(1-0) observed with the PdBI. The axes denote right ascension and declination offset from the phase center (indicated by the cross) in arcseconds. The velocity of each channel (km s^{-1}) is indicated in the top left corner. Contours are separated by 50 mJy/beam, corresponding to 1.92 K. The synthesized beam (3.09″ × 1.32″ with PA 4°) is shown in the bottom left corner.

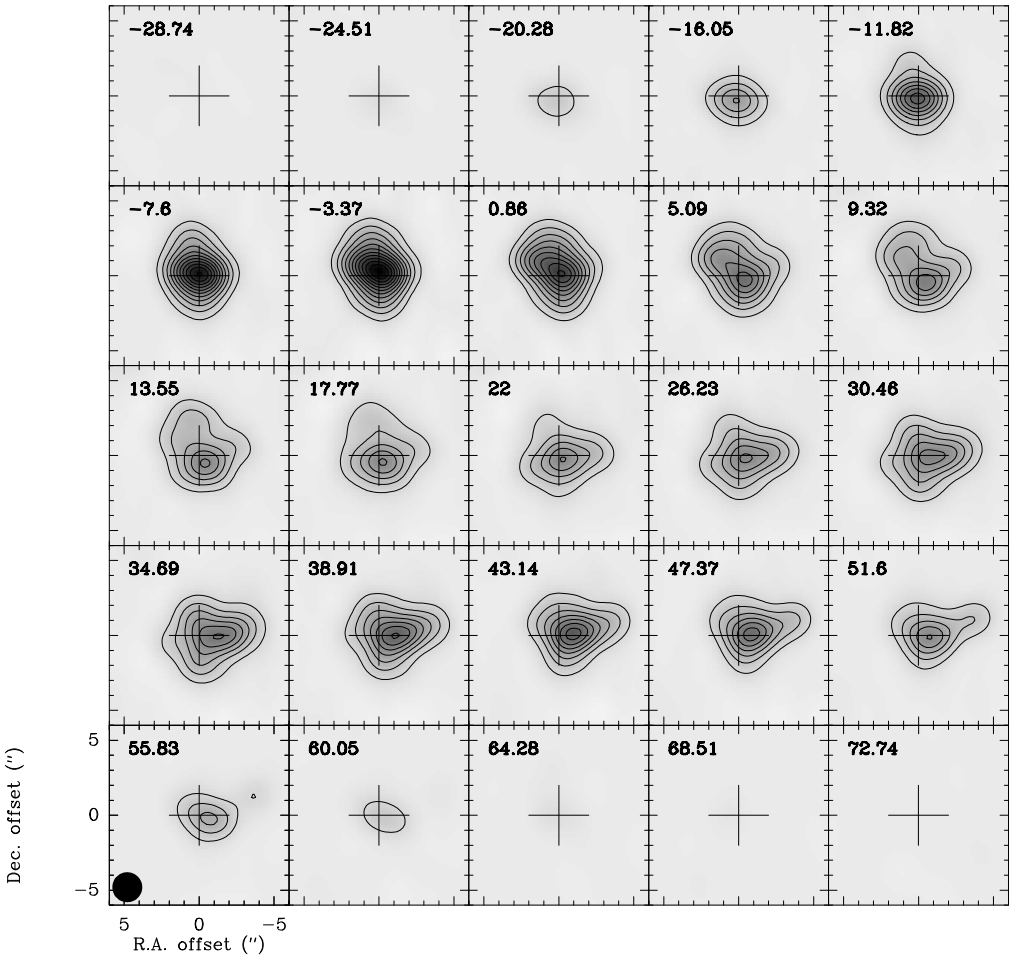

Figure 5.9: Channel maps of HCN(1-0) as in Fig. 5.8, but convolved with a 2″×2″ symmetrical beam (shown in the bottom left corner). Contours are separated by 50 mJy/beam, corresponding to 1.95 K.

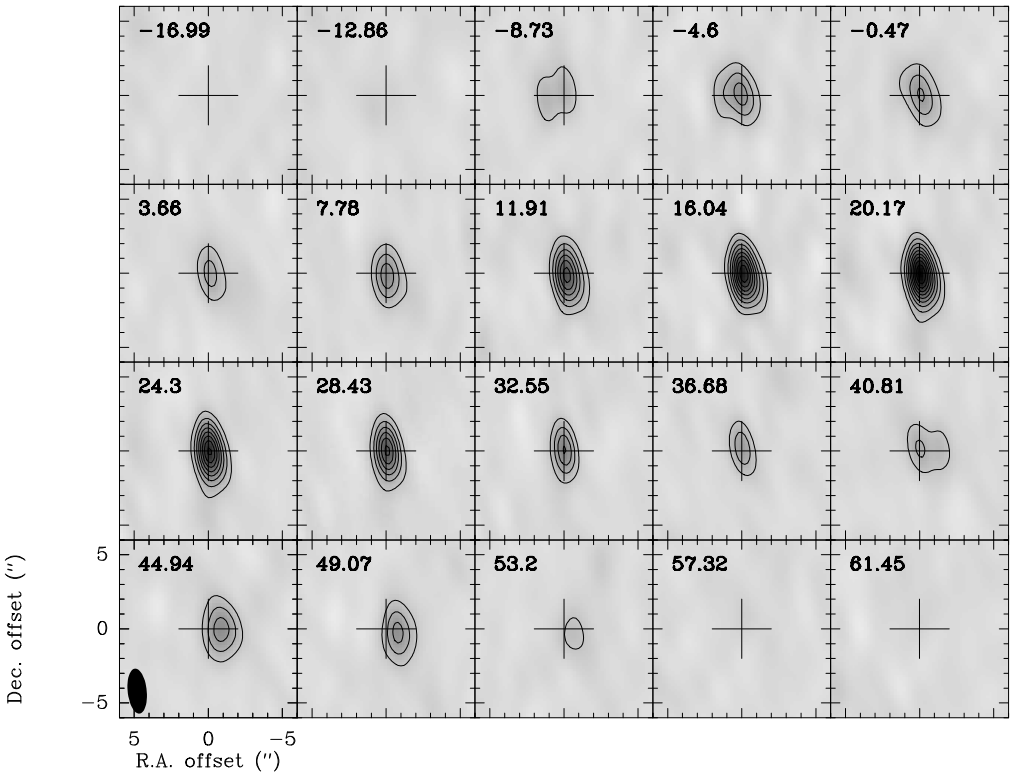

Figure 5.10: Same as Fig. 5.8, but for SiS(5-4). Contours are separated by 10 mJy/beam, corresponding to 0.38 K. The synthesized beam is 3.05″ × 1.28″ with PA 6°.

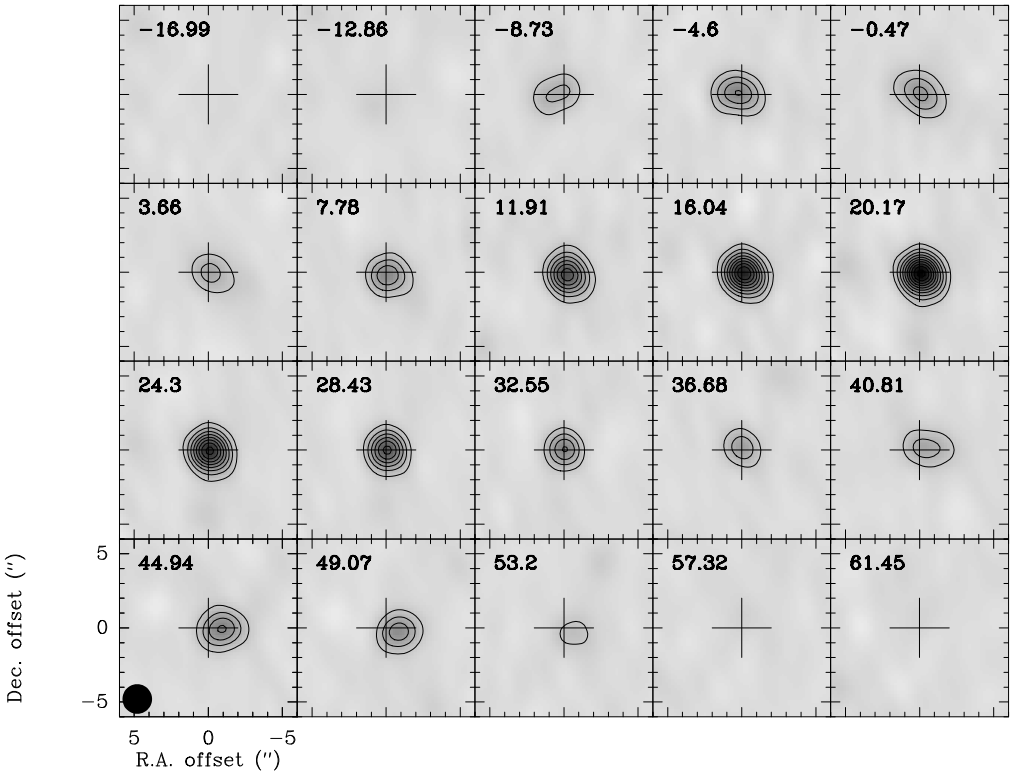

Figure 5.11: Channel maps of SiS(5-4) as in Fig. 5.10, but convolved with a 2″ × 2″ symmetrical beam (shown in the bottom left corner). Contours are separated by 10 mJy/beam, corresponding to 0.37 K.

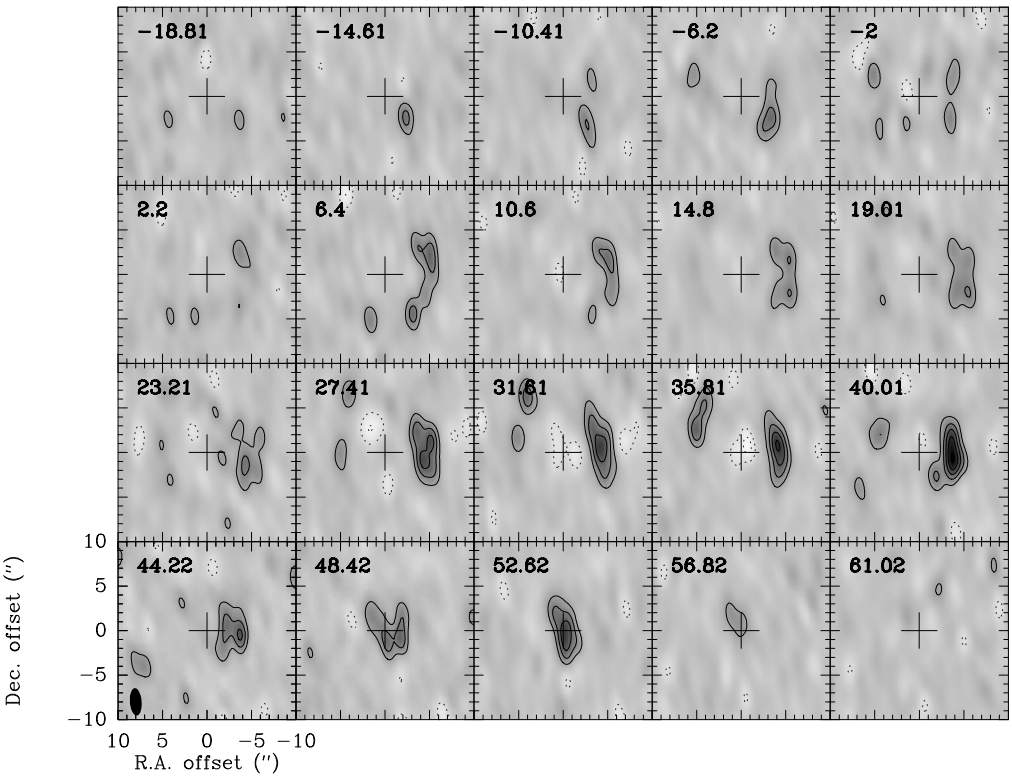

Figure 5.12: Same as Fig. 5.8, but for HCO^+(1-0). Contours are separated by 5 mJy/beam, corresponding to 0.19 K. Dashed lines represent negative levels. The synthesized beam is $3.08'' \times 1.32''$ with PA 5°.

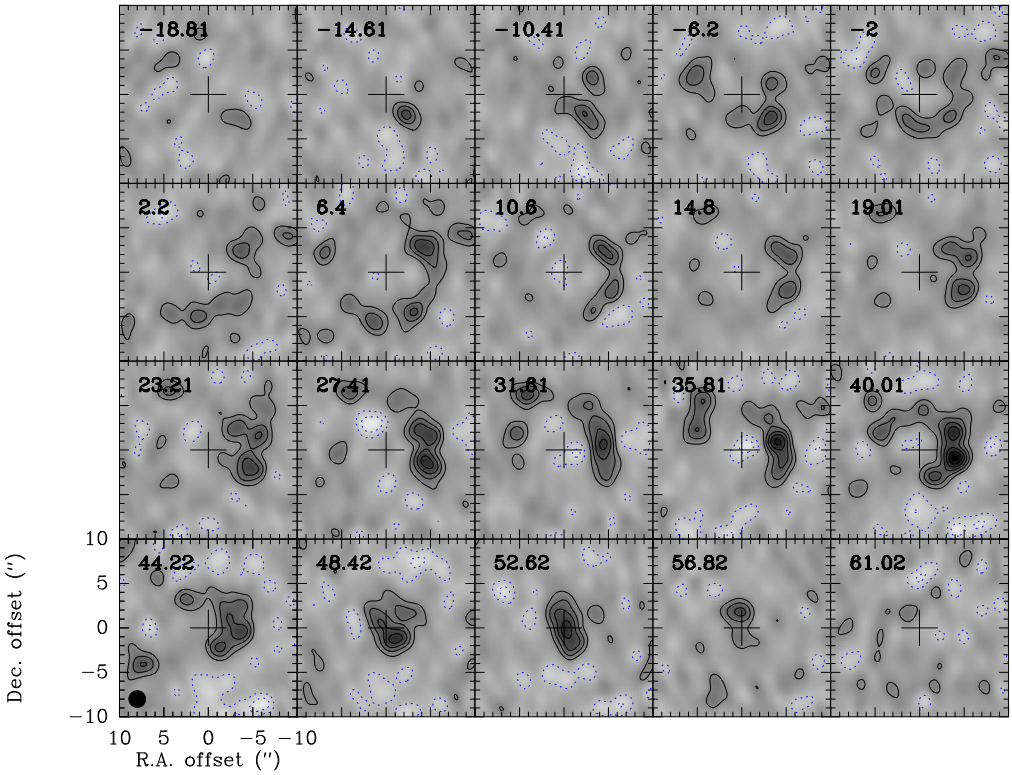

Figure 5.13: Channel maps of HCO^+(1-0) as in Fig. 5.12, but convolved with a 2″ × 2″ symmetrical beam (shown in the bottom left corner). Contours are separated by 5 mJy/beam, corresponding to 0.19 K.

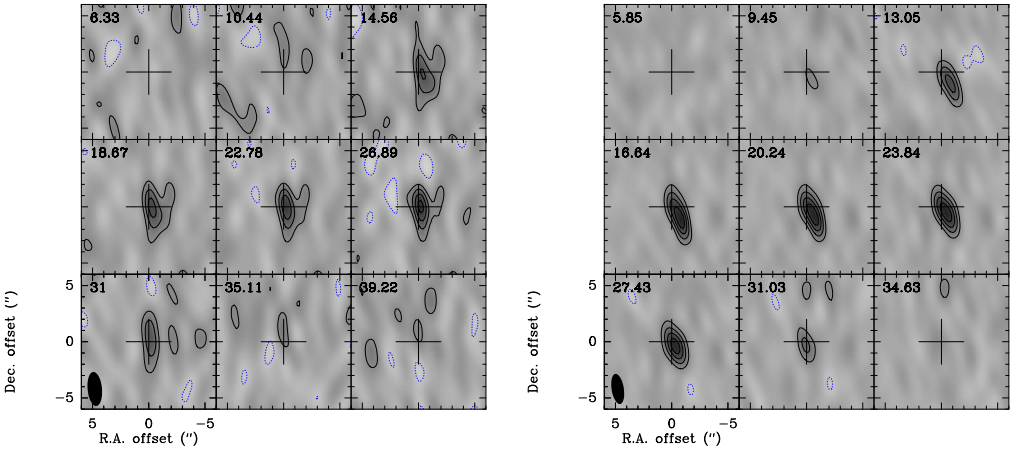

Figure 5.14: Same as Fig. 5.8, but for NaCl(7-6) (*left*) and NaCl(8-7) (*right*). Contours are separated by 5 mJy/beam, corresponding to 0.19 K. Dashed lines represent negative levels. The synthesized beam is $3.04'' \times 1.28''$ with PA 5° and $2.75'' \times 1.09''$ with PA 9°, respectively.

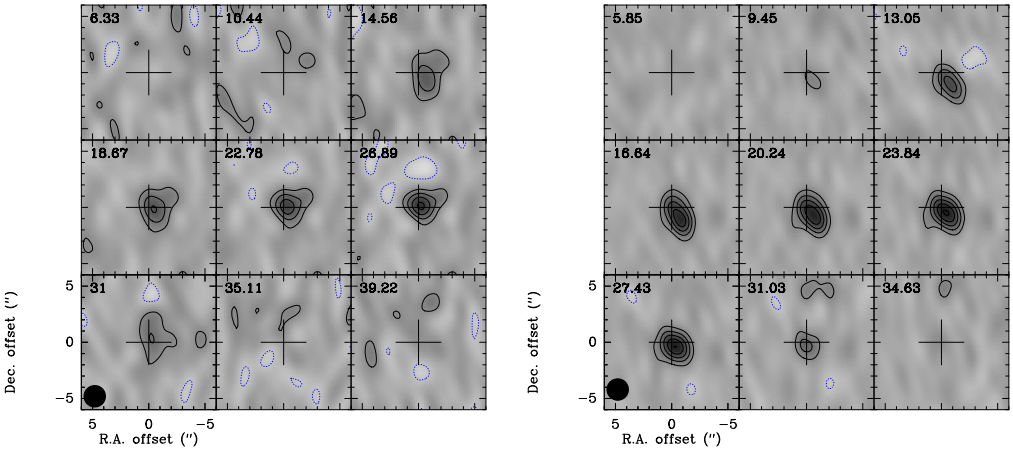

Figure 5.15: Channel maps of NaCl(7-6) (*left*) and NaCl(8-7) (*right*) as in Fig. 5.14, but convolved with a $2'' \times 2''$ symmetrical beam (shown in the bottom left corner). Contours are separated by 5 mJy/beam, corresponding to 0.18 K and 0.14 K respectively.

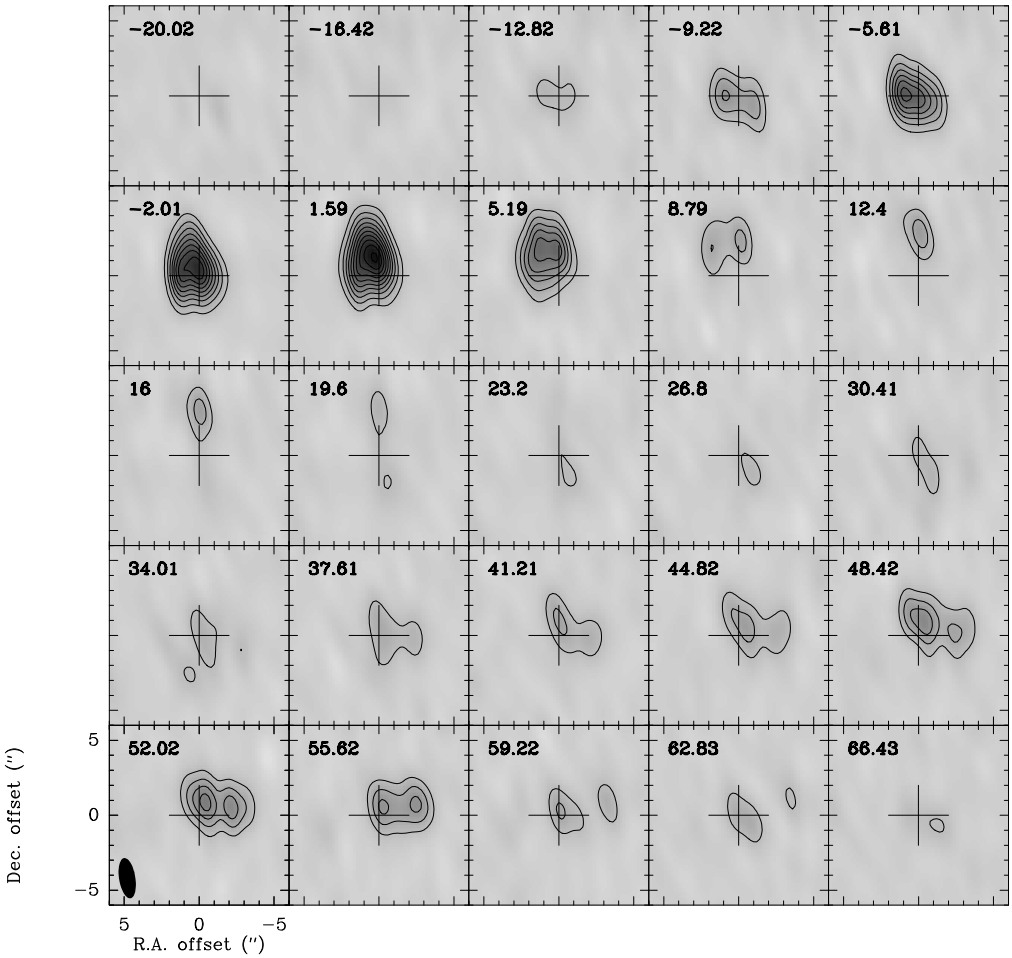

Figure 5.16: Same as Fig. 5.8, but for $SO_2(3_{1,3}\text{-}2_{0,2})$ and $SO_2(16_{2,14}\text{-}15_{3,13})$. Contours are separated by 10 mJy/beam, corresponding to 0.38 K. The synthesized beam is $2.72'' \times 1.09''$ with PA 9°.

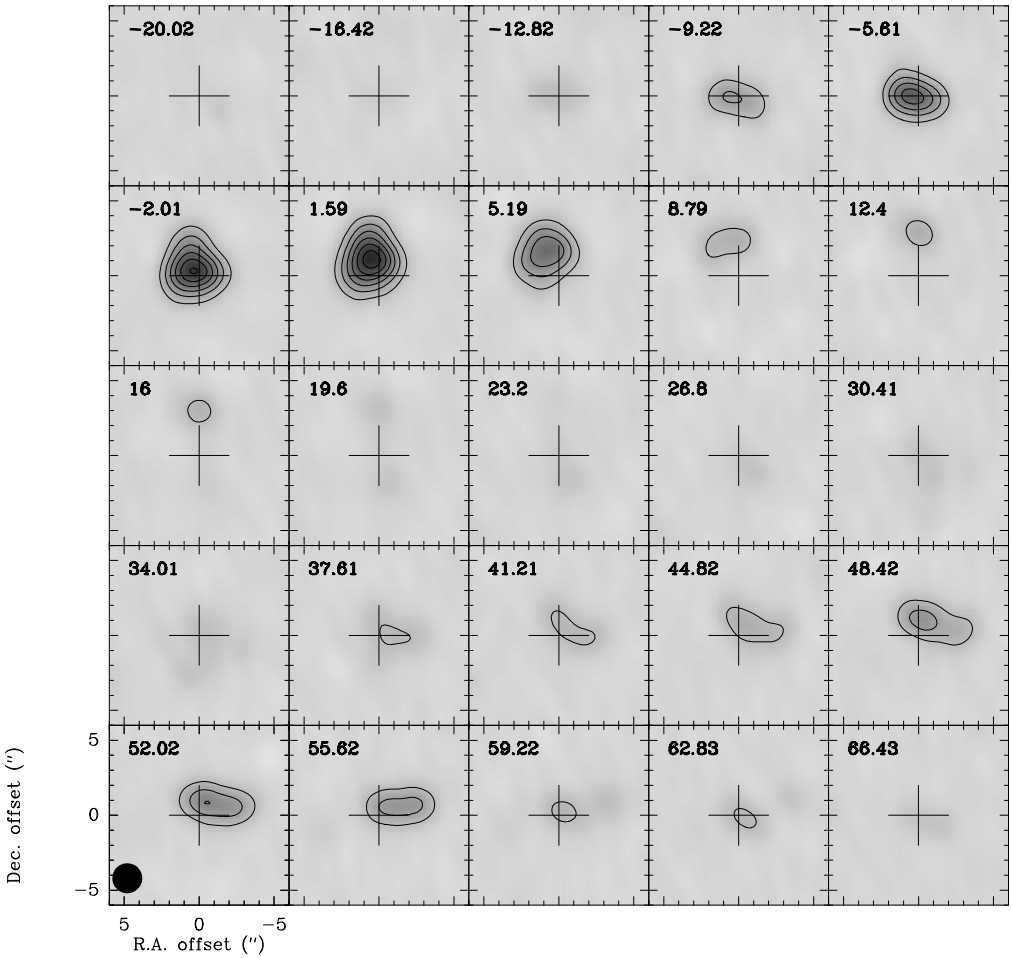

Figure 5.17: Channel maps of $SO_2(3_{1,3}\text{-}2_{0,2})$ and $SO_2(16_{2,14}\text{-}15_{3,13})$ as in Fig. 5.16, but convolved with a $2'' \times 2''$ symmetrical beam (shown in the bottom left corner). Contours are separated by 20 mJy/beam, corresponding to 0.56 K.

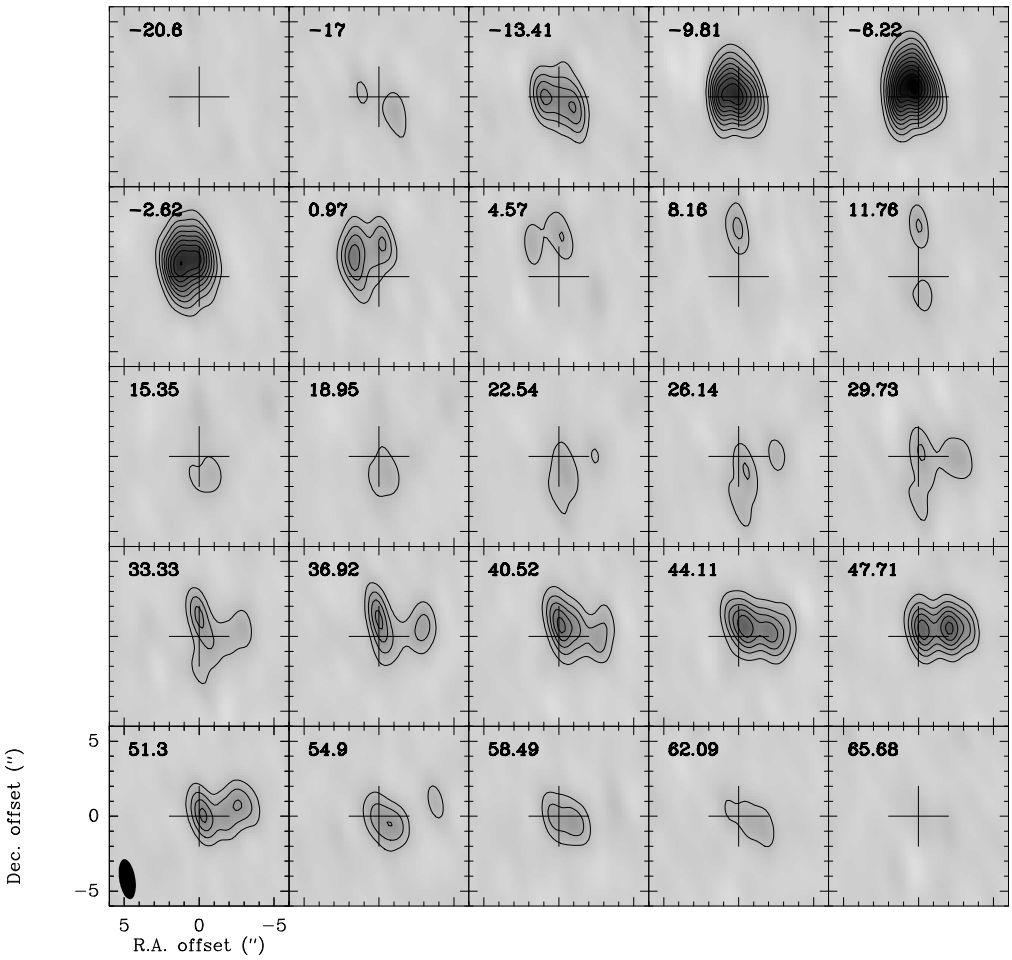

Figure 5.18: Same as Fig. 5.8, but for $SO_2(10_{1,9}\text{-}10_{0,10})$. Contours are separated by 10 mJy/beam, corresponding to 0.38 K. The synthesized beam is $2.72'' \times 1.09''$ with PA 9°.

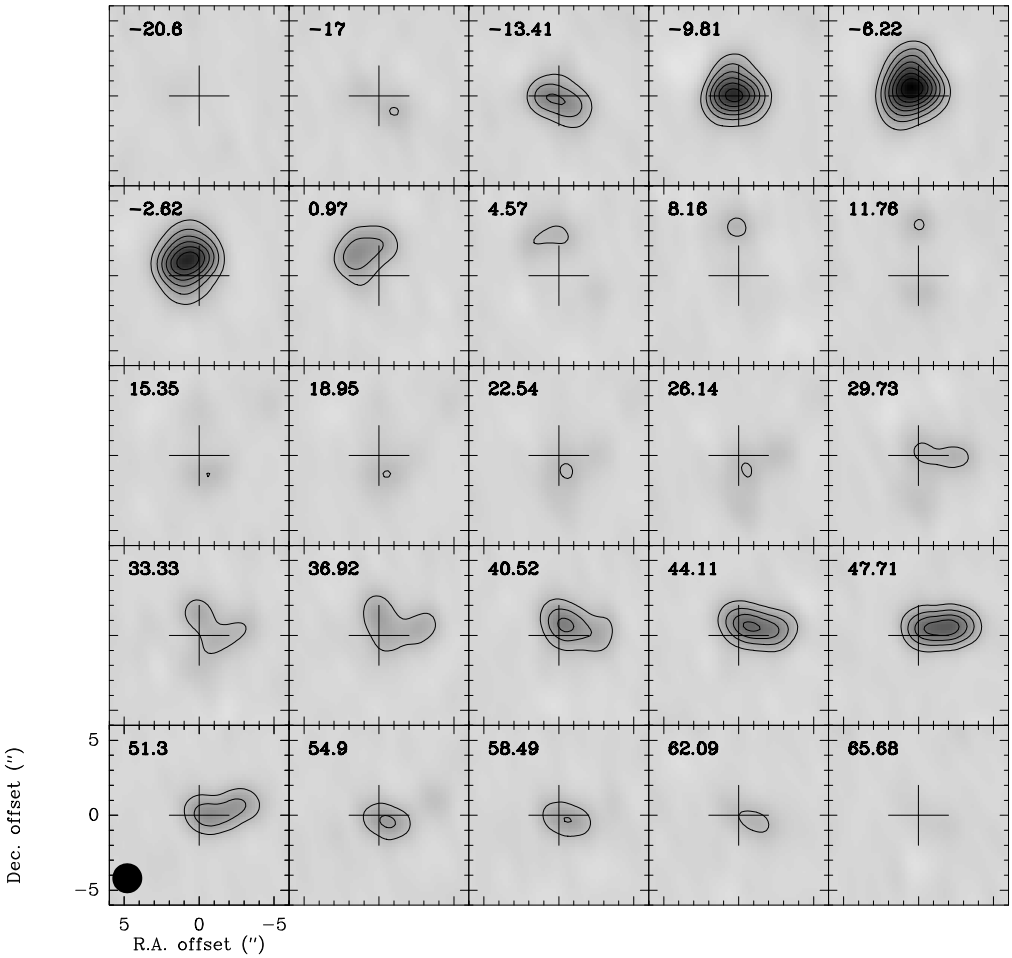

Figure 5.19: Channel maps of $SO_2(10_{1,9}\text{-}10_{0,10})$ as in Fig. 5.18, but convolved with a $2'' \times 2''$ symmetrical beam (shown in the bottom left corner). Contours are separated by 20 mJy/beam, corresponding to 0.56 K.

east, and a weaker redshifted peak $\sim 1''$ north-west of the stellar position at a velocity of 45 km s^{-1}. At the same velocity, a second peak shows up, at a position $2''$ to the west. No emission is seen at the systemic velocity.

Our observations support the model proposed by Muller et al. (2007), consisting of a spherical expanding envelope and a bipolar outflow. The HCN(1-0) and SiS(5-4) channel maps clearly show the blue- ($\sim$ -3 km s^{-1}) and redshifted ($\sim$ 45 km s^{-1}) wings of the outflow, with the redshifted part located more to the west. Both maps also show the contribution of the spherical outflow at the systemic velocity, HCN and SiS are therefore present in all components of the envelope. NaCl, with one emission peak at 22 km s^{-1}, only traces the spherical outflow, whereas SO_2 is present in the bipolar outflow.

The velocity-integrated intensity maps for the different molecules are shown in Fig. 5.20 (see Fig. 5.21 for the symmetrical beam). The 50% contour levels are emphasized by the tick line. We used the GILDAS task `UV_FIT` to fit a 2-dimensional elliptical Gaussian function to the integrated emission in the *uv* plane. HCO^+ was omitted because it only appears in a shell around the stellar position. The resulting flux, position, size and position angle are summarized in Table 5.2.

Given that the emitting region fills the beam, and assuming optically thin lines, we can calculate the column densities towards the peak position as follows for the linear molecules (Goldsmith & Langer 1999):

$$N_u = \frac{3k}{8\pi^3}\frac{1}{\nu\mu^2}\left(\int T_b\, dv\right) \times 10^{39}, \tag{5.17}$$

and similarly for SO_2 (Goldsmith & Langer 1999):

$$N_u = \frac{8\pi k}{hc^3}\frac{\nu^2}{A_{ul}}\left(\int T_b\, dv\right) \times 10^{17}. \tag{5.18}$$

Here, N_u is the column density of the upper transition u in cm^{-2}, k and h the Boltzmann and Planck constants, ν the frequency of the transition in GHz, μ the transition dipole moment in Deybe, A_{ul} the Einstein coefficient for spontaneous emission and $\int T_b\, dv$ the velocity-integrated main-beam brightness temperature in K km s^{-1}. The transition dipole moment for the rotational transition $(J+1, J)$ is defined as

$$\mu^2 = \frac{J+1}{2J+3}\mu_e^2 \tag{5.19}$$

for linear molecules, where we used the values stated in the CDMS database (Müller et al. 2001, 2005) for the permanent dipole moment μ_e. Einstein A coefficients are taken

Table 5.2: Parameters from 2-dimensional elliptical Gaussian fits to the integrated emission in the *uv* plane.

Line	$F_{\rm int}$[a] [Jy km/s]	R.A. offset[b] ["]	Dec. offset[b] ["]	$\theta_{\rm maj}$[c] ["]	$\theta_{\rm min}$[c] ["]	PA[d] [°]	*v*-range [km/s]
88.95 GHz continuum	0.022±0.00[e]	0.08±0.01	-0.04±0.02	0.90±0.10	0.43±0.08	-25.9±8.4	
HCN(1-0)	74.21±0.74	-0.31±0.01	0.04±0.01	3.34±0.03	2.83±0.03	46.6±2.0	[-28,72]
SiS(5-4)	4.30±0.16	-0.24±0.02	-0.06±0.04	1.37±0.17	0.93±0.12	52.7±16.3	[-16,61]
NaCl(7-6)	0.48±0.09	-0.28±0.08	0.21±0.21	2.46±0.71	< 2.46	13.7±6.9	[11,40]
104.20 GHz continuum	0.031±0.00[e]	0.08±0.01	0.03±0.01	0.96±0.08	0.39±0.03	8.9±2.8	
NaCl(8-7)	0.82±0.08	-0.48±0.06	-0.49±0.10	2.22±0.28	0.45±0.36	34.5±6.4	[10,34]
SO_2(*blend*)[f]	13.59±0.63	-0.10±0.03	0.41±0.04	3.97±0.13	3.16±0.09	31.8±4.1	[-16,70]
$SO_2(10_{1,9}\text{-}10_{0,10})$	15.53±0.59	-0.19±0.03	0.17±0.03	3.74±0.10	3.09±0.08	38.9±4.3	[-20,65]

[a] Integrated flux from fitting a 2-dimensional elliptical Gaussian function to the integrated emission in the *uv* plane.
[b] Position offset with respect to the continuum position.
[c] Major and minor axes (FWHM) estimated by the Gaussian fit.
[d] Position angle derived from the Gaussian fit.
[e] Continuum flux in Jy.
[f] Blend of $SO_2(3_{1,3}\text{-}2_{0,2})$ and $SO_2(16_{2,14}\text{-}15_{3,13})$.

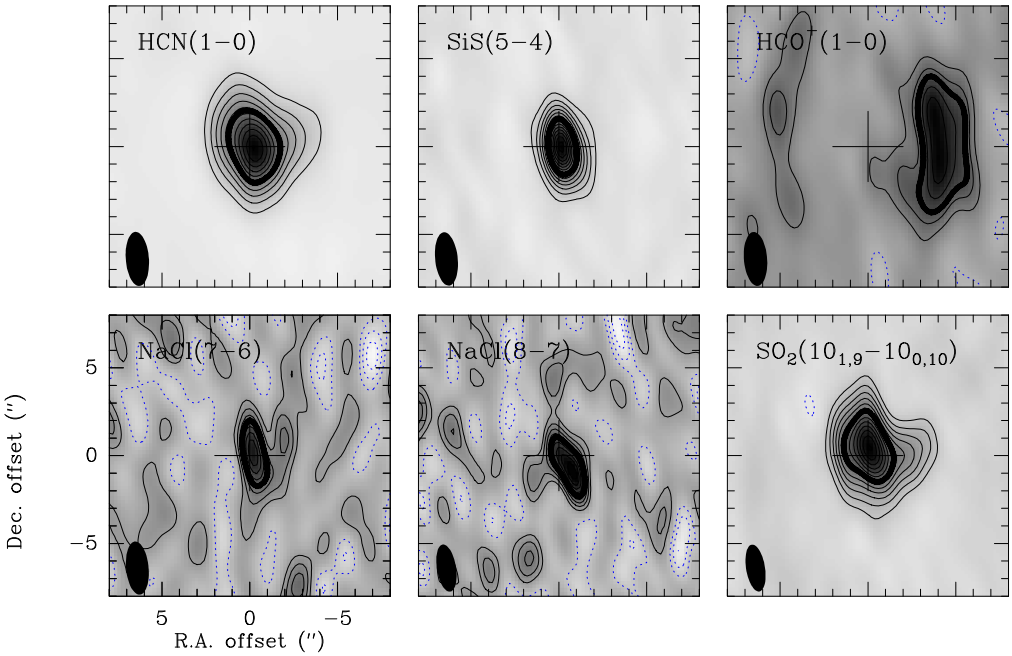

Figure 5.20: Integrated emission maps of HCN(1-0), SiS(5-4), HCO^+(1-0), NaCl(7-6), NaCl(8-7) and $SO_2(10_{1,9}\text{-}10_{0,10})$. The axes denote right ascension and declination offset from the phase center (indicated by the cross) in arcseconds. Contours are separated by respectively 2 Jy/beam km/s, 0.2 Jy/beam km/s, 0.1 Jy/beam km/s, 0.05 Jy/beam km/s, 0.05 Jy/beam km/s and 0.2 Jy/beam km/s. The thick line represents the 50% contour level. The synthesized beams are shown in the bottom left corner.

from the LAMDA-database (Schöier et al. 2005). $\int T_b\, dv$ is obtained by applying the standard conversion from Jy/beam to K (see (5.15)) to the integrated intensities given in the third column of Table 5.3. These integrated intensities resulted from fitting a 2-dimensional elliptical Gaussian function to the emission in Fig. 5.20. Table 5.3 lists the resulting column densities for all observed transitions, except for HCO^+(1-0), for which we didn't calculate the integrated peak intensity, and the blended $SO_2(3_{1,3}\text{-}2_{0,2})$ and $SO_2(16_{2,14}\text{-}15_{3,13})$ lines.

5.5 Line radiative transfer

In the next section, we will construct a model of VY CMa's envelope and calculate the corresponding line profiles for the observed molecular transitions. Therefore, we need to determine the population density of the energy levels between which the specific transitions take place. The population density of level i, however, is connected to the population density of all other energy levels j through the statistical equilibrium equa-

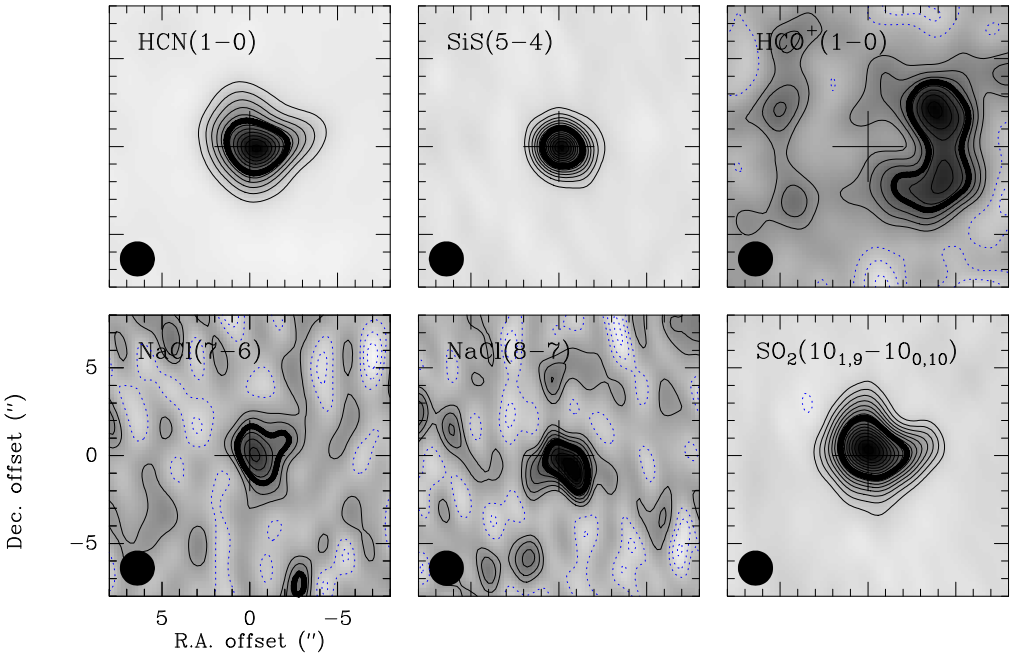

Figure 5.21: Integrated emission maps as in Fig. 5.20, but convolved with a 2″ × 2″ symmetrical beam (shown in the bottom left corner). Contours are separated by respectively 2 Jy/beam km/s, 0.2 Jy/beam km/s, 0.1 Jy/beam km/s, 0.05 Jy/beam km/s, 0.05 Jy/beam km/s and 0.2 Jy/beam km/s. The thick line represents the 50% contour level.

Table 5.3: Upper state column densities (cm^{-2}) towards the peak position of the integrated emission.

Line	σ[a] [Jy/beam km/s]	F_{peak}[b]	N_u[c] [cm^{-2}]
HCN(1-0)	0.19	20.86	5.05×10^{14}
SiS(5-4)	0.05	2.81	1.44×10^{14}
NaCl(7-6)	0.05	0.31	5.67×10^{11}
NaCl(8-7)	0.05	0.47	7.42×10^{11}
$SO_2(10_{1,9}\text{-}10_{0,10})$	0.06	2.44	1.89×10^{14}

[a] Noise in the velocity-integrated emission maps of Fig. 5.20.
[b] Peak flux from fitting a 2-dimensional elliptical Gaussian function to the integrated emission maps of Fig. 5.20.
[c] Upper state column densities (cm^{-2}).

tions, describing the balance between population and depopulation of the energy levels (see Poelman & Spaans (2005, 2006))

$$n_i(x,y,z)\sum_{j\neq i}^{l} R_{ij}(x,y,z) = \sum_{j\neq i}^{l} n_j(x,y,z)R_{ji}(x,y,z). \tag{5.20}$$

In the above equation, n_i denotes the population density of level i (cm^{-3}), l the total number of levels considered, and

$$R_{ij}(x,y,z) = \begin{cases} A_{ij} + B_{ij}\langle J_{ij}\rangle + C_{ij}(x,y,z) & (i > j) \\ B_{ij}\langle J_{ij}\rangle + C_{ij}(x,y,z) & (i < j). \end{cases} \tag{5.21}$$

R_{ij} is a function of the Einstein A_{ij} and B_{ij} coefficients, the collisional rate coefficients C_{ij} and the mean integrated radiation field $\langle J_{ij}\rangle$ at the frequency ν_{ij} of the transition between level i and j. The Einstein A and B coefficients are related through the Einstein relations

$$g_i B_{ij} = g_j B_{ji}, \tag{5.22}$$

$$A_{ji} = \frac{8\pi h\nu^3}{c^3} B_{ji}. \tag{5.23}$$

In order to solve the statistical equilibrium equations (5.20) and determine the level populations, we will use the radiative transfer code "β3D" developed by Poelman & Spaans (2005, 2006). They apply a multi-zone escape probability method, which is based on the Sobolev approximation. The difficulty of solving the statistical equilibrium equations is in the dependence on the radiation field $\langle J_{ij}\rangle$, whose value is a priori unknown. In the Sobolev approximation for large velocity gradients, it is assumed that the radiation field can be calculated locally, independent of the field at other locations further away (Sobolev 1960). With this simplification we can write an expression for $\langle J_{ij}\rangle$, according to Poelman & Spaans (2005, 2006):

$$\langle J_{ij}(x,y,z)\rangle = [1-\beta_{ij}(x,y,z)]\,S_{ij}(x,y,z) + \beta_{ij}(x,y,z)B_{ij}^{\rm bg}(\nu_{ij}, T_{BB}). \tag{5.24}$$

β_{ij} is called the photon escape probability, S_{ij} represents the source function and $B_{ij}^{\rm bg}$ the background radiation. Thus, if $\beta_{ij} = 1$ and all photons escape, $\langle J_{ij}(x,y,z)\rangle = B_{ij}^{\rm bg}(\nu_{ij}, T_{BB})$. On the other hand, if $\beta_{ij} = 0$ and no photons escape, $\langle J_{ij}(x,y,z)\rangle$ is equal to the local source function

$$S_{ij}(x,y,z) = \frac{2h\nu_{ij}^3}{c^2}\left[\frac{n_j(x,y,z)g_i}{n_i(x,y,z)g_j} - 1\right]^{-1}, \tag{5.25}$$

where g_i is the statistical weight of level i.

The escape probability is a function of the optical depth τ. For a photon emitted from a transition between level i and j at position (x, y, z) along the direction $\vec{k}$, the probability to escape is given by

$$\beta_{ij}(x, y, z, \vec{k}) = \frac{1 - \exp(-\tau_{ij}(x, y, z, \vec{k}))}{\tau_{ij}(x, y, z, \vec{k})}. \tag{5.26}$$

Thus, once we know the optical depth in each gridpoint (x, y, z), we can calculate the escape probability and solve the statistical equilibrium equations.

If we consider both thermal and turbulent line broadening, the line profile follows a Gaussian distribution

$$\phi_{ij}(\nu) = \frac{e^{-(\nu-\nu_{ij})^2/\Delta\nu_d^2}}{\sqrt{\pi}\Delta\nu_d}, \tag{5.27}$$

with the Doppler width $\Delta\nu_d = \frac{\nu_{ij}}{c}\Delta v_d = \frac{\nu_{ij}}{c}(v_{th}^2 + v_{turb}^2)^{1/2}$. The optical depth averaged over the line between two gridpoints $s_1(x_1, y_1, z_1)$ and $s_2(x_2, y_2, z_2)$ with $ds = s_1 - s_2$ is then (Poelman & Spaans 2005, 2006)

$$\tau_{ij}(x, y, z, \vec{k}) = \frac{h\nu}{4\pi} n_j(x, y, z) B_{ji} \left(1 - \frac{n_i g_j}{n_j g_i}\right) \phi_{ij}(\nu)\, ds. \tag{5.28}$$

The program works in an iterative way. Initially, the levels populations are derived from a Boltzmann distribution. With these population densities, the optical depth τ is calculated according to (5.28), which allows the determination of β_{ij} via (5.26). The source function is computed from (5.25) using the initial-guess population densities. (5.24) now gives the value of the mean radiation field $\langle J_{ij} \rangle$, which is used to solve the statistical equilibrium equations (5.20) for the population densities n_i. The updated values of n_i are subsequently used as a starting point for the next iteration loop, until convergence is reached.

5.6 Modeling the envelope

We have modeled the emission of HCN(1-0), SiS(5-4) and $SO_2(10_{1,9}\text{-}10_{0,10})$ and determined molecular abundances throughout the envelope of VY CMa. We didn't include $SO_2(3_{1,3}\text{-}2_{0,2})$ and $SO_2(16_{2,14}\text{-}15_{3,13})$ because these lines are blended, nor NaCl(7-6) and NaCl(8-7) as there are no collisional rate coefficients available for NaCl. Since we

have clear evidence for the existence of a spherical envelope and a bipolar outflow, we use the geometries proposed by Muller et al. (2007) and Ziurys et al. (2009) as a starting point. The peculiar appearance of the HCO^+(1-0) emission (see Fig. 5.12-5.13) suggests a more complex geometry. Therefore, we also excluded HCO^+ from our current modeling attempt.

Ziurys et al. (2009) assume a simple H_2 density distribution for the outflow and the spherical part, $n(r) \propto r^{-2}$. The kinetic temperature of the gas follows a power law $T \propto r^{-0.62}$. The expansion velocity in the envelope is set to 20 km s^{-1}. They distinguish between the red and blue lobe of the bipolar outflow, which both have an opening angle of 45° but each have their own inclination angle and expansion velocity. The redshifted flow is inclined 45° off the line-of-sight and has an expansion velocity of 42 km s^{-1}. The blueshifted part inclines 20° off the line-of-sight with $v_{\rm exp}$ = 38 km s^{-1}.

Based on 1.3 mm observations of CO lines, Muller et al. (2007) construct a more complex model of the envelope. They assume a less common H_2 density distribution for the spherical envelope: $n(r) \propto r^{-2.5}$. For the bipolar outflow, a constant H_2 density is taken in the inner region, and they introduce a density enhancement towards the outer part, in order to explain the presence of strong emission peaks at larger velocity offsets. The kinetic temperature profile is given by $T(r) \propto r^{-0.7}$. The expansion velocity in the envelope differs slightly from the value adopted by Ziurys et al. (2009), $v_{\rm exp}$ = 15 km s^{-1}. The velocity in the outflow increases outward from 15 km s^{-1} to 45 km s^{-1}, but also depends on the polar angle. Muller et al. (2007) derive a wide opening angle of 120° and an inclination angle of 15° with respect to the line-of-sight. We present a comparison between the geometry of Muller et al. (2007) and Ziurys et al. (2009) in Table 5.4.

We used both setups as input for the radiative transfer code of Poelman & Spaans (2005, 2006) described in Section 5.5. The calculations are performed on a grid of $178 \times 178 \times 178$ points. We take 30, 41 and 45 rotational levels in the ground vibrational state into account for respectively HCN, SiS and SO_2. Einstein A coefficients, energy levels, statistical weights and collisional rate coefficients for collisions with H_2 are taken from the atomic and molecular database introduced by Schöier et al. (2005). The Doppler width, used to define the line profile over which to integrate, is set to 1 km s^{-1} in the spherical envelope and to 3 km s^{-1} in the bipolar outflow, as proposed by Muller et al. (2007). The molecular abundance (relative to H_2) is left as a free parameter, and has to be defined separately for the spherical part and the outflow. Once the level populations have been calculated, we use the ray tracing program SKY (part of the radiative transfer code RATRAN, developed by Hogerheijde & van der Tak (2000)) to

Table 5.4: Comparison between the model geometry used by Muller et al. (2007) and Ziurys et al. (2009).

Parameter	Muller et al. (2007)	Ziurys et al. (2009)
Envelope gas density*	$4.5 \times 10^5 \left(\frac{10^{16}\ \mathrm{cm}}{r}\right)^{2.5}\ \mathrm{cm}^{-3}$	$\frac{\dot{M}}{4\pi v_{\exp}(1-\frac{R_*}{r})r^2}\ \mathrm{g\ cm}^{-3}$
Outflow gas density*	$\begin{cases} 6\times10^4\ \mathrm{cm}^{-3} \\ \quad \text{for } r < 5\times10^{16}\ \mathrm{cm} \\ 10^5\ \mathrm{cm}^{-3} \\ \quad \text{for } 5\times10^{16}\ \mathrm{cm} < r < 7\times10^{16}\ \mathrm{cm} \\ 10^5\,(7\times10^{16}\ \mathrm{cm}/r)^2\ \mathrm{cm}^{-3} \\ \quad \text{for } r > 7\times10^{16}\ \mathrm{cm} \end{cases}$	$\frac{\dot{M}}{4\pi v_{\exp}(1-\frac{R_*}{r})r^2}\ \mathrm{g\ cm}^{-3}$
Envelope gas temperature	$500 \left(\frac{2.25\times10^{15}\ \mathrm{cm}}{r}\right)^{0.7}\ \mathrm{K}$	$230 \left(\frac{10^{16}\ \mathrm{cm}}{r}\right)^{0.62}\ \mathrm{K}$
Outflow gas temperature	$\begin{cases} 150\,(1.5\times10^{16}\ \mathrm{cm}/r)^{0.7}\ \mathrm{K} \\ \quad \text{for } r < 5\times10^{16}\ \mathrm{cm} \\ 35\ \mathrm{K} \\ \quad \text{for } 5\times10^{16}\ \mathrm{cm} < r < 7\times10^{16}\ \mathrm{cm} \\ 35\,(7\times10^{16}\ \mathrm{cm}/r)\ \mathrm{K} \\ \quad \text{for } r > 7\times10^{16}\ \mathrm{cm} \end{cases}$	$230 \left(\frac{10^{16}\ \mathrm{cm}}{r}\right)^{0.62}\ \mathrm{K}$
Envelope $v_{\exp}$	$15\ \mathrm{km\ s}^{-1}$	$20\ \mathrm{km\ s}^{-1}$
Outflow $v_{\exp}$	$\left(30 - \frac{10\tan\theta}{\tan(60°)}\right)\frac{r}{R_{\mathrm{out}}} + 15\ \mathrm{km\ s}^{-1}$	Blue: $38\ \mathrm{km\ s}^{-1}$ Red: $42\ \mathrm{km\ s}^{-1}$
Opening angle	120°	45°
Inclination	15°	Blue: 20° Red: 45°

* In Muller et al. (2007), the density is given as $n(r)$ (in cm^{-3}), in Ziurys et al. (2009) as $\rho(r)$ (in $\mathrm{g\ cm}^{-3}$). Both are related through $n = \frac{N_A}{M}\rho$, with N_A the Avogadro constant and M the molecular mass.

calculate the emission distribution on the sky. After convolution with the corresponding telescope beam (see Table 5.1), we obtain the line profile and channel maps of each molecule, which can be compared with our observational results.

We adapted the initial abundances until we found the best visual correspondence between the model outcome and our observations. However, both the geometry of Muller et al. (2007) and Ziurys et al. (2009) failed to provide a satisfying result. As an example, Fig. 5.22 shows the HCN(1-0) line profiles at the phase center, calculated from the setup given by Muller et al. (2007) for 2 different input abundances. For the left plot, we assumed an equal HCN abundance in the envelope and bipolar outflow, as in Muller et al. (2007). Clearly, this results in a much too centrally peaked spectrum. Therefore, we also tried to vary the abundance throughout envelope and outflow, which improves the outcome considerably. The calculated profile is shown in the right panel of Fig. 5.22. Although the spectrum now displays the expected blue and red peaks characteristic of the outflow, the peak velocity doesn't occur at the right value.

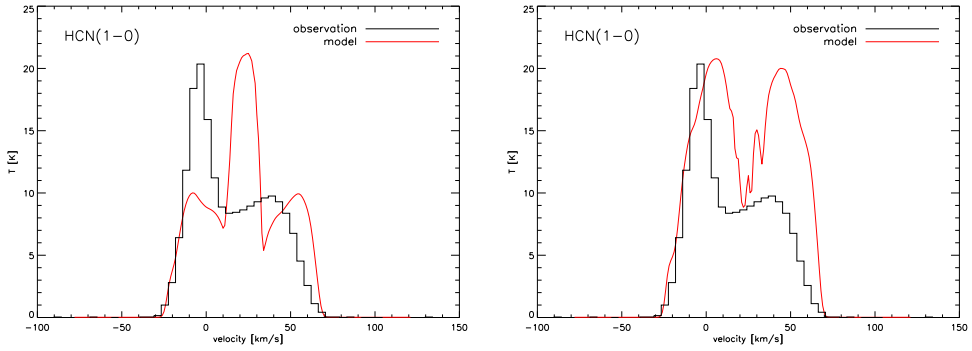

Figure 5.22: Line profiles of HCN(1-0) calculated from the geometry proposed by Muller et al. (2007) (red), compared with the observed profiles (black). The spectra are taken at the phase center. *Left*: The HCN abundance is equal in the spherical envelope and bipolar outflow. *Right*: Envelope and outflow have a different HCN abundance.

Therefore, we tested the influence of each parameter of the model, checking the two geometries against each other. The best option was kept for our final model setup. For the H_2 density in the envelope, the distribution of Muller et al. (2007) was chosen:

$$n(r) = 4.5 \times 10^5 \left(\frac{10^{16}\ \mathrm{cm}}{r} \right)^{2.5} . \tag{5.29}$$

The authors introduced a constant density ($n(r) = 6 \times 10^4$ cm^{-3}) in the inner part of the outflow, a density enhancement between 5×10^{16} cm and 7×10^{16} cm ($n(r) = 10^5$ cm^{-3}) and $n(r) \propto r^{-2}$ further on. This is based on a constant CO/H_2 abundance (Kemper et al. 2003) throughout the outflow. Since we model several molecules, it is more convenient to assume a uniform density distribution in the outflow, and define a separate abundance for the three parts of the outflow:

1) $r < 5 \times 10^{16}$ cm,
2) 5×10^{16} cm $< r < 7 \times 10^{16}$ cm,
3) $r > 7 \times 10^{16}$ cm.

A constant H_2 density of 10^5 cm^{-3} is adopted for the red and blue flows. We decided to work with the kinetic temperature profile of Muller et al. (2007), although there was little difference when changing it. Therefore,

$$T(r) = 500 \text{ K} \left(\frac{2.25 \times 10^{15} \text{ cm}}{r} \right)^{0.7}. \tag{5.30}$$

Kemper et al. (2003) give an expression for the expansion velocity in outflows of AGB and red supergiant stars. We apply this for the spherical part of our model, which means

$$v_{\text{exp}}(r) = 15 \text{ km s}^{-1} \left(1 - \frac{1.188 \times 10^{14} \text{ cm}}{r} \right). \tag{5.31}$$

Our tests show that the expansion velocity in the outflow should increase outwards, as mentioned by Muller et al. (2007). Their model also included, apart from the radial increase in velocity, a dependence on the polar angle, measured from the polar axis. We find, however, that such models produce emission peaks at too low velocities. We thus only assume a linear, radial increase from 15 km s^{-1} to 45 km s^{-1} of v_{exp} in the outflow. An overview of our setup is given in Table 5.5.

With the model parameters set, the best-fit abundances were calculated. The results are listed in Table 5.6, predicted channel maps and spectra are shown in Fig. 5.23 - 5.25.

In general, our model reproduces the observed emission better along the north-south than along the east-west direction. This is also clear from the spectra in the bottom panels of Fig. 5.23-5.25, where, unlike at ΔR.A = 0", we overestimate the flux at an offset of 1" east and west of the stellar position. We were not able to fit the asymmetry in the double-peaked profile of HCN(1-0) (Fig. 5.23). Therefore, we chose the parameters such that the strongest blueshifted peak is well represented by our model. The HCN abundances shown in Table 5.6 are about a factor of 10 lower than those derived by Ziurys et al. (2009) (i.e. 1.2×10^{-6} for the spherical part, 7.5×10^{-6} for the outflow). Given that they assumed a larger distance of 1.5 kpc, we can still conclude that the ratio between the abundance in the spherical envelope and the bipolar outflow is similar in both models.

SiS (Fig. 5.24) is present in all parts of the envelope, as predicted by Ziurys et al. (2007), but is a factor 10 more abundant in the spherical part than in the outflow.

Table 5.5: The geometry used in our modeling.

Parameter	Value
Envelope gas density	$4.5 \times 10^5 \left(\frac{10^{16}\ \mathrm{cm}}{r}\right)^{2.5}\ \mathrm{cm}^{-3}$
Outflow gas density	$10^5\ \mathrm{cm}^{-3}$
Envelope gas temperature	$500 \left(\frac{2.25\times10^{15}\ \mathrm{cm}}{r}\right)^{0.7}\ \mathrm{K}$
Outflow gas temperature	$500 \left(\frac{2.25\times10^{15}\ \mathrm{cm}}{r}\right)^{0.7}\ \mathrm{K}$
Envelope v_{exp}	$15\ \mathrm{km\ s}^{-1} \left(1 - \frac{1.188\times10^{14}\ \mathrm{cm}}{r}\right)$
Outflow v_{exp}	$30\frac{r}{R_{\mathrm{out}}} + 15\ \mathrm{km\ s}^{-1}$
Opening angle	120°
Inclination	15°

Table 5.6: Molecular abundances relative to H_2.

Molecule	Abundance			
	spherical	outflow 1[a]	outflow 2[b]	outflow 3[c]
HCN	1.5×10^{-7}	8.0×10^{-7}	1.0×10^{-6}	8.0×10^{-7}
SiS	4.0×10^{-7}	6.0×10^{-8}	2.0×10^{-8}	2.0×10^{-8}
SO_2	3.0×10^{-9}	2.5×10^{-6}	2.5×10^{-6}	2.0×10^{-6}

[a] $r < 5 \times 10^{16}$ cm
[b] 5×10^{16} cm $< r < 7 \times 10^{16}$ cm
[c] $r > 7 \times 10^{16}$ cm

Though too extended in the east-west direction, the model fits perfectly to the observations along the north-south axis. As for HCN(1-0), we were unable to reproduce the asymmetric blue and red peaks of the $SO_2(10_{1,9}\text{-}10_{0,10})$ line (Fig. 5.25). Therefore, we again focused on the stronger blueshifted part. SO_2 is mainly abundant in the outflow, but a low fraction had to be added to the spherical part as well, in order to account for

some emission around the systemic velocity.

5.7 Conclusions

We used the Plateau de Bure interferometer to observe a number of molecular species in the circumstellar environment of the red supergiant VY CMa. We were able to detect emission from HCN(1-0), HCO^+(1-0), SiS(5-4), NaCl(7-6), NaCl(8-7), $SO_2(3_{1,3}\text{-}2_{0,2})$, $SO_2(16_{2,14}\text{-}15_{3,13})$ and $SO_2(10_{1,9}\text{-}10_{0,10})$. Inspection of the channel maps confirmed previous results (e.g. Muller et al. 2007; Ziurys et al. 2009)) that the envelope consists of a spherically symmetric shell and a high-velocity bipolar outflow. Moreover, since we observed several molecules and made use of the imaging advantages of interferometry, we could perform a more detailed analysis of the emission regions than above-mentioned authors. NaCl is found to be present only in the spherical part, whereas SO_2 appears almost exclusively in the outflow. HCN and SiS, on the other hand, are seen in all parts of the envelope. We constructed a model using the geometry of a spherical envelope plus bipolar outflow, characterized by an opening angle of 120°, constant H_2 density and an expansion velocity increasing linearly from 15 km s^{-1} to 45 km s^{-1}. This allowed us to reproduce the observed channel maps and determine molecular abundances for HCN, SiS and SO_2. The predicted channel maps fit well to the observed ones, even though we were not able to recreate the asymmetry of the double-peaked profile, and our results match the observations better along a north-south offset from the phase center than along an east-west. Given the complexity of VY CMa's circumstellar environment, we did not expect a perfect fit, and these new results definitely brought us one step closer to a complete picture of this interesting object.

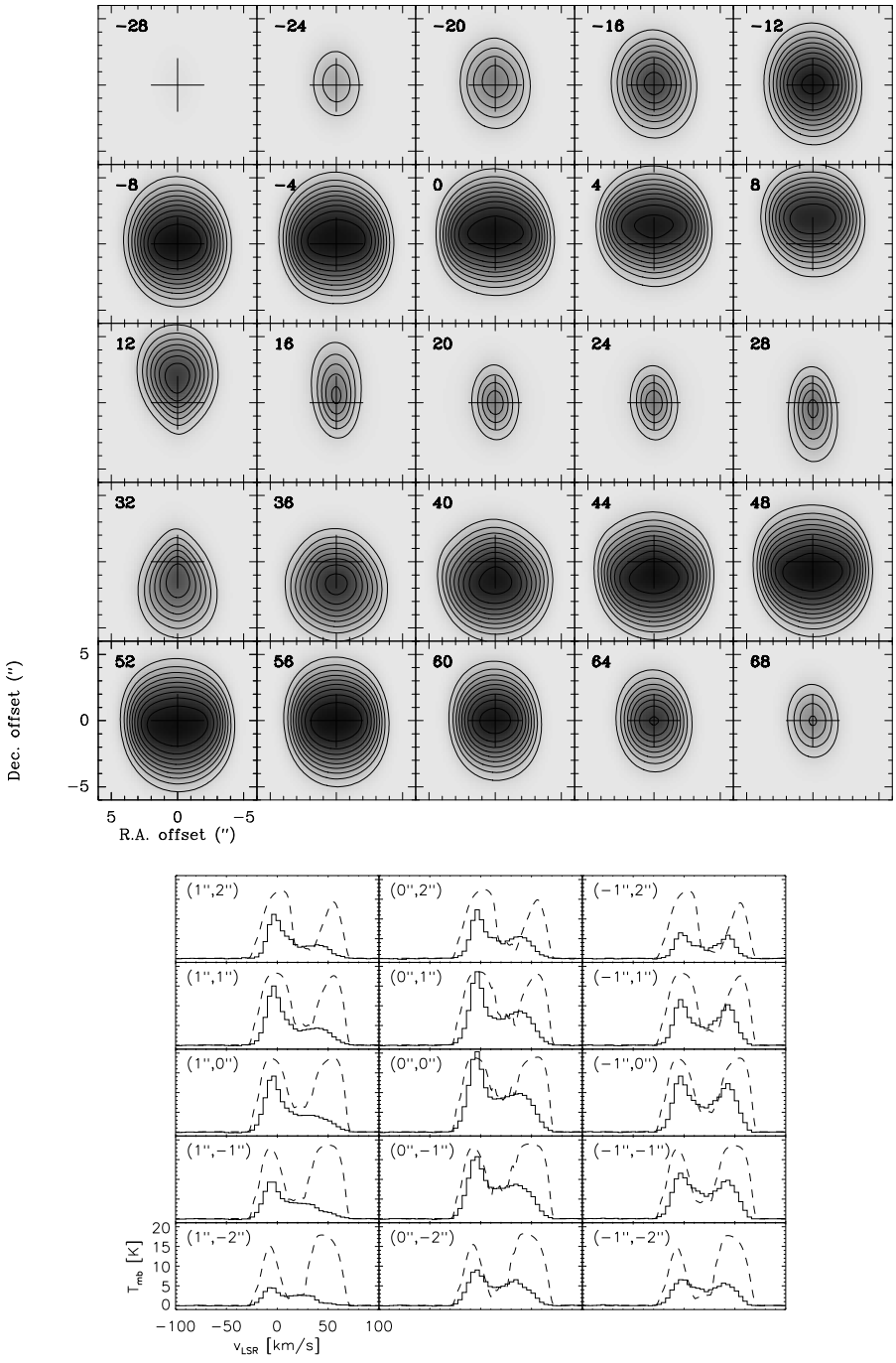

Figure 5.23: *Top*: Simulated channel maps of HCN(1-0). The contours are separated by 1.92 K, as in Fig. 5.8. *Bottom*: Spectra of the HCN(1-0) line observed with the PdB interferometer (solid lines), taken at different positions. The offset from the phase center is shown in the top left corner of each pannel. Overplotted are the predicted model spectra (dashed lines).

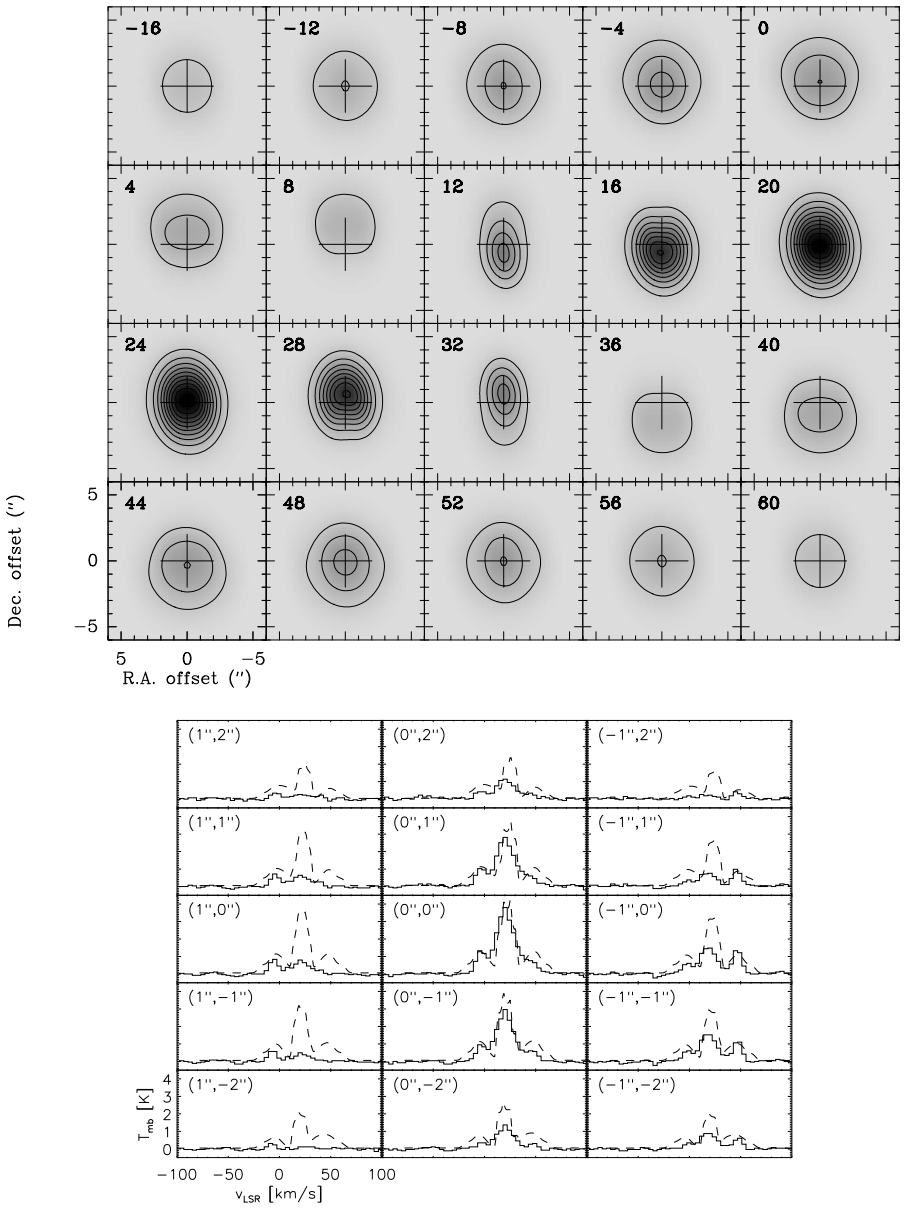

Figure 5.24: Same as Fig. 5.23, but for SiS(5-4). The contours are separated by 0.38 K, as in Fig. 5.10.

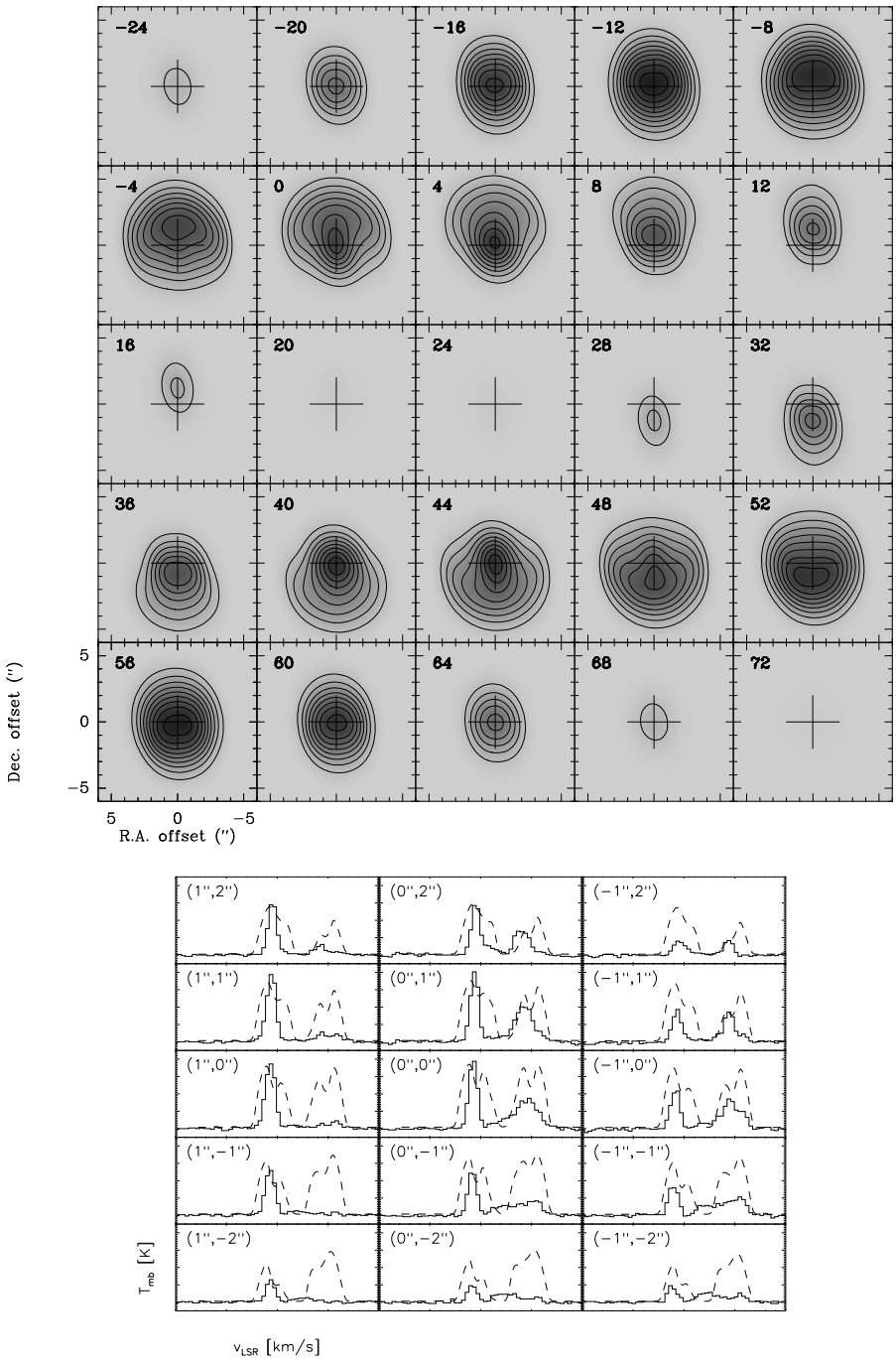

Figure 5.25: Same as Fig. 5.23, but for $SO_2(10_{1,9}\text{-}10_{0,10})$. The contours are separated by 0.38 K, as in Fig. 5.18.

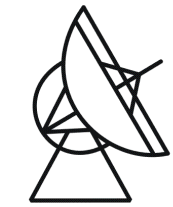

Max-Planck-Institut
für Radioastronomie

6
Conclusions

Among the multitude of stellar objects, red supergiants represent a fascinating group. Only stars with masses between 8 and 30 $M_{\odot}$ will pass through this phase near the end of their life, after leaving the main sequence and before exploding as a core-collapse supernovae. Due to the short lifetime of this evolutionary phase, RSGs are not very numerous, and many of their characteristics are still unclear. While it is well-known that they are generally surrounded by a dusty circumstellar envelope, the physics of this envelope is not yet fully understood. Studies of large samples of RSGs are essential if one wants to get a complete picture of the red supergiant state. Such analyses are hampered by the fact that only a limited number of RSGs have been detected as a consequence of their short lifetime, which makes it difficult to derive statistical properties. Additionally, detailed exploration of individual objects is necessary. Indeed, several peculiar red supergiants have been identified, with properties deviating from those of the standard red supergiant population.

In this work, we contributed to both the study of large groups of RSGs and the investigation of individual objects. To begin with, we analyzed the masing properties of a sample of Galactic RSG stars, by means of observations of the SiO maser at 86 GHz, common in RSGs. In the rest of this thesis, we concentrated on the peculiar hypergiant VY CMa, one of the most interesting objects among the RSGs.

Red supergiants are characterized by high mass-loss, which creates the typical circumstellar envelope. These envelopes have been subject to a multitude of studies. Thanks to the low temperatures of the envelope, they are an ideal environment for the formation of dust grains. The presence of dust causes the spectral energy distribution of RSGs to show a large infrared excess. Often, the circumstellar envelopes are known to harbor maser emission from SiO, H_2O and OH.

The SiO maser was the subject of Chapter 2. SiO masers are extremely useful to determine stellar line-of-sight velocities. Such velocities are essential in studies of the inner Galactic structure. Since many of the known RSG clusters are located near the endpoint of the Galactic bar, an analysis of these populations can provide important input for the modeling of the Galactic kinematics. Apart from that, the SiO masers are also interesting on their own. The relation between the maser intensity and IR flux has been studied before, but several questions remain. Unfortunately, a coherent study of SiO maser occurrence among Galactic RSGs had not been conducted. Only individual object or clusters were studied before. Therefore, we selected for the first time a complete sample of around 90 RSGs in Galactic open clusters and searched for the SiO ($v = 1, J = 2 - 1$) maser at 86 GHz with the IRAM 30m telescope. By focusing on RSGs in stellar clusters, source-specific properties of the SiO maser can be derived. Indeed, cluster stars are formed in an equal environment with equal metallicity, at the same time and at the same distance from us, and only individual characteristics of each RSG will determine whether an SiO maser is present or not.

The observed sample consisted of 88 (candidate) red supergiants in the Galactic clusters RSGC1, RSGC2, RSGC3, NGC 7419, Perseus OB1, GLIMPSE9 and GLIMPSE 13, SGR 1900+14, MFD2008, Trumpler 27 and two collections of RSGs near the Galactic center, detected by Blum et al. (2003) and Comerón et al. (2004). Additionally, we observed two Mira variables for comparison. In total, we detected SiO maser emission from 13 RSGs and from the 2 Mira variables. One of the reported masers was a new detection. From the line profiles it was clear that the RSG masers tend to cover a wider velocity range than the masers in the Mira variables. We compared the 86 GHz peak intensity derived from our observations, with the 43 GHz peak intensity listed in the literature. Among the 12 RSGs that were detected in both transitions, 10 of them had stronger emission at 86 GHz. This proved that the 86 GHz line is the best transition to study radial velocities in our sample of Galactic red supergiants. From an analysis of color properties, we concluded that the maser detections occurred in the reddest sources and the strongest mid-infrared sources. This result contributes to the evidence of a radiative pumping mechanism for the SiO maser in these Galactic RSGs.

In Chapter 3 we introduced the red supergiant VY CMa. While typical RSGs are already extreme in terms of mass-loss and luminosity, VY CMa is even more extraordinary. This hypergiant has a luminosity of $3 \times 10^5\ L_\odot$ and is losing mass at a rate of 2-4$\times 10^{-4}\ M_\odot\ \mathrm{yr}^{-1}$. The spectral energy distribution of VY CMa shows a large infrared excess caused by its circumstellar envelope. Optical and IR observations have revealed the asymmetry of this envelope. In the next chapters, we tried to construct a model of VY CMa's circumstellar environment. We first concentrated on the dust characteristics, next we examined the gas phase molecules.

The spectral energy distribution with its IR excess was investigated in Chapter 4. Because of the existence of a large amount of dust grains within the envelope, stellar photons will be scattered or absorbed and reemitted by these dust particles before they reach the observer. Therefore, the shape of the SED can only be understood if one understands the physics of radiative transfer. The transfer equation describes exactly how the stellar radiation is changed by the dust, and how the emergent SED will look. After a short introduction into radiative transfer, we introduced three different methods to solve the transfer problem. As a starting point, we assumed a spherically symmetric envelope, and we used a basic Monte Carlo program. This assumption was mainly made in order to simplify the problem, and familiarize ourselves with radiative transfer calculations. As a consequence, the resulting SED was a poor fit to the observations, and applying a more complex 2-dimensional geometry was necessary.

The optical and IR images introduced in Chapter 3 provided evidence for the existence of a disk of dust around VY CMa. Thus, in the second part of Chapter 4 we used the geometry of such a disk as input for the radiative transfer code LELUYA. LELUYA was developed especially to handle axially symmetric distributions. It uses an adaptive grid which traces gradients in density and optical depth. By applying a scaling approach, all parameters become dimensionless and only the temperature of dust condensation has to be specified. Unfortunately, LELUYA is not time efficient, and one model calculation takes up to 4 days. Therefore, we only calculated a small number of models. After a smart initial guess, we refined the parameters until we obtained a good fit to the observed spectral energy distribution. Though providing a more than acceptable fit, the best model had rather suspicious input parameters. The stellar temperature had to be set to 3500 K, while the literature clearly points towards 2800 K. Moreover, we had to introduce a dust mixture which consisted of 70% of carbonaceous grains, and only 30% of silicates. Since VY CMa is an oxygen-rich star, such a high fraction of carbon grains is unrealistic. However, when changing the input parameters to more ideal values, the resulting spectrum was a bad fit to the observations.

Due to the long computational time, it was impossible to perform a parameter study, or to try and improve the results. Therefore the last part of Chapter 4 focused on a third radiative transfer program, MCMax. It is based on a Monte Carlo method, can handle 2-dimensional disk geometries, and unlike LELUYA only needs about 30-60 minutes to perform a full model calculation. This enabled us to scan the parameter space and calculate a total of more than 3000 models. We examined the effects of using both a black body and a MARCS model atmosphere as central source. However, it became immediately clear that in order to obtain the right flux levels in the optical and near-IR, a lower temperature of 2800 K is favored, and MARCS models are only available from 3000 K on. Therefore, we decided to concentrate only on the black body models for our final result. The dust mixture was a crucial point of LELUYA. Strangely, only a mixture with a unrealistically high carbon fraction was able to provide an acceptable fit to the observed SED, while the same input in MCMax didn't result in a good fit. Therefore, we changed the dust composition, based on results from the literature. Finally, we concluded that the dust in VY CMa's circumstellar disk consists of 50% metallic iron, 30% alumina, 10% olivine and 10% melilite. The disk has a surface density $\Sigma \propto r^{-1}$ and a total dust mass of 10^{-3} $M_{\odot}$. The central star is represented by a black body of 2800 K. The stellar radius was found to be 2000 $R_{\odot}$ and the stellar mass 15 $M_{\odot}$. We observe the disk under an inclination angle of 55°.

Finally, in Chapter 5 we used the PdB interferometer to probe the envelope of VY CMa by observing different molecular lines, which are known to trace different regions of the envelope. Previous observations of selected molecules by Muller et al. (2007) and Ziurys et al. (2007, 2009) revealed that the envelope contains a bipolar outflow. They found that certain molecules are only present in the spherical part of the envelope, others only in the outflow, and a last group is located in all parts. Interferometry offers the advantage of imaging and high resolution. This allowed to investigate the different regions of VY CMa's circumstellar environment, by selecting a set of molecular transitions that are expected to trace the different parts. For the first time, such a wide variety of molecules was mapped in such detail around VY CMa. After a short introduction to radio interferometry, we presented the results of our observations with the Plateau de Bure interferometer. We observed 2 frequency setups, at 90 GHz and 104 GHz respectively. These frequency ranges are expected to contain emission from HCN(1-0), HCO^+(1-0), HNC(1-0), SiS(5-4), NaCl(7-6), NaCl(8-7), $SO_2(3_{1,3}\text{-}2_{0,2})$, $SO_2(16_{2,14}\text{-}15_{3,13})$ and $SO_2(10_{1,9}\text{-}10_{0,10})$. We detected emission from all transitions, apart from HNC(1-0). Channels maps supported the existence of the proposed bipolar outflow. Clearly, NaCl only traces the spherical outflow, while SO_2 is present exclusively in the bipolar outflow. SiS and HCN were found to exist in all components of the envelope.

We constructed a model of the bipolar outflow and reproduced the observed emission of HCN(1-0), SiS(5-4) and $SO_2(10_{1,9}\text{-}10_{0,10})$. We based our geometry on the results of Muller et al. (2007) and Ziurys et al. (2007, 2009), selecting the optimal parameters from both authors. We concluded that the bipolar outflow has a large opening angle of 120°, a constant H_2 density and the expansion velocity increases linearly from 15 km s^{-1} to 45 km s^{-1}.

VY CMa is far from being completely understood. Our PdB observations provided more evidence for the bipolar outflow, the emission of the different molecular transitions showed nicely how certain molecules trace different regions of the envelope. In order to get a final understanding of the complex circumstellar environment of this hypergiant, more observations are definitely needed. Studying extra molecules, which are expected to exist closer to the central star, or farther out in the envelope, will complete the current picture of the CSE.

Also the general populations of RSGs will need further investigation. Our detection of maser sources is an important but small step. Luckily, recently several new Galactic clusters rich in RSGs have been identified. This increases the number of known RSG sources, and allows for more accurate statistical studies of the properties of these fascinating objects.

Bibliography

Alcolea, J., Bujarrabal, V., & Gomez-Gonzalez, J. 1990, A&A, 231, 431

Alcolea, J., Pardo, J. R., Bujarrabal, V., et al. 1999, A&AS, 139, 461

Alexander, M. J., Kobulnicky, H. A., Clemens, D. P., et al. 2009, AJ, 137, 4824

Beauchamp, A., Moffat, A. F. J., & Drissen, L. 1994, ApJS, 93, 187

Benjamin, R. A., Churchwell, E., Babler, B. L., et al. 2003, PASP, 115, 953

Benson, P. J., Little-Marenin, I. R., Woods, T. C., et al. 1990, ApJS, 74, 911

Bieging, J. H. & Tafalla, M. 1993, AJ, 105, 576

Bissantz, N., Englmaier, P., & Gerhard, O. 2003, MNRAS, 340, 949

Bjorkman, J. E. & Wood, K. 2001, ApJ, 554, 615

Blöcker, T., Balega, Y., Hofmann, K., & Weigelt, G. 2001, A&A, 369, 142

Blum, R. D., Ramírez, S. V., Sellgren, K., & Olsen, K. 2003, ApJ, 597, 323

Bowers, P. F., Johnston, K. J., & Spencer, J. H. 1983, ApJ, 274, 733

Buhl, D., Snyder, L. E., Lovas, F. J., & Johnson, D. R. 1974, ApJ, 192, L97

Bujarrabal, V. 1994a, A&A, 285, 953

Bujarrabal, V. 1994b, A&A, 285, 971

Bujarrabal, V., Planesas, P., & del Romero, A. 1987, A&A, 175, 164

Caron, G., Moffat, A. F. J., St-Louis, N., Wade, G. A., & Lester, J. B. 2003, AJ, 126, 1415

Cho, S.-H., Kaifu, N., & Ukita, N. 1996, A&AS, 115, 117

Choi, Y. K., Hirota, T., Honma, M., et al. 2008, PASJ, 60, 1007

Clark, B. G. 1980, A&A, 89, 377

Clark, J. S., Negueruela, I., Crowther, P. A., & Goodwin, S. P. 2005, A&A, 434, 949

Clark, J. S., Negueruela, I., Davies, B., et al. 2009, A&A, 498, 109

Comerón, F., Torra, J., Chiappini, C., et al. 2004, A&A, 425, 489

Conti, P. S. 1976, Memoires of the Societe Royale des Sciences de Liege, 9, 193

Cotera, A. S., Erickson, E. F., Colgan, S. W. J., et al. 1996, ApJ, 461, 750

Currie, T., Hernandez, J., Irwin, J., et al. 2010, ApJS, 186, 191

D'Alessio, P., Calvet, N., Hartmann, L., Franco-Hernández, R., & Servín, H. 2006, ApJ, 638, 314

Danchi, W. C., Bester, M., Degiacomi, C. G., Greenhill, L. J., & Townes, C. H. 1994, AJ, 107, 1469

Davies, B., Figer, D. F., Kudritzki, R., et al. 2009a, ApJ, 707, 844

Davies, B., Figer, D. F., Kudritzki, R.-P., et al. 2007, ApJ, 671, 781

Davies, B., Figer, D. F., Law, C. J., et al. 2008, ApJ, 676, 1016

Davies, B., Origlia, L., Kudritzki, R., et al. 2009b, ApJ, 696, 2014

Decin, L., Hony, S., de Koter, A., et al. 2006, A&A, 456, 549

Deguchi, S., Nakashima, J., Zhang, Y., et al. 2010, PASJ, 62, 391

Dutrey, A., ed. 2000, *IRAM Millimeter Interferometry Summer School 2*, IRAM, Grenoble, France

Efstathiou, A. & Rowan-Robinson, M. 1990, MNRAS, 245, 275

Elias, J. H., Frogel, J. A., & Humphreys, R. M. 1985, ApJS, 57, 91

Eliasson, B. & Bartlett, J. F. 1969, ApJ, 155, L79+

Elitzur, M. 1980, ApJ, 240, 553

Figer, D. F., Kim, S. S., Morris, M., et al. 1999, ApJ, 525, 750

Figer, D. F., MacKenty, J. W., Robberto, M., et al. 2006, ApJ, 643, 1166

Figer, D. F., Najarro, F., Gilmore, D., et al. 2002, ApJ, 581, 258

Figer, D. F., Rich, R. M., Kim, S. S., Morris, M., & Serabyn, E. 2004, ApJ, 601, 319

Fleck, Jr., J. A. & Canfield, E. H. 1984, Journal of Computational Physics, 54, 508

Garmany, C. D. & Stencel, R. E. 1992, A&AS, 94, 211

Goldsmith, P. F. & Langer, W. D. 1999, ApJ, 517, 209

Gustafsson, B., Edvardsson, B., Eriksson, K., et al. 2008, A&A, 486, 951

Habing, H. J. 1996, A&A Rev., 7, 97

Habing, H. J., Sevenster, M. N., Messineo, M., van de Ven, G., & Kuijken, K. 2006, A&A, 458, 151

Haikala, L. K., Nyman, L.-A., & Forsstroem, V. 1994, A&AS, 103, 107

Hall, P. J., Allen, D. A., Troup, E. R., Wark, R. M., & Wright, A. E. 1990, MNRAS, 243, 480

Harwit, M. & Bergin, E. A. 2002, ApJ, 565, L105

Harwit, M., Malfait, K., Decin, L., et al. 2001, ApJ, 557, 844

Herbig, G. H. 1970a, Memoires of the Societe Royale des Sciences de Liege, 59, 13

Herbig, G. H. 1970b, ApJ, 162, 557

Herbig, G. H. 1972, ApJ, 172, 375

Herpin, F., Baudry, A., Alcolea, J., & Cernicharo, J. 1998, A&A, 334, 1037

Heske, A. 1989, A&A, 208, 77

Högbom, J. A. 1974, A&AS, 15, 417

Hogerheijde, M. R. & van der Tak, F. F. S. 2000, A&A, 362, 697

Humphreys, E. M. L., Gray, M. D., Yates, J. A., et al. 2002, A&A, 386, 256

Hyland, A. R., Becklin, E. E., Neugebauer, G., & Wallerstein, G. 1969, ApJ, 158, 619

Iben, J. I. 1985, QJRAS, 26, 1

Indebetouw, R., Mathis, J. S., Babler, B. L., et al. 2005, ApJ, 619, 931

Ivezić, Ž. & Elitzur, M. 1997, MNRAS, 287, 799

Ivezić, Ž., Nenkova, M., & Elitzur, M. 1999, ArXiv Astrophysics e-prints

Jewell, P. R., Snyder, L. E., Walmsley, C. M., Wilson, T. L., & Gensheimer, P. D. 1991, A&A, 242, 211

Jiang, B. W., Deguchi, S., & Ramesh, B. 1999, PASJ, 51, 95

Jiang, B. W., Deguchi, S., Yamamura, I., et al. 1996, ApJS, 106, 463

Johnson, H. L. 1968, ApJ, 154, L125+

Justtanont, K., de Jong, T., Helmich, F. P., et al. 1996, A&A, 315, L217

Kaifu, N., Buhl, D., & Snyder, L. E. 1975, ApJ, 195, 359

Kemper, F., Stark, R., Justtanont, K., et al. 2003, A&A, 407, 609

Kim, J., Cho, S.-H., Oh, C. S., & Byun, D.-Y. 2010, ApJS, 188, 209

Knapp, G. R., Sandell, G., & Robson, E. I. 1993, ApJS, 88, 173

Knowles, S. H., Mayer, C. H., Cheung, A. C., Rank, D. M., & Townes, C. H. 1969, Science, 163, 1055

Krügel, E. 2003, *The physics of interstellar dust*, ed. Krügel, E., IoP Series in Astronomy and Astrophysics

Krügel, E. 2008, *An introduction to the physics of interstellar dust*, ed. Krügel, E., Series in astronomy and astrophysics

Kwan, J. & Scoville, N. 1974, ApJ, 194, L97

Lada, C. J. & Reid, M. J. 1978, ApJ, 219, 95

Le Bertre, T. & Nyman, L. 1990, A&A, 233, 477

Le Sidaner, P. & Le Bertre, T. 1996, A&A, 314, 896

Levesque, E. M. 2010, in Astronomical Society of the Pacific Conference Series, Vol. 425, Hot and Cool: Bridging Gaps in Massive Star Evolution, ed. C. Leitherer, P. Bennett, P. Morris, & J. van Loon, 103–+

Levesque, E. M., Massey, P., Olsen, K. A. G., et al. 2006, ApJ, 645, 1102

Lewis, B. M. 1989, ApJ, 338, 234

Lewis, B. M., David, P., & Le Squeren, A. M. 1995, A&AS, 111, 237

Lipscy, S. J., Jura, M., & Reid, M. J. 2005, ApJ, 626, 439

Lockett, P. & Elitzur, M. 1992, ApJ, 399, 704

Low, F. J., Johnson, H. L., Kleinmann, D. E., Latham, A. S., & Geisel, S. L. 1970, ApJ, 160, 531

Lucas, R., Bujarrabal, V., Guilloteau, S., et al. 1992, A&A, 262, 491

Lucy, L. B. 1999, A&A, 344, 282

Malizia, A., Bassani, L., Stephen, J. B., et al. 2005, ApJ, 630, L157

Massey, P., DeGioia-Eastwood, K., & Waterhouse, E. 2001, AJ, 121, 1050

Mercer, E. P., Clemens, D. P., Meade, M. R., et al. 2005, ApJ, 635, 560

Mermilliod, J. C., Mayor, M., & Udry, S. 2008, A&A, 485, 303

Merrill, K. M. & Stein, W. A. 1976, PASP, 88, 294

Messineo, M., Davies, B., Figer, D. F., et al. 2011, ApJ, submitted

Messineo, M., Davies, B., Ivanov, V. D., et al. 2009, ApJ, 697, 701

Messineo, M., Figer, D. F., Davies, B., et al. 2010, ApJ, 708, 1241

Messineo, M., Figer, D. F., Davies, B., et al. 2008, ApJ, 683, L155

Messineo, M., Habing, H. J., Menten, K. M., Omont, A., & Sjouwerman, L. O. 2004, A&A, 418, 103

Messineo, M., Habing, H. J., Menten, K. M., et al. 2005, A&A, 435, 575

Messineo, M., Habing, H. J., Sjouwerman, L. O., Omont, A., & Menten, K. M. 2002, A&A, 393, 115

Messineo, M. & Menten, K. 2011, A&A, in preparation

Meynet, G. & Maeder, A. 2000, A&A, 361, 101

Meynet, G. & Maeder, A. 2003, A&A, 404, 975

Min, M., Dullemond, C. P., Dominik, C., de Koter, A., & Hovenier, J. W. 2009, A&A, 497, 155

Moffat, A. F. J., Fitzgerald, M. P., & Jackson, P. D. 1977, ApJ, 215, 106

Monnier, J. D., Bester, M., Danchi, W. C., et al. 1997, ApJ, 481, 420

Monnier, J. D., Danchi, W. C., Hale, D. S., et al. 2000, ApJ, 543, 861

Monnier, J. D., Tuthill, P. G., Lopez, B., et al. 1999, ApJ, 512, 351

Morris, M. & Bowers, P. F. 1980, AJ, 85, 724

Morris, M., Guilloteau, S., Lucas, R., & Omont, A. 1987, ApJ, 321, 888

Morris, M., Redman, R., Reid, M. J., & Dickinson, D. F. 1979, ApJ, 229, 257

Mulders, G. D., Dominik, C., & Min, M. 2010, A&A, 512, A11+

Müller, H. S. P., Schlöder, F., Stutzki, J., & Winnewisser, G. 2005, Journal of Molecular Structure, 742, 215

Müller, H. S. P., Thorwirth, S., Roth, D. A., & Winnewisser, G. 2001, A&A, 370, L49

Muller, S., Dinh-V-Trung, Lim, J., et al. 2007, ApJ, 656, 1109

Nakashima, J. & Deguchi, S. 2007, ApJ, 669, 446

Nakashima, J.-i. & Deguchi, S. 2006, ApJ, 647, L139

Negueruela, I., González-Fernández, C., Marco, A., Clark, J. S., & Martínez-Núñez, S. 2010, A&A, 513, A74+

Nercessian, E., Omont, A., Benayoun, J. J., & Guilloteau, S. 1989, A&A, 210, 225

Neufeld, D. A., Feuchtgruber, H., Harwit, M., & Melnick, G. J. 1999, ApJ, 517, L147

Nyman, L., Hall, P. J., & Le Bertre, T. 1993, A&A, 280, 551

Olofsson, H., Rydbeck, O. E. H., Lane, A. P., & Predmore, C. R. 1981, ApJ, 247, L81

Omont, A., Lucas, R., Morris, M., & Guilloteau, S. 1993, A&A, 267, 490

Pardo, J. R., Cernicharo, J., Gonzalez-Alfonso, E., & Bujarrabal, V. 1998, A&A, 329, 219

Peraiah, A. 2001, *An Introduction to Radiative Transfer: Methods and Applications in Astrophysics*, ed. Peraiah, A., Cambridge University Press

Perrine, C. D. 1923, PASP, 35, 229

Perryman, M. A. C., Lindegren, L., Kovalevsky, J., et al. 1997, A&A, 323, L49

Pierce, M. J., Jurcevic, J. S., & Crabtree, D. 2000, MNRAS, 313, 271

Poelman, D. R. & Spaans, M. 2005, A&A, 440, 559

Poelman, D. R. & Spaans, M. 2006, A&A, 453, 615

Price, S. D., Egan, M. P., Carey, S. J., Mizuno, D. R., & Kuchar, T. A. 2001, AJ, 121, 2819

Richards, A. M. S., Yates, J. A., & Cohen, R. J. 1998, MNRAS, 299, 319

Robitaille, T. P., Whitney, B. A., Indebetouw, R., & Wood, K. 2007, ApJS, 169, 328

Rosseland, S. 1924, MNRAS, 84, 525

Rutten, R. J. 2003, *Radiative Transfer In Stellar Atmospheres*, Sterrekundig Instituut Utrecht, Institute of Theoretical Astrophysics Oslo, available at `http://www.astro.uu.nl/~rutten/Radiative_Transfer.html`

Rybicki, G. B. & Lightman, A. P. 1979, *Radiative processes in astrophysics*, ed. Rybicki, G. B. & Lightman, A. P., Wiley-Interscience

Schöier, F. L., van der Tak, F. F. S., van Dishoeck, E. F., & Black, J. H. 2005, A&A, 432, 369

Scholz, M. & Wood, P. R. 2000, A&A, 362, 1065

Schwab, F. R. 1984, AJ, 89, 1076

Sevenster, M. N. 1999, MNRAS, 310, 629

Shinnaga, H., Moran, J. M., Young, K. H., & Ho, P. T. P. 2004, ApJ, 616, L47

Sivagnanam, P., Le Squeren, A. M., Minh, F. T., & Braz, M. A. 1990, A&A, 233, 112

Smith, N., Humphreys, R. M., Davidson, K., et al. 2001, AJ, 121, 1111

Snyder, L. E. & Buhl, D. 1975, ApJ, 197, 329

Sobolev, V. V. 1960, *Moving envelopes of stars*, ed. Sobolev, V. V. (Cambridge: Harvard University Press)

Spencer, J. H., Schwartz, P. R., Waak, J. A., & Bologna, J. M. 1977, AJ, 82, 706

Spencer, J. H., Schwartz, P. R., Winnberg, A., et al. 1981, AJ, 86, 392

Stephenson, C. B. 1990, AJ, 99, 1867

Subramaniam, A., Mathew, B., Bhatt, B. C., & Ramya, S. 2006, MNRAS, 370, 743

Takaba, H., Iwate, T., Miyaji, T., & Deguchi, S. 2001, PASJ, 53, 517

Taylor, G. B., Carilli, C. L., & Perley, R. A., eds. 1999, Astronomical Society of the Pacific Conference Series, Vol. 180, *Synthesis Imaging in Radio Astronomy II*

Tenenbaum, E. D., Woolf, N. J., & Ziurys, L. M. 2007, ApJ, 666, L29

Valdettaro, R., Palla, F., Brand, J., et al. 2001, A&A, 368, 845

van Blerkom, D. 1978, ApJ, 223, 835

van Blerkom, D. & Auer, L. 1976, ApJ, 204, 775

Verhoelst, T., van der Zypen, N., Hony, S., et al. 2009, A&A, 498, 127

Vinković, D. 2003, PhD thesis, University of Kentucky

Vinković, D., Blöcker, T., Hofmann, K., Elitzur, M., & Weigelt, G. 2004, MNRAS, 352, 852

Westerlund, B. 1961, PASP, 73, 51

Whitelock, P., Menzies, J., Feast, M., et al. 1994, MNRAS, 267, 711

Wilson, T. L., Rohlfs, K., & Hüttemeister, S. 2009, *Tools of Radio Astronomy* (Springer-Verlag)

Wittkowski, M., Langer, N., & Weigelt, G. 1998, A&A, 340, L39

Woosley, S. E., Heger, A., & Weaver, T. A. 2002, Reviews of Modern Physics, 74, 1015

Yang, M. & Jiang, B. W. 2011, ApJ, 727, 53

Ziurys, L. M., Milam, S. N., Apponi, A. J., & Woolf, N. J. 2007, Nature, 447, 1094

Ziurys, L. M., Tenenbaum, E. D., Pulliam, R. L., Woolf, N. J., & Milam, S. N. 2009, ApJ, 695, 1604